Author:
White, Emily

Title:
Atmospheric inverse modelling of biospheric carbon dioxide fluxes in the UK and Europe

Atmospheric inverse modelling of biospheric carbon dioxide fluxes in the UK and Europe

Emily Daisy Evora White

A dissertation submitted to the University of Bristol in accordance with the requirements for the degree of Doctor of Philosophy in the Faculty of Science

School of Chemistry

November 2018

41,000 words

Abstract

Human activity is causing rising atmospheric CO_2 concentrations leading to an increase in global mean temperature and a changing climate. Monitoring biospheric CO_2 fluxes at global, continental and regional scales is important to track how the biosphere is responding to climate change and to evaulate the success of mitigation policies that involve enhancing sinks of CO_2, such as reforestation. The use of atmospheric measurements of CO_2 concentrations in a "top-down" inverse modelling set-up is a valuable tool to assess CO_2 fluxes. This thesis works towards the first top-down estimates of UK biospheric CO_2 fluxes and includes the contribution to a regional inverse modelling comparison project that focusses on European biospheric CO_2 fluxes.

A hierarchical Bayesian inverse modelling framework is first adapted to some of the unique characteristics of CO_2 fluxes, such as the strong diurnal and seasonal cycle, and the mixture of anthropogenic, biospheric and oceanic sources. This framework is then applied to the UK, using atmospheric CO_2 concentrations from a relatively dense network of tall-tower and surface sites in and around the UK. The UK biosphere is found to be in balance with a net zero CO_2 flux to the atmosphere, according to two separate inversions that use two different models of biospheric flux as prior information. Extending the scope of the study to Europe, with a different measurement network and a more mature model of biospheric fluxes, reveals that European biospheric fluxes are also in balance and estimates found here agree with previous regional inverse modelling studies. Of particular interest in this thesis is the role of the prior biospheric flux model. The inversion process has highlighted some areas where models need to improve, for example in estimating fluxes related to human disturbance.

To my dearest parents and treasured friends.

For the love of this beautiful world we live in.

Ever hopeful.

Acknowledgements

Most importantly, I would like to thank my supervisor, Matt Rigby, for his invaluable help and patience as he has guided me through my PhD project over the past four years. I am very grateful for Matt's continual support of my work, as well as his encouragement to take advantage of opportunities outside my research, such as a three-month placement at the Government Office for Science.

Mark Lunt and Alistair Manning have also been instrumental in the development of my PhD project. I am indebted to Mark for the time he has taken to help me navigate the code for the, catchily named, hierarchical Bayesian trans-dimensional MCMC inversion. Alistair has provided much helpful support and discussion surrounding the NAME model and my inversion results.

I had the privilege of guiding several students through Masters or summer projects. Evie Walton deserves an extra special mention and many thanks for helping me churn through reams of NAME model runs.

I am also very grateful for the painstaking work of the "measurement people": Simon O'Doherty, Dickon Young, Ann Stavert and Kieran Stanley, who have provided the data to make the inverse modelling in this thesis possible.

The Atmospheric Chemistry Research Group has felt a bit like my second home at times and I have enjoyed seeing it grow and evolve during my time here. It is a really wonderful group of supportive people and it's been a pleasure to be a part of it. I would like to thank each and every one of them for the different things that they contribute to the group and for the wealth of interesting nuggets that they have taught me over the years. I am particularly appreciative of their continuous encouragement in the final stages to help get me over the finish line!

I have been lucky enough to participate in a number of collaborations throughout my PhD project, which has been a wonderful way to engage with the community and has really helped to shape my thinking about my results and the wider field. Eddy Comyn-Platt and Luke Smallman deserve a special mention for their help with JULES and CARDAMOM.

Writing a thesis is a daunting task but reading a thesis can be even more so! I would like to thank Matt, Luke Western, Rachel Tunnicliffe and Josh Pencheon for taking the time to read parts of my thesis and their very helpful comments.

My PhD project has been part of the GW4+ Doctoral Training Partnership and I am indebted to the DTP for introducing me to the most wonderful group of friends. Rose, Mike, Erik, Beth, Moya,

Serginio and James have been such an incredible support network for the past four years as we have undertaken this PhD journey together, and importantly had lots of fun! We will definitely remain friends for life.

I have loved living in Bristol, it is a beautiful city, and living with some great housemates has made it all the more special. I would like to thank them for all the meals we have shared, the chats we have had, and for making Bristol home.

My amazing friends away from Bristol have played a very important role in this thesis too. I thank them all very much for helping me to have fun and encouraging me every step of the way.

As this acknowledgement list comes to an end there remain some very special people to mention. My Grandparents, Marcia, Dennis and Joan, have always impressed upon me the value of education and I am extremely grateful for all they have done for me throughout my life. And, of course, my parents, Rosie and Rob, who are always there for me no matter what. They have been such amazing rocks throughout this whole process and deserve all the thanks in the World for their tireless support. I really don't know what I would do without them.

Finally, I would just like to thank the gardeners in Royal Fort Gardens for making it such a delightful place to take breaks from the PhD. This garden has helped me to clear my head on numerous occasions and has also been a beautiful spot for al fresco summer lunches with friends. It is one of my favourite places in Bristol.

Declaration

I declare that the work in this dissertation was carried out in accordance with the requirements of the University's Regulations and Code of Practice for Research Degree Programmes and that it has not been submitted for any other academic award. Except where indicated by specific reference in the text, the work is the candidate's own work. Work done in collaboration with, or with the assistance of, others, is indicated as such. Any views expressed in the dissertation are those of the author.

SIGNED: ..... DATE:.....

Table of contents

List of figures

List of tables

Chapter 1

Introduction

1.1 The carbon cycle and climate change

The global concentration of carbon dioxide (CO_2) in the atmosphere is rising. Charles David Keeling began making continuous measurements of CO_2 in "clean" background air at the remote site of Mauna Loa in Hawaii in the 1950s and as a result of this work, the "Keeling Curve" (Fig. 1.1a) provided one of the first pieces of evidence of the rapid increase in atmospheric CO_2 concentrations.

The atmosphere is just one of the global carbon reservoirs (Fig. 1.2). The biosphere stores carbon in vegetation and soils and the ocean stores carbon at different depths and within sediments. Geological reservoirs exist where terrestrial vegetation, mostly from the Carboniferous period, has been fossilised or where, millions of years ago, phytoplankton and zooplankton have undergone anaerobic decomposition. These carbon reservoirs have different turnover times (the mass of carbon divided by the flux of exchange). The atmosphere has a turnover time of a few years, whereas this is decades to millennia in the biospheric and oceanic reservoirs and over 10,000 years in the geological reservoir (Ciais et al., 2013). As well as these turnover times, processes relating to the exchange of carbon between reservoirs occur on a whole range of timescales. The biosphere removes CO_2 from the atmosphere via photosynthesis (gross primary productivity, GPP) and releases CO_2 via autotrophic (plant) and heterotrophic (soil, microbial and animal) respiration. These are particularly strong diurnal and seasonal processes. Photosynthesis is driven by changes in solar radiation down to seconds and there is predominant uptake of CO_2 during the growing season as vegetation flourishes and a predominant source of CO_2 outside the growing season due to heterotrophic respiration as vegetation dies and decomposes. The oscillation seen in the red curve of Fig. 1.1a represents this strong seasonal cycle of atmospheric CO_2 that originates from the disproportionate northern hemisphere biospheric flux to the atmosphere (since the land mass is greater than in the southern hemisphere). Atmospheric CO_2 is exchanged with the ocean due to the partial CO_2 pressure difference and the timescale of this process is dependant on wind speeds and wave breaking. A smaller oceanic carbon pool exists in marine biota, such as phytoplanckton and, like with the terrestrial biosphere, CO_2 exchange here through photosynthesis and respiration is also driven by solar radiation down to timescales of seconds.

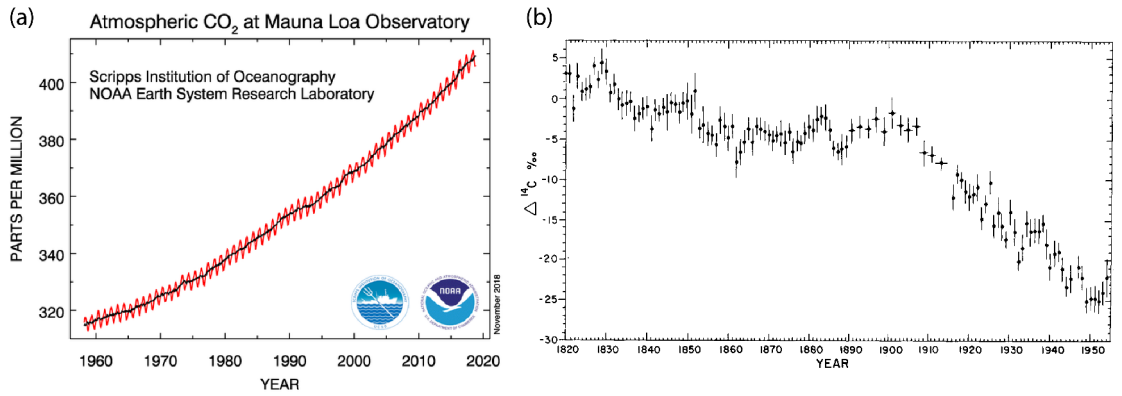

Fig. 1.1: (a): CO_2 measurements taken at Mauna Loa between 1958 and 2018. The red curve represents monthly average concentrations and the black curve represents seasonally corrected data (Keeling et al., 1976; Thoning et al., 1989). (b): measurements of atmospheric $\Delta^{14}C$ derived from tree rings between 1820 and 1954 (Stuiver and Quay, 1981). The uncertainty bars give the 1σ uncertainty range.

Prior to Keeling's measurements, Hans Suess noticed a decrease in the $^{14}C/C$ ratio in tree rings (Fig. 1.1b). Unlike active carbon pools in the biosphere and ocean, fossil fuels from the geological reservoirs contain no ^{14}C, since ^{14}C has a half-life of 5700 years. Burning fossil fuels will therefore reduce the $^{14}C/C$ ratio. This provided important evidence that the rise in atmospheric CO_2 concentrations is predominantly due to fossil fuel burning as a result of industrialisation. Averaged over the past half-century, the contribution from fossil fuels is estimated to be 82% of total CO_2 emissions due to human activity (Boden et al., 2018), whilst the other 18% is caused by land use changes, such as deforestation (Hansis et al., 2015; Houghton and Nassikas, 2017).

Around the time of the industrial revolution (circa 1750), the concentration of CO_2 in the atmosphere was 277 parts per million (ppm) (Joos and Spahni, 2008) and today, in 2018, it has increased by nearly 45% to around 405 ppm (Dlugokencky and Tans, 2018). This rapid rise in atmospheric CO_2 concentrations is important because CO_2 is a greenhouse gas (GHG). The greenhouse effect is a natural process that keeps the planet 33°C warmer than it would otherwise be, through the absorption of infrared radiation by GHGs in the atmosphere (Kiehl and Trenberth, 1997). Natural levels of GHGs have fluctuated in the past over time-scales of thousands of years. In the last million years, the concentration of CO_2 has varied between roughly 180 ppm and 280 ppm (Petit et al., 1999). This is directly linked to global temperatures; times of low CO_2 concentration have been cooler glacial periods, whereas times of high CO_2 concentration have been warmer inter-glacial periods. However, the rapid increase in CO_2 concentrations in the last century and a half since the industrial revolution is unprecedented and is leading to rising global temperatures (Zeebe et al., 2016).

Already, the global mean temperature has risen by 1°C since the pre-industrial era, which has led to a number of observed climatic changes (Masson-Delmotte et al., 2018). Warmer temperatures cause the ocean to expand and ice caps to melt, leading to sea level rise. Further impacts of climate change include increased precipitation in some areas and higher frequency of extreme

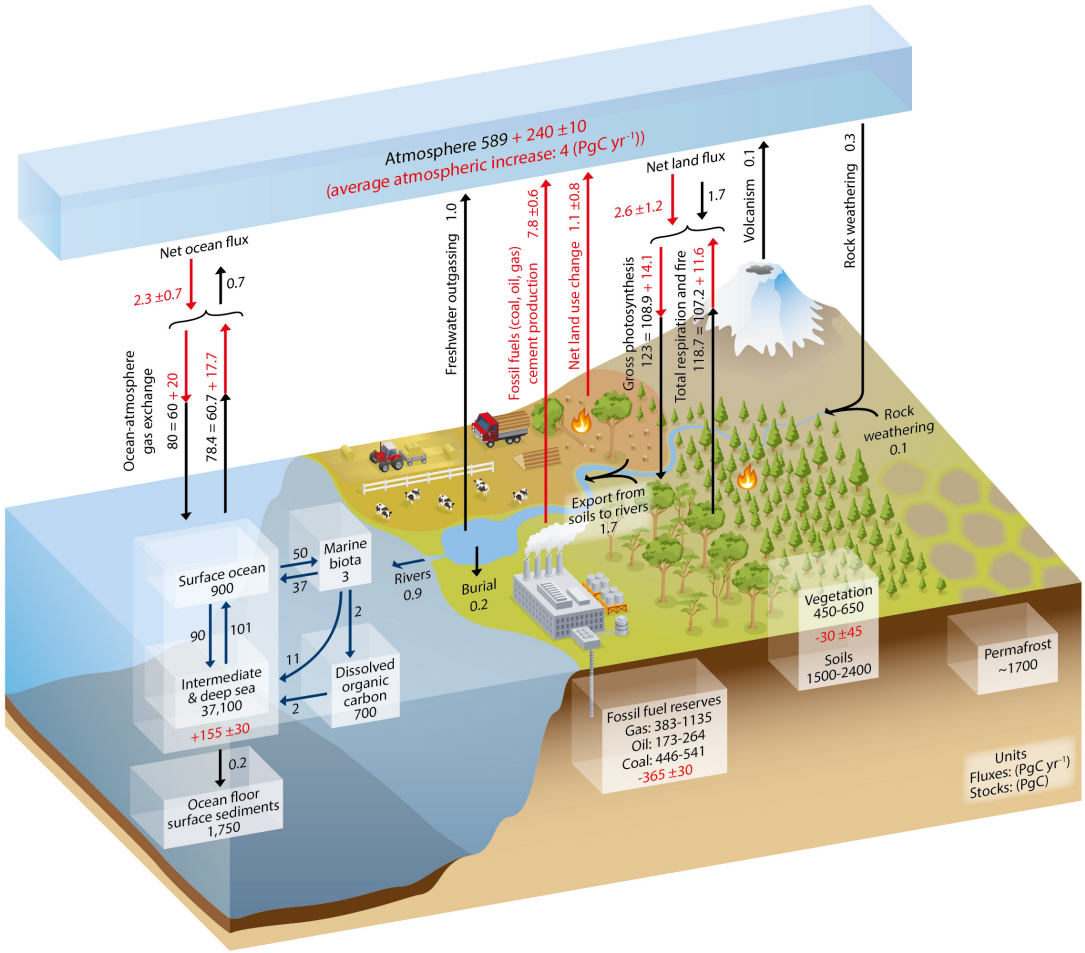

Fig. 1.2: The global carbon cycle, taken from Ciais et al. (2013). Numbers in boxes represent the mass of the reservoir in Pg C (10^{12} grams carbon). Numbers next to arrows represent fluxes between reservoirs in Pg C yr^{-1} averaged over 2000-2009. Black numbers and arrows show pre-industrial (before 1750) reservoir masses and fluxes. Red numbers and arrows show the changes in reservoir masses and fluxes related to anthropogenic activity.

events, such as droughts, heatwaves, floods, cyclones and wildfires. Many species have already been affected and are expected to be further affected by a changing climate; for example, researchers have observed changes to migratory patterns and geographic range. Future climate change will disproportionately affect the poorest in society and negatively impact the ability to achieve international sustainable development, for example through the United Nations Sustainable Development Goals (https://www.un.org/sustainabledevelopment/).

Looking at the changes in the fluxes between the carbon reservoirs over the past 50 years, only around 45% of the CO_2 emissions from fossil fuel burning and land use change end up as CO_2 in the atmosphere (Dlugokencky and Tans, 2018). The ocean absorbs around 23% of the CO_2 emitted as it is soluble in water REF (Le Quéré et al., 2018). This alters ocean chemistry and leads to ocean acidification, which impacts marine organisms REF. The remaining roughly 32% is absorbed by the land, mostly because the additional CO_2 in the atmosphere causes a fertilisation effect for plants, making them more productive (Sitch et al., 2008), but also because of the affects of climate change, which will be further discussed shortly (Le Quéré et al., 2018). For an idea of the magnitudes and uncertainties on the fluxes from these reservoirs see the values in Fig. 1.2, which are averaged over the period 2000-2009. Annual emissions from fossil fuel burning and uptake into these three reservoirs have all grown since 1959, however emissions from land-use change have remained roughly constant. This partitioning between the reservoirs tended to be calculated through measuring and estimating the atmospheric, oceanic and total carbon reservoirs, leaving the residual to be attributed to the biospheric reservoir. More recently, methods to understand the biospheric reservoir have improved, despite remaining uncertain, leading to a budget imbalance between estimated emissions and estimated uptake into the biospheric, oceanic and atmospheric reservoirs of just 0.07 Pg C yr^{-1} averaged over the past 50 years. This indicates that over half-century timescales the estimates for the individual reservoirs in the carbon budget are well understood. However, on shorter timescales there can be significant variability, for example the imbalance grows to -0.6 Pg C yr^{-1} averaged over 2007-2016 (Le Quéré et al., 2018). This is most likely due to errors in the estimates for the land and ocean sinks.

The climate and the carbon cycle are inextricably linked, so changes to the climate will impact the way that different carbon reservoirs can absorb CO_2 (Friedlingstein et al., 2006). For example, a warmer climate stimulates photosynthesis in plants and may lengthen the growing season in some areas. However, at higher temperatures plants become heat stressed and suffer from drought, and as a result photosynthesis may be reduced. Warmer temperatures also increase soil respiration, in turn increasing the nutrient release to soils, which has a positive feedback on photosynthesis. Along with a rise in atmospheric CO_2 concentrations, an increase in the amplitude of the seasonal cycle of atmospheric CO_2 concentrations has been observed (Graven et al., 2013), indicating that the northern hemisphere biosphere is exchanging 30-60% more CO_2 between the growing and non-growing season than it did 50 years ago. This is thought to be explained by ecological changes such as the migration of evergreen shrubs and trees northwards as the temperature increases and human disturbance, such as

fire and logging, shifting the overall composition of vegetation to contain an increasing amount of younger trees that experience shorter, more intense periods of CO_2 uptake.

The biosphere and biospheric fluxes are the focus of much of this thesis and their future evolution as the climate changes can be separated into two key components.The first is how the biosphere reacts to changing temperatures, precipitation patterns and extreme events. The second is how human interaction with the biosphere changes as global population increases and humans inevitably look to the biosphere as a way to curb CO_2 emissions to the atmosphere.

1.2 The international response to climate change

1.2.1 Intergovernmental Panel on Climate Change

In 1988, the World Meterological Organisation (WMO) and the United Nations Environment Programme (UNEP) established the Intergovernmental Panel on Climate Change (IPCC), as concerns began to grow about the potential climate impacts of rising CO_2 concentrations. Widely regarded as the accepted voice on climate change, the IPCC brings together leading climate scientists from all over the world and amalgamates the latest climate science publications to produce reports on the current state of climate science. These reports set out the impacts of climate change and present options for mitigation and adaptation. Through a painstaking process, the wording in the "Summary for Policymakers" is agreed by representatives from all participating governments, ensuring that the message of the IPCC report is clear and understandable for decision-makers.

1.2.2 United Nations Framework Convention on Climate Change

The United Nations Framework Convention on Climate Change (UNFCCC) was initiated and entered into force in 1994. Annual Conferences of the Parties (COPs) take place for the, currently 192, countries involved to discuss the progress being made in relation to action against climate change. At COP 3 in Kyoto in 1997, the Kyoto Protocol was agreed, setting legally binding obligations for Annex I countries (those countries considered at the time to be more economically developed) to reduce their GHG emissions between 2008 and 2012. The Doha amendment extended this period from 2013 to 2020. A key component of the Kyoto Protocol is to establish GHG inventories and Annex I countries are required to submit estimates of their GHG emissions to the UNFCCC each year to track progress. In 2010, at the UN Climate Change Conference it was also agreed that warming should be limited to 2°C.

At COP 21 in 2015, the successor to the Kyoto Protocol was agreed in the form of the Paris Agreement. The Paris Agreement states that average global mean temperature rise should be kept to *well below* 2°C and that there should be a concerted effort to limit warming to 1.5°C. Instead of making the distinction between Annex I and non-Annex I countries, the Paris Agreement includes all countries and works on the basis of Nationally Determined Contributions (NDCs). Countries are

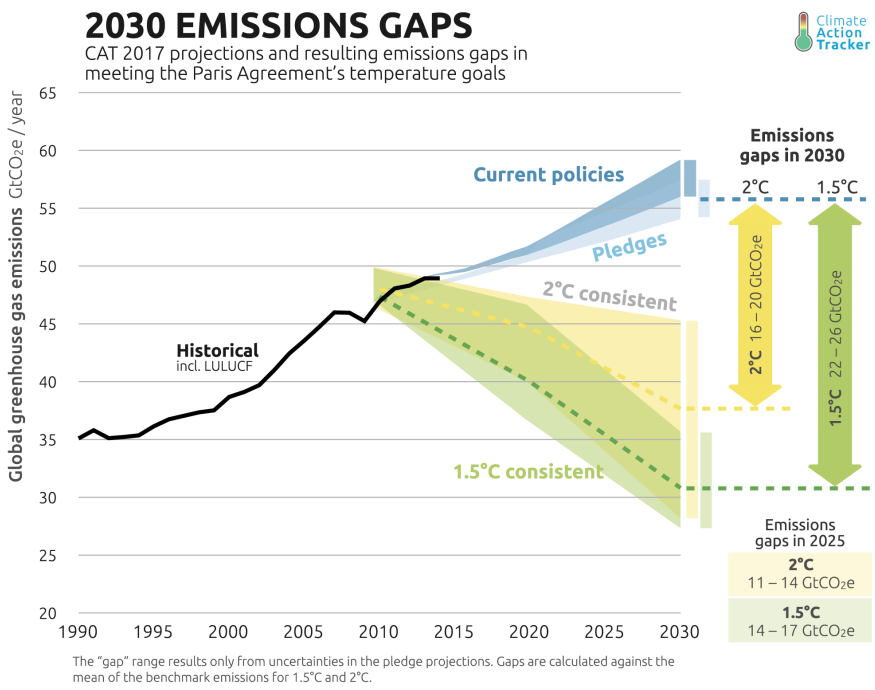

Fig. 1.3: Historical global emissions (black line) along with projected future emissions under current climate change policies (darker blue range) and the pledges, or NDCs, made as a result of the Paris Agreement (lighter blue range). The emissions pathways that are consistent with meeting the 2°C limit in global mean temperature rise (yellow range) and those consistent with meeting the 1.5°C limit in global mean temperature rise (green range). The yellow and green arrows show the emissions reductions required, through more ambitious pledges and their realisation as climate change policies, to meet the 2°C and 1.5°C targets respectively. Graph taken from the Climate Action Tracker (https://climateactiontracker.org/global/cat-emissions-gaps/).

expected to make pledges of their emissions reductions and the financial support that they can provide to less economically developed countries. The current emissions reduction pledges from all countries are shown in Fig. 1.3 and fall short of what is required to remain within the 2°C target, let alone the 1.5°C target. As part of this process, a global stocktake will occur every 5 years to evaluate the progess countries are making towards the aims of the Paris Agreement and countries will be required to strengthen the ambition of their NDCs in response.

The agreement also aims for GHG neutrality by 2050, meaning that sources of GHGs as a result of human activity are balanced by negative emissions or sinks (i.e. a removal of CO_2 from the atmosphere through processes such as reforestation or carbon capture and storage). Indeed, enhancing the carbon sink is deemed a neccessity given the scale of the problem (Rockström et al., 2017). Therefore, many NDCs involve policies that create negative emissions. Forests in particular provide huge mitigation potential (Griscom et al., 2017) and 25% of the emissions reductions pledged through NDCs are expected to be achieved through changing land use and reforestation (Grassi et al., 2017).

The latest IPCC report was especially commissioned to examine the climatic impacts of a 1.5°C world versus a 2°C world and revealed alarming consequences of both scenarios (Masson-Delmotte et al., 2018). For example, under 1.5°C warming coral reefs are expected to decline by 80%, rising to 99% under 2°C warming. The Arctic ocean will be free of sea-ice around once a century under 1.5°C warming and once a decade under 2°C warming. The authors of the report estimate that there are just 12 years until the 1.5°C warming is met if there are no changes to current policies.

1.2.3 UK Climate Change Act 2008

The United Kingdom (UK) has developed its own piece of legislation: the UK Climate Change Act 2008 (The UK government, 2008), that commits to reducing greenhouse gas emissions to 80% of 1990 levels by 2050. This requires an annual report of UK emissions to be submitted to Parliament. As part of this legislation, carbon budgets are set at 5 year intervals. The Committee on Climate Change was set up to scrutinise government over its progress towards each carbon budget and to suggest ways in which the UK may be able to meet its targets.

1.3 Reporting greenhouse gas emissions

All of these agreements and pieces of legislation require countries to know how much CO_2 and other GHGs they are emitting. Measuring progress in reducing GHGs requires an estimate of the baseline to work from and some form of regular reporting to ensure countries are on track. The most common form of reporting takes an inventory-style approach, where an estimate is made for the emissions of different sectors. This is known as the "bottom-up" approach.

1.3.1 CO_2 emissions from fossil fuels and industry

National inventories of CO_2 emissions from fossil fuel burning are built up using a variety of different datasets, such as population density and the quantity of fuel sold to power vehicles etc. Various scaling factors are used to convert the information in these datasets into GHG emissions estimates. Different countries have access to different levels of data, meaning that some inventories are much more sophisticated than others. Sophisticated inventories may use country-specific scaling factors as opposed to the basic scaling factors that are applied globally. This can lead to some discrepancies in different inventories (Peylin et al., 2011). One inventory covering global sectoral emissions is the Emissions Database for Global Atmospheric Research (EDGAR, EC-JRC/PBL, 2011), which uses emissions factors for different human activities and technologies and collates information at the most basic level required for submission to the UNFCCC for every country. Another is the Open-source Data Inventory for Anthropogenic CO_2 (ODIAC, Oda and Maksyutov, 2011), based on datasets such as satellite-observed night lights.

The UK inventory is the National Atmospheric Emissions Inventory (NAEI, http://naei.beis.gov.uk). This inventory is compiled by the consultancy Ricardo Engineering and Environment for the UK government and is made up of energy and fuel statistics from the Department for Business Energy and Industrial Strategy, transport statistics from the Department for Transport and food and farming statistics from the Department for the Environment, Food and Rural Affairs, along with information from trade associations and individual companies. Emissions factors are from the 2006 IPCC Guidelines for National Greenhouse Gas Inventories or more specialised literature sources. The inventory complies with, and aims to exceed, the Tier 1 Quality Assurance and Quality Control standards outlined in the 2006 IPCC guidelines, which are the basic requirements for submitting inventory data to the UNFCCC. Uncertainty estimates (two standard deviations) for individual CO_2 sectors range from 2-55% and the combined uncertainty across all greenhouse gases is estimated to be 5% in 1990 and 3% in 2006 (Brown et al., 2018).

1.3.2 CO_2 emissions from land use and land use change

The anthropogenic emissions sector that is subject to the largest uncertainty is that of CO_2 emissions from land-use, land-use change and forestry (LULUCF). Bookkeeping models are used to track the carbon stored in vegetation and soils before and after land-use change, which incorporate datasets on, for example, biomass in forests, harvests and land that has been converted to a new land-use type. Finding estimates for different human or natural effects applying to the same areas of land is a difficult task and one problem with estimating emissions from LULUCF is ensuring comparability between estimates (Grassi et al., 2018). In the inventories reported to the UNFCCC, LULUCF is considered to be the direct human induced effect on both managed and un-managed land (such as land-use change and harvest); the indirect human induced effects on managed land (those due to climate change, such as changes in temperature and precipitation); and the natural effects on managed land (such as inter-annual variability and forest fires). The uncertainty on global LULUCF emissions

submitted to the UNFCCC, averaged over 1990-2010, is around 90% to two standard deviations (Grassi et al., 2017). In contrast, the LULUCF estimates given in the IPCC reports only include the direct human induced effect on managed and un-managed land; the indirect human induced and natural effects, on the other hand, are considered to be the "residual sink". These decadal estimates have an uncertainty of around 110% to two standard deviations (Houghton and Nassikas, 2017). These reporting differences have led to a discrepancy between global estimates of LULUCF of around 4 Pg CO_2 yr^{-1} between 2005-2014, which is a significant as this is equivalent to 10% of the total anthropogenic emissions during this time period (Grassi et al., 2018).

1.3.3 CO_2 flux from the terrestrial biosphere

Regional terrestrial carbon fluxes can be estimated using a range of observational and computational methods. These include the up-scaling of direct flux measurements made using eddy covariance or chamber systems (Baldocchi and Wilson, 2001) and models of atmosphere-biosphere CO_2 exchange. Flux measurements are important for understanding the small-scale processes responsible for carbon fluxes. However, they are relatively localised estimates (centimetres to kilometres), which are challenging to scale up to national levels. Biosphere models and land surface models (LSMs) can be used to estimate carbon fluxes using coupled representations of biogeophysical and biogeochemical processes, driven by observations of meteorology and ecosystem parameters (Bloom et al., 2016; Clark et al., 2011; Potter, 1999). Such models describe processes to varying degrees of complexity and are driven by observational data to varying degrees of detail; hence predictions of biospheric GHG fluxes can vary significantly between models (Atkin et al., 2015; Todd-Brown et al., 2013).

1.3.4 Emissions estimation from the top-down

Emissions accounting using the bottom-up technique is in widespread use. However, many pieces of legislation, and indeed the IPCC itself, suggest that "best practice" should include alternative methods of emissions accounting to verify bottom-up estimates. One alternative, known as the "top-down" approach, is to consider atmospheric concentrations of the gases emitted. An atmospheric concentration measurement can be related to the surface emissions that have contributed to it via the wind fields that transported the emissions to the measurement location. This is the premise of atmospheric inverse modelling, which will be further described in Section 1.4.

There are not many countries that officially use this technique to report emissions. The UK, Switzerland and Australia are currently the only ones. This is partly due to the number of continuous measurements required, which are costly to set up and maintain. However, top down methods are constantly improving, so their use in official emissions verification is likely to grow in the near future. It is even thought that as bottom-up methods reach the limit of possible uncertainty reduction, top-down methods may be able to overtake these methods for precision (Leip et al., 2018).

1.4 Atmospheric inverse modelling

Atmospheric inverse modelling has been introduced as a top-down approach that provides an alternative to the bottom-up approaches described in Section 1.3. In this approach, a model of atmospheric transport is used to relate spatiotemporally resolved surface fluxes to atmospheric measurements of CO_2 concentrations. Since atmospheric observations are sensitive to fluxes spanning tens to hundreds of kilometres (Gerbig et al., 2009), inverse methods are a valuable tool for examining national fluxes and evaluating estimates of surface exchange of CO_2 at larger spatial scales. Through the introduction of the atmospheric data, an initial "guess" of the surface fluxes may be changed to be consistent with atmospheric concentrations.

1.4.1 The forward model

Equation 1.1 describes the linear forward model that maps the relationship between atmospheric observations and fluxes and forms the basis of the inverse method.

$$\boldsymbol{y} = \boldsymbol{H}\boldsymbol{x} + \varepsilon \tag{1.1}$$

Here, there are observations of atmospheric CO_2 concentrations, $\boldsymbol{y}$, that are connected to a set of CO_2 fluxes, $\boldsymbol{x}$, via a model of atmospheric transport, $\boldsymbol{H}$. Using what is known initially about the fluxes in a region (the first "guess"), a time series of modelled "observations", $\boldsymbol{H}\boldsymbol{x}$, can be calculated. However, due to imperfections in the atmospheric transport model, initial flux estimates and measurements, there will likely be a mismatch between the modelled "observations" and what has actually been measured in the atmosphere. This mismatch is accounted for in the additional parameter, ε.

The component parts of the inverse modelling technique - the atmospheric data, the atmospheric transport model and the initial flux maps used to help solve the problem - are described in the following sections.

1.4.2 Atmospheric data

Measurements may be collected on a variety of platforms, such as through an inlet on a tall (typically 100s of metres above the surface) or surface (~10m above the surface) tower, via aircraft, by filling flasks of air or, more recently, via satellite. The work of this thesis will focus on measurements taken at tall tower and surface tower continuous measurement sites.

1.4.2.1 Measuring atmospheric CO_2 concentrations

Measurements of atmospheric CO_2 are usually made with a cavity ring-down spectrometer (CRDS). This instrument involves a cavity with a mirror at either end, a laser and a detector. The laser is fired within the cavity and the intensity of light is allowed to build up. The laser is then turned off and the

light intensity within the cavity decays away as light leaks out. The mirrors allow the light to bounce back and forth, giving a large effective path length for the decay. If a gas, such as CO_2, is injected into the cavity, the absorption or reflection properties of the gas will decrease the time taken for the light intensity to decay to $1/e$ from the original intensity. This "ringdown" time can be calculated from the detector signal, which is registered in volts, and can then be converted to a mole fraction of gas in the cavity. Of course, measurements need to be calibrated and a description of the calibration method for a specific set-up is described in Sect. 1.4.2.2.

1.4.2.2 UK measurement networks

To support the UK's climate change legislation, a continuous and automated measurement network has been established (Stanley et al., 2018; Stavert et al., 2018) with the goal of providing estimates of GHG emissions that are independent of the UK's bottom-up anthropogenic inventory. CO_2 mole fractions are continuously measured at six sites across the UK and Republic of Ireland. Four of these sites, Mace Head (MHD), Ridge Hill (RGL), Angus (TTA) and Tacolneston (TAC), originally formed the UK Deriving Emissions related to Climate Change (UK-DECC) network and are described in Stanley et al. (2018), whilst two, Heathfield (HFD) and Bilsdale (BSD), were developed under the Greenhouse gAs Uk and Global Emissions (GAUGE) programme (Palmer et al., 2018) and are described in Stavert et al. (2018). The location of these sites is shown in Fig. 1.4. The site at MHD, Republic of Ireland, is a coastal station, 10m above ground level (magl), situated primarily to measure concentrations of background air arriving at the site from the Atlantic Ocean. The Laboratoire des Sciences du Climat et de l'Environnement (LSCE) is responsible for making CO_2 measurements at this site from a 23 magl inlet (see Vardag et al., 2014, for a full site description). All of the UK sites are tall-tower stations (with inlets ranging from 42 to 248 magl), designed to measure elevated greenhouse gas mole fractions as air is transported over the surface in the UK and Europe.

Previous studies have used data from the UK-DECC network to infer UK emissions of GHGs of predominantly anthropogenic origin, such as methane (CH_4), nitrous oxide (N_2O) and HFC-134a (Ganesan et al., 2015; Manning et al., 2011; Say et al., 2016). These studies found varying levels of agreement with bottom-up inventory methods. Whilst CO_2 is measured by the network, top-down CO_2 emissions estimates are not yet reported to the UK government as the methodology for disaggregating biospheric and anthropogenic sources and sinks needs to be developed.

Continuous CO_2 measurements are made at all stations using Picarro G2301 or G2401 CRDS instruments. CRDS data are corrected for daily linear instrumental drift using standard gases and for instrumental non-linearity using calibration gases, spanning a range of above and below ambient mole fractions, on a monthly basis (Stanley et al., 2018). Calibration and standard gases are of natural composition and calibrated at the GasLab Max Planck Institute for Biogeochemistry, Jena, or the World Calibration Centre for CO_2 at Empa, linking them to the WMO X2007 scale (Stanley et al., 2018; Stavert et al., 2018). At sites with multiple inlets, since there is only one CRDS instrument, each hour is divided up into the number of inlets and measurements at each inlet are taken continuously

over this period. Therefore, measurements at each height at Bilsdale and Tacolneston (with 3 inlets) are taken continuously for roughly 20 minutes every hour, and at Heathfield and Ridge Hill (with 2 inlets) measurements are taken continuously for roughly 30 minutes at each inlet every hour. Dividing measurements between multiple inlets each hour is not thought to have a large effect on the data collected, however for the purposes of the inverse modelling in this study a 2-hourly average of the data is taken, which ensures any discontinuities are smoothed out. Further information about the instruments, measurement protocol and uncertainty estimates can be found in Stanley et al. (2018) and Stavert et al. (2018).

Depending on the atmospheric conditions, these tall-tower sites may be measuring CO_2 concentrations within the well vertically mixed boundary layer (typically during the daytime when deep convection occurs in part due to warmer surface temperatures) or within the stratified free troposphere (possible during some nighttime hours when the height of the boundary layer decreases to below the inlet height in part due to cooler surface temperatures). Measurements made in the well mixed boundary layer are representative of changes to CO_2 concentrations due to surface CO_2 fluxes whereas measurements made in the free troposphere capture background CO_2 concentrations. Understanding surface fluxes of CO_2 is the aim of inverse modelling so the distinction between these times of day needs to be taken into account and this often leads to some level of data filtering. An investigation of various filtering techniques is carried out in this thesis.

1.4.3 Atmospheric transport models

Atmospheric transport models connect surface fluxes to the concentrations of gases in the atmosphere. There are two types of transport models. The first are Lagrangian models that release particles from a reference point and then track the location of those particles as they are dispersed in the atmosphere following fields of wind speed and wind direction. A random term is also added to simulate sub grid scale turbulence, slightly nudging the particles in different directions whilst they follow the mean wind fields. The second are Eulerian models that operate on a fixed grid and gases are advected based on the conditions in each grid cell.

Lagrangian models are well suited to understanding regional atmospheric transport at high spatial resolutions (on the order of $0.1^\circ \times 0.1^\circ$ but it would be very computationally expensive to run these models over a global domain. Eulerian models on the other hand are very well suited to global modelling but are lacking in spatial resolution (typically on the order of $1^\circ \times 1^\circ$). Lagrangian models are also known to perform well at times of convective transport but poorly during times of low wind speeds and stratified atmospheric conditions, which leads inverse modelling teams to filter out data points for which the model may not be able to correctly represent the atmospheric transport.

Both a Lagrangian and an Eulerian model are used in this work. The Lagrangian model is used to find regional source sensitivities, i.e. where surface emissions are expected to contribute to measurements taken within the region, and the Eulerian model provides the mole fraction boundary conditions at the edge of the region.

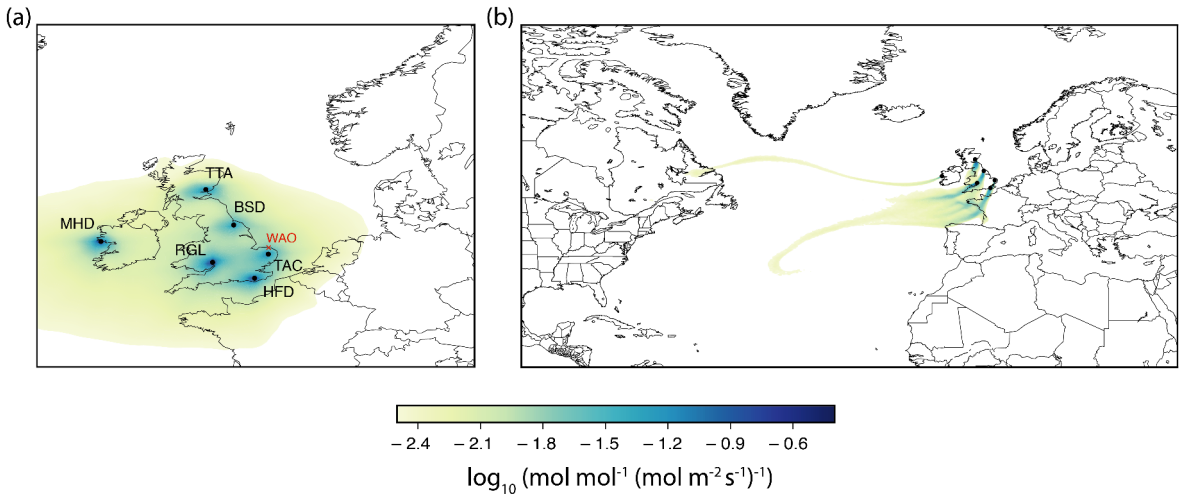

Fig. 1.4: (a): Mean annual NAME footprint (or surface sensitivities) for 2014, for each of the six sites. MHD: Mace Head; RGL: Ridge Hill; HFD: Heathfield; TAC: Tacolneston; BSD: Bilsdale; TTA: Angus. WAO shows the location of the Weybourne Atmospheric Observatory, where data has been used to validate the results in Chapter 3 but has not been included in the inversion (the mean footprint from this station is not plotted). (b): Footprints representing the 30-day air histories corresponding to one 2-hour measurement period (i.e. where air has been for the 30 days before the measurement was taken) for each of the same six sites. The map extent represents a typical NAME domain.

1.4.3.1 NAME

The Chernobyl disaster in 1986 revealed the lack of available models to estimate where emissions from a point source, in this case radioactive particles from the nuclear reactor, are transported in the atmosphere. As a result, in 1987, the UK Met Office developed The Numerical Atmospheric dispersion Modelling Environment (NAME), a Lagrangian particle dispersion model (LPDM). Later, it was adapted to run backwards in time to find where air has come from, and where it could have picked up possible emissions sources, before arriving at a particular location, i.e. a measurement site.

When run backwards in time, as it is for inverse modelling applications, NAME tracks thousands of particles back in time from observation locations. The particles move based on mean wind speed, wind direction and sub grid scale turbulence. The model determines the locations where air masses interacted with the surface, and therefore where surface sources and sinks could contribute to a concentration measurement. The "surface" is defined in this work as the lowest 40 km of the troposphere. There is therefore no vertical dimension to the model output, however there are multiple vertical levels in the model itself (determined by the meteorology used to drive the model) and it is possible for a particle to interact with the surface, move to a higher height and then move back to the surface, in which case all interaction with the surface would be recorded. At the end of the simulation, which could be 30 days as in Fig. 1.4b, the air histories at each time step in the model are integrated to give a full 30-day back trajectory. The model provides a grid of the sensitivity of each mole fraction observation to the potential flux from each grid cell and this is often referred to as the “footprint” of

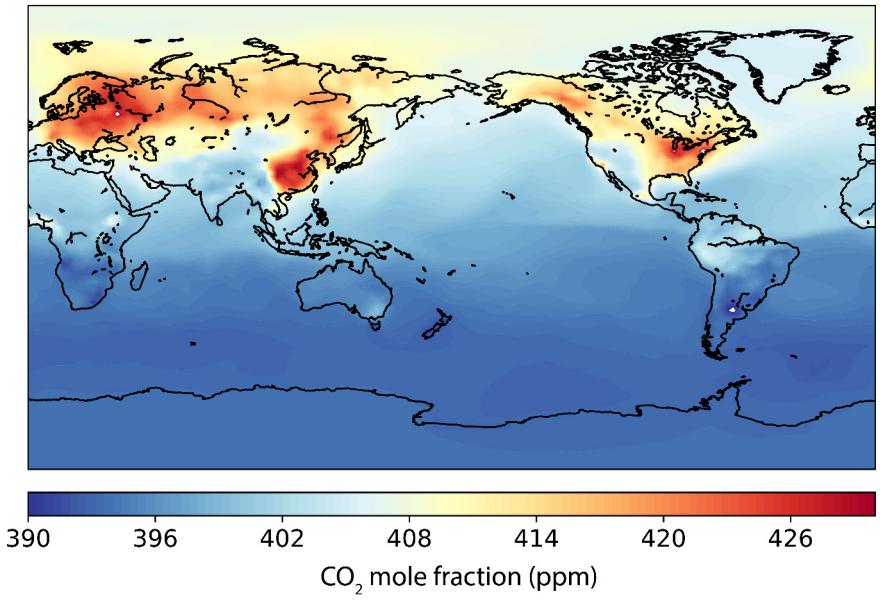

Fig. 1.5: MOZART model CO_2 output for February 2014 at the vertical level closest to the surface.

a particular observation (Jones et al., 2006; Manning et al., 2011). The units used to describe the footprints are therefore units of concentration divided by units of flux $\left(\frac{mol/mol}{mol/m^2/s}\right)$. The meteorological dataset used to drive NAME is from the Met Office Unified Model (Cullen, 1993). This is constructed of a series of meteorological analyses that produce short-term forecasts using observational data from the land surface, ocean and satellites to constrain the meteorology in the model to the real state of the atmosphere. The spatial and vertical resolution of the meteorology guides the spatial and vertical resolution of NAME and changes through time; for example between early-2010 and mid-2014 it is 0.233° latitude by 0.352° longitude (roughly 25 by 25 km over the UK) and has 70 vertical levels.

Figure 1.4a shows an average footprint over 2014 and Fig. 1.4b shows a footprint taken from a 2-hour period. The average footprint shows that with the six measurement sites described in Sect. 1.4.2.2, a good coverage of sensitivity to UK surface fluxes can be achieved. For context, a sensitivity of -1.5 $\log_{10}$ (mol mol^{-1} (mol m^{-2} s^{-1})$^{-1}$) and a grid cell flux of 3.5×10^{-7} mol m^{-2} s^{-1} (an average NEE flux in June) equates to a concentration of 0.1ppm seen at the measurement site, which is above typical measurement uncertainty. The 2-hour footprint shows a typical full NAME domain and how measurements taken at MHD are mostly receiving air from across the Atlantic, with even some small sensitivity to the east coast of the United States of America. The other sites are mostly sensitive to fluxes over the UK and northern France.

1.4.3.2 MOZART

The Model for OZone And Related chemical Tracers (MOZART, Emmons et al., 2010) is a global Eulerian model. The model is driven by a meteorological dataset, which could be output from climate

models or assimilations of meterological data, and an emissions inventory. In each grid cell, emissions are dispersed based on physical dispersion processes that are simulated using equations of shallow, mid-level and deep convective transport, as well as vertical diffusion in the boundary layer and advective transport. The model includes grid cell chemistry. As sources and sinks of CO_2 occur at the land surface and are taken into account in the emissions inventory, the atmospheric chemistry component in a CO_2 simulation does not play a large role. MOZART's spatial resolution is guided by the meterology used to drive it, which in this work is GEOS-5 (Rienecker et al., 2011) at a resolution of 2.5° latitude by 1.895° longitude, and there are 56 vertical levels.

MOZART monthly mean mole fractions for February 2014 are shown in Fig. 1.5. The inter-hemispheric gradient of CO_2 is clear to see, as a result of the slow mixing times between the hemispheres and the comparatively large number of emissions sources and sinks in the northern hemisphere. Also, since this is winter in the northern hemisphere, the terrestrial biosphere will be a dominant source of CO_2, whereas the terrestrial biosphere in the southern hemisphere will be a dominant sink of CO_2.

1.4.4 Initial fluxes

The "initial fluxes" used in the forward model in Sect. 1.4.1 are known as "prior" fluxes in the inverse model and are used to initiate and guide the inversion process. These fluxes usually come from bottom up inventories of sources and sinks as described in Sect. 1.3 and this is the approach taken in this thesis. One alternative approach, however, constructs the prior as a spatio-temporal correlation, where the mean flux distribution is a function of an underlying dataset related to emissions, such as population density. This is known as the geostatistical method (Michalak, 2004).

1.4.5 The Jacobian matrix

As has already been seen, the role of the atmospheric transport model is to relate concentration measurements to surface fluxes. The output of the model provides a map of where on the surface any fluxes would contribute to an observation made at a measurement site, so where the measurements are sensitive to fluxes. This sensitivity of concentration measurements to fluxes is known as the "Jacobian" or "sensitivity" matrix, denoted $\boldsymbol{H}$ in the description of the linear forward model (Eq. 1.1), and maps the change in $\boldsymbol{y}$ given a change in $\boldsymbol{x}$ (Eq. 1.2).

$$\boldsymbol{H}_{ij} = \frac{\Delta \boldsymbol{y}_i}{\Delta \boldsymbol{x}_j} \tag{1.2}$$

However, $\boldsymbol{H}$ is not neccessarily simply the output from the atmospheric transport model. Finding a new flux field by changing the flux in every grid cell in the domain is likely to be a very large problem and the data from atmospheric observations is unlikely to be enough to constrain it. To reduce the problem the model grid may be split up into a smaller number of regions, known as basis functions. The sum of fluxes in these basis functions are then scaled up or down in the inversion. Therefore, $\boldsymbol{H}$

has dimensions m (number of data points) by n (number of basis functions). Further basis functions are included to account for the boundary conditions.

1.4.6 The inverse model

1.4.6.1 Bayes theorem

The idea behind the "inverse" problem is that an updated estimate of the initial fluxes, $\boldsymbol{x}$, can be found by incorporating the information about atmospheric concentrations, $\boldsymbol{y}$, thereby reducing the mismatch, ε from Eq. 1.1. Both $\boldsymbol{x}$ and $\boldsymbol{y}$ are probability distributions as they have an uncertainty related to them. The question is, how does the probability distribution of $\boldsymbol{x}$ change when new evidence, $\boldsymbol{y}$, is introduced?

Determining conditional probabilities like this is the premise of Bayes theorem, which forms the basis of the majority of inverse methods. Consider two separate events, A and B. $P(A)$ and $P(B)$ are the probabilities of A and B occurring independently of each other, while $P(A,B)$ and $P(B,A)$ are the probabilities of both events occurring together and $P(A|B)$ and $P(B|A)$ are the conditional probabilities of $P(A)$ occurring given that $P(B)$ has already occurred and vice versa. Given the product rule:

$$P(A,B) = P(B|A)P(A) \tag{1.3}$$

$$P(B,A) = P(A|B)P(B) \tag{1.4}$$

And since the order doesn't matter:

$$P(A,B) = P(B,A) \tag{1.5}$$

Leading to Bayes theorem, which describes the probability of an event occurring based on knowledge about a different, related event:

$$P(A|B) = \frac{P(B|A)P(A)}{P(B)} \tag{1.6}$$

Therefore, in the case of atmospheric inverse modelling the Bayes equation can be written as:

$$\rho(\boldsymbol{x}|\boldsymbol{y}) = \frac{\rho(\boldsymbol{y}|\boldsymbol{x})\rho(\boldsymbol{x})}{\rho(\boldsymbol{y})} \tag{1.7}$$

The parameters to be estimated (such as the flux and boundary condition scaling) are initially described by a prior probability density function (PDF), $\rho(\boldsymbol{x})$, that is not aware of any observations, $\boldsymbol{y}$. $\rho(\boldsymbol{y}|\boldsymbol{x})$ is known as the likelihood function and describes how well $\boldsymbol{y}$ maps to the prior estimate of $\boldsymbol{x}$, i.e. the mismatch, ε, from Eq. 1.1. The updated parameter estimates are described by the posterior PDF $\rho(\boldsymbol{x}|\boldsymbol{y})$, i.e. the probability of the parameter estimates *given* the added information $\boldsymbol{y}$. The term

$\rho(\boldsymbol{y})$, known as the "evidence", acts as a normalising term and is the same for all values of $\boldsymbol{y}$. It can usually be ignored because in the case where $\boldsymbol{x}$ has a fixed number of dimensions it will cancel out when comparing different parameter values. However, for reasons that will become apparent in Sect. 1.4.8.1, the dimension of $\boldsymbol{x}$ does not always remain constant throughout the inversion used in this thesis, and in this case the evidence term becomes important.

$\rho(\boldsymbol{x})$ and $\rho(\boldsymbol{y}|\boldsymbol{x})$ could be considered to have a Gaussian distribution and the form of this distribution is described by Eq. 1.8. Here $\boldsymbol{\mu}$ is the mean of the distribution and $\boldsymbol{\Sigma}$ is a covariance matrix whose diagonal elements describe the variance of the parameters, $\boldsymbol{x}$, and whose off-diagonal elements describe the covariance between different parameters.

$$f(\boldsymbol{x}) = \frac{1}{\sqrt{|\boldsymbol{\Sigma}|2\pi}} exp\left(-\frac{1}{2}(\boldsymbol{x}-\boldsymbol{\mu})^T\boldsymbol{\Sigma}^{-1}(\boldsymbol{x}-\boldsymbol{\mu})\right) \tag{1.8}$$

Combining Eq. 1.7 and 1.8 gives Eq. 1.9, where $\boldsymbol{R}$ is the data covariance matrix and $\boldsymbol{P}$ is the prior covariance matrix. $\boldsymbol{x}_{prior}$ is the prior mean estimate for $\boldsymbol{x}$.

$$\rho(\boldsymbol{x}|\boldsymbol{y}) \propto \frac{1}{2\pi\sqrt{|\boldsymbol{R}||\boldsymbol{P}|}} exp\left(-\frac{1}{2}(\boldsymbol{y}-\boldsymbol{H}\boldsymbol{x})^T\boldsymbol{R}^{-1}(\boldsymbol{y}-\boldsymbol{H}\boldsymbol{x})\right) \cdot exp\left(-\frac{1}{2}(\boldsymbol{x}_{prior}-\boldsymbol{x})^T\boldsymbol{P}^{-1}(\boldsymbol{x}_{prior}-\boldsymbol{x})\right) \tag{1.9}$$

1.4.6.2 Finding the posterior solution

The optimum solution to Eq. 1.9 is where the probability of the posterior $\rho(\boldsymbol{x}|\boldsymbol{y})$ is at its maximum. There are a number of different ways to reach the posterior solution. Optimisation approaches seek to maximise the exponential components of Eq. 1.9, which leads to the cost function in Eq. 1.10 where the solution is found by minimising J (Tarantola, 2005).

$$J(\boldsymbol{x}) = (\boldsymbol{y}-\boldsymbol{H}\boldsymbol{x})^T\boldsymbol{R}^{-1}(\boldsymbol{y}-\boldsymbol{H}\boldsymbol{x}) + (\boldsymbol{x}-\boldsymbol{x}_{prior})^T\boldsymbol{P}^{-1}(\boldsymbol{x}-\boldsymbol{x}_{prior}) \tag{1.10}$$

The cost function can be minimised using many different techniques. For less complex problems a Bayesian synthesis inversion may be used, where the model grid is split into a number of regions (basis functions) to reduce the size of the problem and the cost function is solved analytically (e.g. Enting et al., 1995; Gerbig et al., 2003b; Rödenbeck et al., 2003). Alternatively, the solution may be found iteratively using simple gradient descent methods (e.g. Rodenbeck et al., 2009). For more complex problems, ensemble and variational methods have been developed to approximate the solution. Ensemble methods, like the ensemble Kalman filter used in the CarbonTracker framework (Peters et al., 2005), carry out an ensemble of model runs and use that to approximate the exact solution. Variational methods, such as the 4D-variational approach used in TM5-4DVar (Basu et al., 2013), take a step by step approach to find the optimal solution.

More recently, Markov chain Monte Carlo (MCMC) algorithms have been used as an alternative method to sample the parameter space and build up the posterior PDF (Rigby et al., 2011). More details of this technique are given in Sect. 1.4.8.2.

1.4.7 Challenges of atmospheric inverse modelling

Robust uncertainty quantification in Bayesian frameworks can be difficult as they require that uncertainties in the prior flux estimate $\rho(\boldsymbol{x})$, and uncertainties in the model's ability to simulate the data $\rho(\boldsymbol{y}|\boldsymbol{x})$, are well characterised. In practice, this is rarely the case and various studies have investigated the use of data-driven uncertainty estimation (e.g. Berchet et al., 2013; Ganesan et al., 2014; Kountouris et al., 2018b; Michalak, 2004).

Inversions are also known to suffer from "aggregation errors". One type of aggregation error arises from the way in which areas of the flux domain are grouped together to decrease the number of unknowns, because usually there are not sufficient data to solve for fluxes in each model grid cell (Kaminski et al., 2001). If too coarse a resolution is used the aggregation error may be large, however if too fine a resolution is used, the computational cost can become prohibitive in some inversion frameworks.

Finally, for reasons of mathematical and computational convenience within probabilistic inverse modelling approaches, Gaussian PDFs are often used to describe prior knowledge (Miller et al., 2014). However, in reality atmospheric GHG emissions or uptake processes are physically bound to either be positive or negative but cannot be both. Gaussian assumptions, which permit both positive and negative solutions, can therefore lead to unphysical solutions. Miller et al. (2014)has investigated different ways to impose non-negativity on inversion estimates and finds that MCMC approaches, like the one described in the following sections, are best able to robustly impose this constraint and find the most realistic posterior estimates and uncertainty bounds.

1.4.8 Hierarchical Bayesian trans-dimensional Markov Chain Monte Carlo

The hierarchical Bayesian trans-dimensional MCMC approach has been developed to address many of the challenges introduced in Sect. 1.4.7.

1.4.8.1 Hierarchical Bayes and the trans-dimensional case

The traditional Bayesian approach requires that decisions about the form of the prior PDF, $\rho(\boldsymbol{x})$, and likelihood function, $\rho(\boldsymbol{y}|\boldsymbol{x})$, are made a priori. These pre-defined decisions have the potential to strongly influence the form of the posterior PDF in an inversion (Ganesan et al., 2014). In a hierarchical Bayesian inversion, a second "level" to the traditional Bayes equation is introduced, to account for the fact that initial parameter uncertainty estimates are themselves uncertain. This is known as a "hierarchical" Bayes framework and is shown in Eq. 1.11 (Ganesan et al., 2014). In this case, additional parameters, known as hyper-parameters, are used to describe the uncertainties

in the prior and the model and posterior estimates for these parameters are found as a result of the inversion. In Eq 1.11, θ is an assortment of hyper-parameters describing the uncertainty on $\boldsymbol{x}$, and the model-measurement error.

$$\rho(\boldsymbol{x},\theta,k|\boldsymbol{y}) = \rho(\boldsymbol{y}|\boldsymbol{x},\theta,k)\rho(\boldsymbol{x}|\theta,k)\rho(k)\rho(\theta) \tag{1.11}$$

Alongside the additional hyper-parameters θ, Eq. 1.11 also contains a parameter k, the number of unknowns in $\boldsymbol{x}$. In response to the problem of aggregation errors, Lunt et al. (2016) has set out a trans-dimensional method that finds the balance between the two extremes of this problem without imposing arbitrary region boundaries. In this approach, the number of basis functions to be solved is not fixed a priori because spatial regions can be moved, created or destroyed throughout the inversion process, and hence $\boldsymbol{x}$ has an unknown length. Therefore, the number of unknowns is itself a parameter to be solved in the inversion, with the uncertainty in this term propagating through to the posterior parameters estimate, more fully accounting for the uncertainties within a traditional Bayesian approach.

1.4.8.2 Reversible jump Markov chain Monte Carlo

In general, there is no analytical solution to the hierarchical Bayesian equation, so the posterior solution is approximated using a reversible jump Metropolis-Hastings MCMC algorithm (Green, 1995; Lunt et al., 2016; Metropolis et al., 1953; Tarantola, 2005).

This is an algorithm that explores the possible values for each parameter by making a new proposal for a parameter value at each step of a "chain" of possible values. Equation 1.12 describes how values are accepted or rejected.

$$U \leq (prior\ ratio \times likelihood\ ratio \times proposal\ ratio) \tag{1.12}$$

U is a uniformly distributed random number between 0 and 1, the prior ratio is the probability of the proposed value sampled from the prior PDF compared to the probability of the existing value; the likelihood ratio is the likelihood of the proposed value compared to the likelihood of the existing value; and the proposal ratio is the probability of generating the current model state (i.e. the model with the current number of basis functions) from the proposed model state compared to the probability of generating the proposed model state from the current model state. New values are accepted if the combination of ratios is greater than or equal to the value U. This means that more favourable parameter values or model states are always accepted; however, less favourable parameter values or model states can also be randomly accepted in order to fully explore the full posterior PDF. The algorithm will usually have to undergo around 10^5 or 10^6 iterations to appropriately explore the posterior distribution. At the end of the algorithm a chain of all accepted parameter values is stored (if a proposal is rejected the chain will spend longer at the previously accepted value). A histogram of

this chain describes a posterior PDF for each parameter so that statistics such as the mean, median and standard deviation can be calculated.

Reversible jump MCMC is required here because it is able to sample PDFs with an unknown number of dimensions, unlike the standard MCMC algorithm where the dimensions of the problem must be pre-defined. Therefore, the proposal ratio must be calculated at each iteration, whereas in standard MCMC the proposal ratio would always be equal to 1.

1.5 Brief history of atmospheric CO_2 inversions

Atmospheric inversions differ in four main respects: the observational data used, the atmospheric transport model used, the prior fluxes used and, as has been touched on already, the inverse framework used. These differences govern the scale across which the inversion takes place and have led to a diversity of inverse flux estimates. However, it is important to understand the differences between fluxes from many methods to better understand the methods themselves.

In CO_2 emissions estimation, researchers have mostly focussed on finding estimates for biospheric CO_2 fluxes. This is because it is difficult to separate the anthropogenic and biospheric components from the observational data and, since the uncertainty of bottom-up biospheric fluxes is comparatively large compared to that of bottom-up anthropogenic fluxes, anthropogenic fluxes can be thought of as "known".

1.5.1 Global inversions

The first global atmospheric inversions of CO_2 were developed in the 1980s, using Eulerian transport models and weekly surface flask data (Enting and Mansbridge, 1989; Tans et al., 1989). Given the differing results that were being produced, the Atmospheric Tracer Transport Model Intercomparison Project (Transcom) was set up, initally to investigate the impact of using different transport models in the same Bayesian synthesis inversion with 11 land and 11 ocean regions and using data from 76 measurement sites in the GLOBALVIEW-2000 dataset (Gurney et al., 2003). Atmospheric transport models were found to be a large contributor to uncertainty, comparable to the uncertainty related to the limited number of CO_2 observations. The work concluded that the reduction of uncertainty of carbon budgets in the mid-latitudes could be achieved through improved transport simulation, whereas in the tropics the lack of data was the limiting factor.

As more complex inversion systems became available, such as the ones introduced in Sect. 1.4.6.2, the comparison could extend its remit and investigate the differences between the inverse set-ups, as well as differences in observational datasets and choice of prior fluxes (Peylin et al., 2013). These differences led to a spread in annual mean fluxes across the eleven inversions of around 1 Pg C yr^{-1} (for context, mean global flux across the inversion period was -3.11 Pg C yr^{-1}). Despite these limitations, Peylin et al. (2013) note that the results of the study provide a unique perspective on the

global carbon budget, as atmospheric inverse modelling is the only tool that can evaluate exchange between all carbon pools.

In the Global Carbon Budget 2014 (Le Quéré et al., 2015), global atmospheric inversions were incorporated for the first time to estimate year to year changes in biospheric fluxes, which correlated well with the budget residual that had previously been used to estimate the uptake of anthropogenic CO_2 by the biosphere. Inversions could also contribute to the evaluation of the spatial distribution of land and ocean fluxes.

1.5.2 Regional inversions

Whilst understanding global CO_2 emissions is important for constraining the global carbon budget, for the emissions reporting requirements of the Paris Agreement and other national pieces of climate change legislation, such as the UK Climate Change Act, 2008, CO_2 fluxes need to be evaluated at smaller regional scales, over continents and individual countries.

Continental studies have been carried out over Europe, for example by Peters et al. (2010) using an Eulerian transport model, by Rivier et al. (2010) comparing Eulerian and Lagrangian transport models, or by Kountouris et al. (2018a) using a Lagrangian transport model. Gerbig et al. (2003b) and (Schuh et al., 2010) have assesed North American fluxes using Lagrangian transport models. At the country scale, the high resolution offered by Lagrangian transport models is required. Studies have been carried out over the Netherlands (Meesters et al., 2012) and New Zealand (Steinkamp et al., 2017), for example. Regional inversions have focussed on New England and Quebec in Canada (Matross et al., 2006) and on the state of Oregon in the USA (Göckede et al., 2010).

To date, regional inverse modelling set-ups have not benefitted from the same intercomparison studies carried out for global inversions. However, a study focussed on comparing regional inverse set-ups over Europe is currently being developed and Chapter 4 presents one contribution to the project.

1.6 Thesis motivation

CO_2 emissions as a result of human activity are rising, both through burning fossil fuels and through LULUCF, which is leading to rising global mean temperature. The latest IPCC report, commissioned to look at the climate impacts of living in a world 1.5°C warmer than pre-industrial times, has given a stark warning to the global community. There are just 12 years to implement policies that will limit global mean temperature rise to 1.5°C. Monitoring atmospheric CO_2 concentrations and using inverse modelling to find surface fluxes provides one means by which current emissions can be evaluated and progress to meet targets can be tracked.

The strengths of atmospheric CO_2 inversions currently lie in estimating biospheric CO_2 fluxes. Although anthropogenic emissions estimation is the aim of carbon targets, biospheric emissions

estimation can make an important contribution towards this. Firstly, a significant part of anthropogenic emissions are related to biospheric fluxes as 18% are a result of LULUCF. Atmospheric CO_2 inversions usually assume the anthropogenic component is well known and include it as a fixed term in the inversion, however in these cases researchers typically only refer to the anthropogenic emissions from fossil fuel burning as the emissions related to LULUCF are difficult to quantify and subject to large uncertainties. As such, there is scope for atmospheric CO_2 inversions to be sensitive to fluxes from LULUCF and as the biosphere is potentially the target of 25% of emissions reductions under the Paris Agreement, alternative mechanisms to evaluate these fluxes will become more important. Secondly, the biosphere is changing as a result of climate change. The potential of the biosphere to absorb CO_2 from the atmosphere is clearly why it is being used to mitigate climate change. Therefore, it is important to track how that potential changes as climate variables, such as temperature and precipitation, change. Thirdly, through advancing inverse modelling techniques and improving biospheric flux estimates, it is hoped that inverse modelling can be used to estimate anthropogenic fluxes from fossil fuel burning and LULUCF more routinely in the future.

Under the UK Climate Change Act, 2008, the UK has its own obligations to monitor GHG emissions and report them to Parliament each year. The UK is advanced compared to other nations in its use of top-down emissions verification, establishing the UK-DECC measurement network to verify emissions of GHGs such as CH_4, N_2O and HFC-134a (Ganesan et al., 2015; Manning et al., 2011; Say et al., 2016). However, solely bottom-up inventories provide information on CO_2 fluxes because there are inherent difficulties in the top-down inverse modelling approach, caused by the fact that CO_2 fluxes come from many different sources. Therefore, the work of this thesis develops the first CO_2 emissions estimates for the UK using a top-down inverse modelling approach, albeit focussed on biospheric fluxes. These estimates are to be found in Chapter 3.

The hierarchical Bayesian trans-dimensional MCMC inversion set-up described in Sect. 1.4.8 has been developed for GHGs that only have anthropogenic influence and no natural sources. As will be further discussed in Chapter 2, there are many characteristics unique to CO_2 that require some adaptations to a standard atmospheric inversion framework. As such, the work of Chapter 2 focusses on the methodological advancements needed to support the UK biospheric CO_2 emissions estimation in Chapter 3.

Finally, although regional inversion systems have undergone major developments in the last decade, they have suffered from a lack of intercomparison studies. During this PhD project, the opportunity has arisen to participate in one such intercomparison project focussing on European biospheric fluxes, offering the chance to test the inversion set up developed in Chapters 2 and 3 against other more mature CO_2 inversion systems. The results that have been generated by this system through the intercomparison process are explored in Chapter 4. Since the work of Chapter 3, focussing on the UK, and the work of Chapter 4, focussing on Europe, overlap, a synthesis of the results of these chapters is presented in Chapter 5.

This thesis is therefore a first step towards CO_2 flux estimation using the inverse framework described here. It is hoped that through this work, a better understanding of UK biospheric CO_2 fluxes can be achieved, as well as a better understanding of how a CO_2 inversion can be set up within this framework.

Chapter 2

Adapting an inverse system for carbon dioxide flux estimation

2.1 Introduction

In this chapter, the hierarchical Bayesian trans-dimensional MCMC approach described in Sect. 1.4.8 is adapted to meet the needs of a CO_2 inversion. Performing atmospheric inversions for CO_2 poses a unique set of challenges, which are described in the following paragraphs. The new system is then tested, as described in the rest of this chapter. This is the first concerted effort to use the NAME atmospheric dispersion model along with a hierarchical Bayesian inversion to estimate fluxes of CO_2 and the method developed here forms the basis of the work of Chapters 3 and 4. The final set-up is described in Section 2.2 and the rationale behind this set-up is explored in a number of tests using synthetic data in Section 2.3. The method developed in this chapter features in White et al. (2019).

The key challenges associated with estimating fluxes of CO_2 that are not necessarily present with other GHGs are that: there are multiple co-located sources that are highly spatially variable; CO_2 has a strong diurnal and seasonal cycle associated with biospheric fluxes (and anthropogenic fluxes to a smaller extent); and, due to the existence of sinks as well as sources, the flux to the atmosphere can be negative.

In Sect. 1.1 the complex interplay of the biospheric, oceanic and anthropogenic components of the carbon cycle is described. These different, often co-located, sources make it very difficult to disentangle the contributions of the separate sources to the observations. The biospheric flux is by far the largest component, and net ecosystem exchange (NEE) is composed of positive fluxes to the atmosphere (or sources) from terrestrial ecosystem respiration (TER, a combination of autotrophic and heterotrophic respiration) and negative fluxes to the atmosphere (or sinks) from gross primary productivity (GPP). The relationship between these three fluxes is given in Eq. 2.1.

$$NEE = TER - GPP \tag{2.1}$$

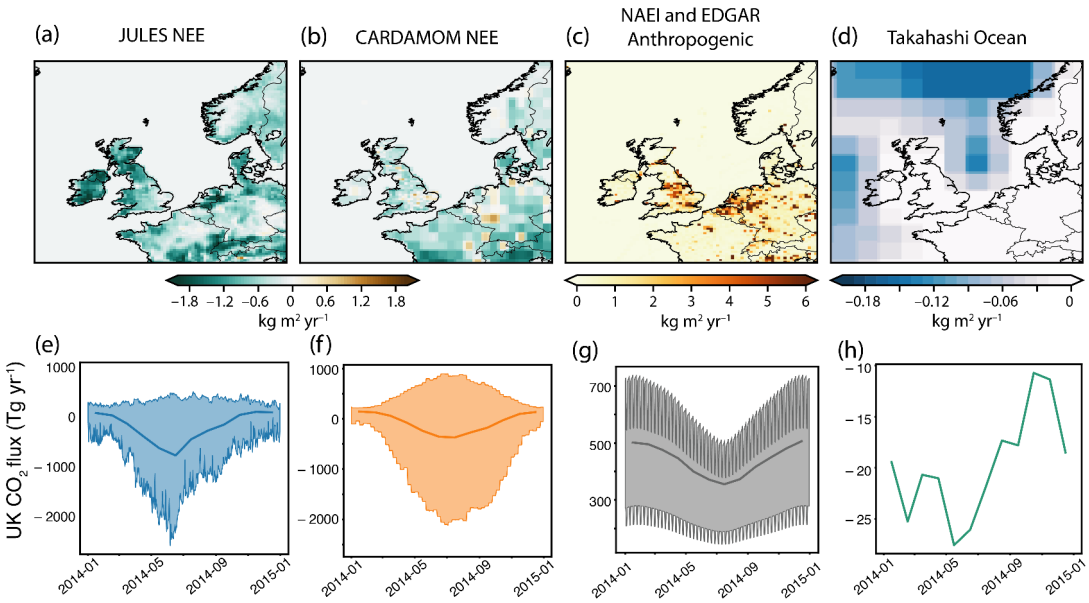

Fig. 2.1: Top: maps of average NEE CO_2 fluxes in 2014 from JULES and CARDAMOM, anthropogenic emissions from NAEI (UK) and EDGAR (outside UK), and ocean fluxes from Takahashi et al. (2009). All datasets have been regridded to the resolution of NAME model output from their native resolution (given in Table 2.2). Bottom: time-series of UK CO_2 fluxes throughout 2014. Solid line represents monthly fluxes and shading represents the diurnal range.

According to the CARDAMOM and JULES models of biospheric fluxes, monthly mean fluxes of TER and GPP are on the order of +/- 10^3 Tg yr^{-1} respectively at their seasonal maximum over the UK. In contrast, annual anthropogenic fluxes are on the order of 10^2 Tg yr^{-1} over the UK according to the NAEI (http://naei.beis.gov.uk), which can be similar to the UK's monthly NEE flux at the seasonal maximum. UK coastal ocean fluxes are on the order of 10^1 Tg yr^{-1} (Takahashi et al., 2009), which is similar to the UK's annual NEE flux. These fluxes are illustrated in Fig 2.1, note the different scales on the y-axes. Given the dominant seasonal cycle in biospheric fluxes, many inverse modelling studies of CO_2 flux typically focus on estimating biospheric fluxes and assume that anthropogenic fluxes are "fixed" in the inversion (e.g. Kountouris et al., 2018a; Meesters et al., 2012). This assumption is made since the uncertainties in anthropogenic fluxes are thought to be low compared to those of the biospheric fluxes, although this may not necessarily be the case as there can be significant discrepancies between different anthropogenic emissions inventories (Peylin et al., 2011).

To address the challenges in separating sources, some researchers have looked at concentrations of isotopes or co-emitted gasses to ascertain source signatures in CO_2 mole fractions. Whilst biospheric fluxes are the focus of this work, these methods hold promise for future work and are woth mentioning here. Radiocarbon, ^{14}C, is completely depleted in fossil fuels compared to biospheric and oceanic carbon pools, so measurements of atmospheric $\Delta^{14}C$ taken alongside measurements of CO_2 have been used to isolate fossil fuel CO_2 concentrations (e.g. Miller et al., 2012; Turnbull et al., 2011a; Xueref-

Remy et al., 2018). However, measurements of ^{14}C are expensive so can only be made infrequently across a sparse network. Carbon monoxide (CO) is released during incomplete combustion so also provides a way to separate the contribution of biospheric and anthropogenic sources to CO_2 concentrations (e.g. Laan et al., 2010; Turnbull et al., 2011b). However, due to large uncertainties in the CO:CO_2 source ratio, CO measurements usually need to be combined with ^{14}C measurements. The atmospheric potential oxygen (APO) method is based on the fact that there are different O_2:CO_2 ratios for biospheric and anthropogenic fluxes and can be used independently of CO and ^{14}C (Pickers, 2016). Along with tracers for anthropogenic emissions, methods have also been developed to distinguish the different biospheric processes. Carbonyl sulphide (COS) is taken up by plants during photosynthesis and since this is the dominant process by which it is removed from the atmosphere it can be used to isolate fluxes of GPP (e.g. Campbell et al., 2017; Suntharalingam et al., 2008; Wang et al., 2016).

Along with a large seasonal cycle, atmosphere-biosphere CO_2 exchange has an even more pronounced diurnal flux cycle, and both temporal flux cycles are orders of magnitude greater than the annual net flux (see the difference in magnitude between the diurnal range and monthly means of NEE in Fig. 2.1). Denning et al. (1996) was the first to explore the importance of coupling diurnal cycles in fluxes and atmospheric transport finding that, in comparison to using monthly average CO_2 fluxes, the diurnal cycle of simulated mole fractions was greatly improved and could match that of the observations. This is in order to represent the "diurnal rectifier effect" - the fact that both atmospheric transport and photosynthesis and respiration cycles are driven by solar radiaton leading to higher CO_2 concentrations at the surface and lower concentrations at higher altitudes. This is because photosynthesis occurs in the day when there is deep convection in the boundary layer (lowering CO_2 concentrations in the boundary layer) whereas respiration occurs at night when generally only shallow mixing takes place (increasing CO_2 concentrations close to the surface). Gerbig et al. (2003b) then developed an analysis framework for regional scale CO_2 flux inversions, building on the work of Denning et al. (1996). The study sets out the need to explicitly simulate the diurnal cycle of biospheric fluxes and highlights the importance of high spatial and temporal resolution data when addressing the unique problems of representation and aggregation errors caused by the highly varying nature of CO_2 fluxes in both space and time.

GPP and TER can be very large fluxes (according to the CARDAMOM model the minimum monthly GPP over the UK is -1200 Tg CO_2 yr^{-1} and the maximum monthly TER is 1000 Tg CO_2 yr^{-1}), whilst the net flux is much smaller in comparison (with a monthly minimum over the UK of -400 Tg CO_2 yr^{-1} and maximum of 100 Tg CO_2 yr^{-1}). The daily transition from positive to negative net flux is also unique to CO_2 inversions and, depending on the system, may be problematic. Many inverse systems scale NEE as a single variable in their inversions (e.g. Kountouris et al., 2018a; Steinkamp et al., 2017). However, in a synthetic data study in which biospheric CO_2 was inferred, Tolk et al. (2011) found that separately solving for positive fluxes (TER) and negative fluxes (GPP) in atmospheric inversions provided a better fit to the atmospheric mole fraction data than inversions that scaled NEE only. This separation has been applied in various studies demonstrating model set-ups

Table 2.1: Measurement site information. The location of sites is also shown in Fig. 1.4a. *Weybourne data is used for validation of the results only and is not included in the inversions. LSCE – Laboratoire des Sciences du Climat et de l'Environnement, DECC – Deriving Emissions related to Climate Change, GAUGE – Greenhouse gAs Uk and Global Emissions, UEA – University of East Anglia.

Site	Site code	Location	Inlet Height (m above ground level)	Network
Mace Head	MHD	53.327 °N, 9.904 °W	24	LSCE
Ridge Hill	RGL	51.998 °N, 2.540 °W	90	DECC
Tacolneston	TAC	52.518 °N, 1.139 °E	185	DECC
Heathfield	HFD	50.977 °N, 0.231 °E	100	GAUGE
Bilsdale	BSD	54.359 °N, 1.150 °W	248	GAUGE
Angus	TTA	56.555 °N, 2.986 °W	222	DECC
**Weybourne*	*WAO*	*52.950 °N, 1.122 °E*	*10*	*UEA*

with synthetic data, for example: geostatistical approaches (Göckede et al., 2010), ensemble Kalman filter methods (Lokupitiya et al., 2008; Zupanski et al., 2007) and Bayesian synthesis methods (Schuh et al., 2009). Yet, despite the apparent improvement in performance, this separation is not routinely used in CO_2 inversions as there are only a limited number of real data studies where it has been implemented (e.g. Gerbig et al., 2003a; Matross et al., 2006; Meesters et al., 2012; Schuh et al., 2010). This issue is given particular attention throughout this thesis.

2.2 Method

This section describes the set-up that has been developed for CO_2 estimation, responding to many of the challenges that have been introduced. The decisions that have been made leading to the final set up will be further explored in a suite of tests using synthetic data that follow this section. The set-up for the synthetic tests is described in Section 2.2.5.

2.2.1 Data

Although the results presented in this chapter are based on synthetic data, an appreciation of the observations is essential to understand some of the difficulties of modelling CO_2 fluxes. Studies using real data will follow in Chapters 3 and 4. The synthetic data used in this chapter represents the same six measurement sites and inlet heights (the highest available) as the work in Chapter 3, which are detailed in Table 2.1. The locations of these measurements sites are shown in Fig. 1.4a.

Figure 2.2 shows the mole fraction measurements available for the six sites during the period 2013-2014, averaged to weekly bins. Gaps in the data are where the site was not yet in operation or was experiencing downtime due to instrument disruption. Mace Head (MHD) is a background site, mostly measuring "clean" background air that has come over the Atlantic ocean, which is why the concentrations seen here (Fig. 2.2c) are some of the lowest across all sites. The small variability

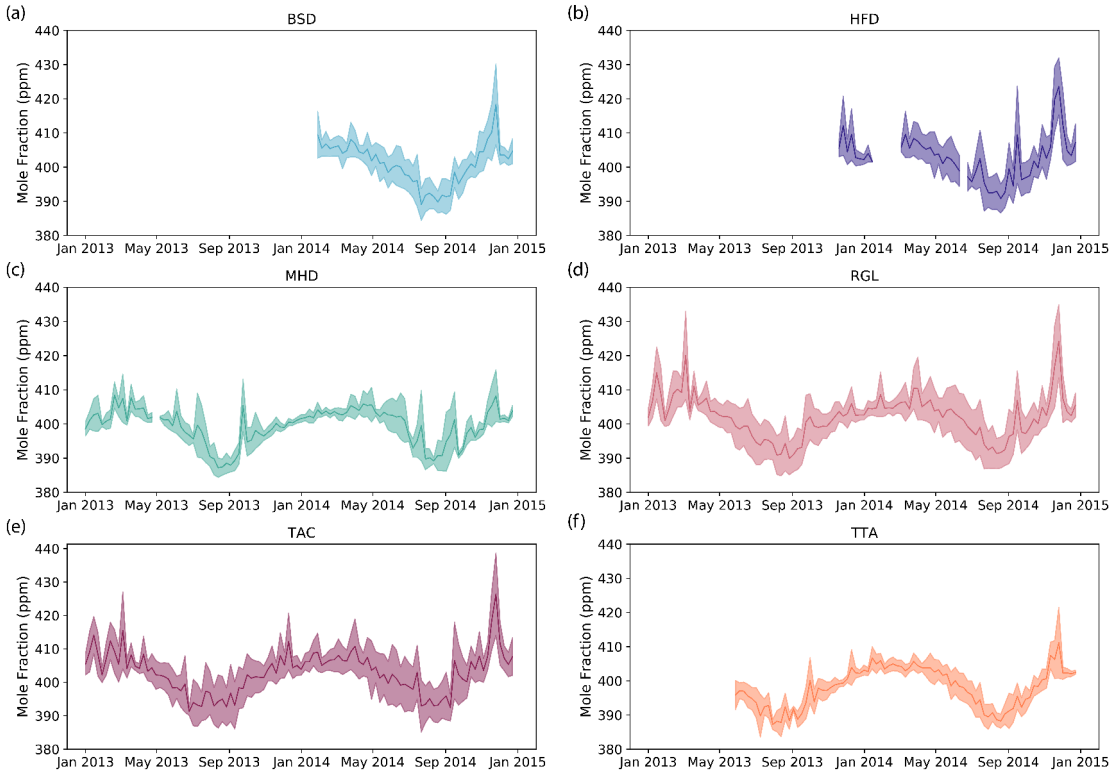

Fig. 2.2: Data collected at the six measurement sites in the DECC and GAUGE networks. Data is averaged to weekly and the shading represents the standard deviation of the measurements taken in each week period.

at MHD is explained by the lack of pollution events measured there. Observations at Angus (TTA, Fig. 2.2f) are similarly low, indicating that it too lacks strong pollution sources nearby. The other sites are often sampling the enhancement of CO_2 concentrations due to human activity or ecosystem respiration over the UK.

Unlike other GHGs, there is a clear seasonal cycle seen in the observational CO_2 data. This is characterised at most sites by a steep decline in atmospheric concentration between June and August, a sharp turning point in August, a steep increase again between August and November and a comparatively smooth turning point between December and May. Measurements at Tacolneston (TAC, Fig. 2.2e) seem to be an exception to this in that the summer turning point is much smoother, occurring between July and September. Peaks in CO_2 concentration can reach roughly 30ppm above baseline and one that seems to be seen across all measurement sites occurs in November 2015. This is a period of particularly stagnant meteorological conditions across the UK, which means that emissions at that time will accumulate in the atmosphere without being dispersed.

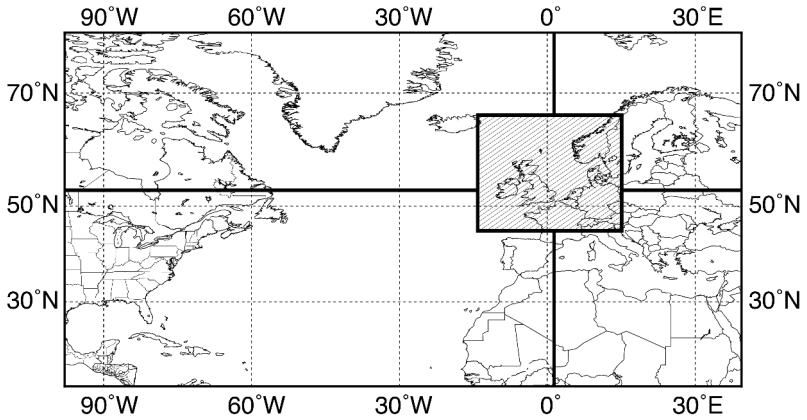

Fig. 2.3: The domain used to calculate NAME footprints. The boxes relate to the basis functions that are scaled in the inversion, described in Sect. 2.2.4.1. The four edge boxes correspond to four basis functions. The hatched box is the main area of focus for the synthetic studies and, in most tests, basis functions in this area are based on a fractional map of 6–7 different plant functional types (PFTs).

2.2.2 Atmospheric transport model

The Lagrangian atmospheric transport model, or LPDM, NAME is used in this work and is introduced in Section 1.4.3.1. The domain used to calculate atmospheric transport covers most of Europe, the east coast of North and Central America and North Africa (-97.9° - 39.38° longitude and 10.729° - 79.057° latitude) and is shown in Fig. 2.3. At each two-hourly measurement time step, the model releases 20,000 particles, which are tracked back in time for 30 days, so that by the end of this period the majority of particles will have left the model domain. Since most CO_2 flux to the atmosphere occurs at the surface, the instances where the particles are in the lowest 40m of the atmosphere are recorded and it is assumed that this represents the sensitivity of observed mole fractions to surface fluxes in the inversion domain, when integrated over time.

2.2.2.1 Adapting NAME footprints for rapidly varying fluxes

In many previous inverse modelling studies using LPDMs (e.g. Manning et al., 2011; Steinkamp et al., 2017; Thompson and Stohl, 2014) the footprint is assumed to be equal to the integrated air history over the duration of the simulation (e.g. 30 days). Based on the assumption that fluxes have not changed substantially during the 30-day period, the integrated footprint can be multiplied by the prior flux and summed over all the grid cells in the domain to create a time series of modelled mole fractions at each measurement site.

Integrated NAME footprints have been used for CO_2 simulations in Steinkamp et al. (2017), with twice-daily data, 4 day back-trajectories and weekly prior flux estimates. However, many CO_2 inverse modelling studies using other LPDMs will disaggregate footprints back in time, capturing changes in surface sensitivity on timescales shorter than the duration of the simulation, to cope with sub-daily

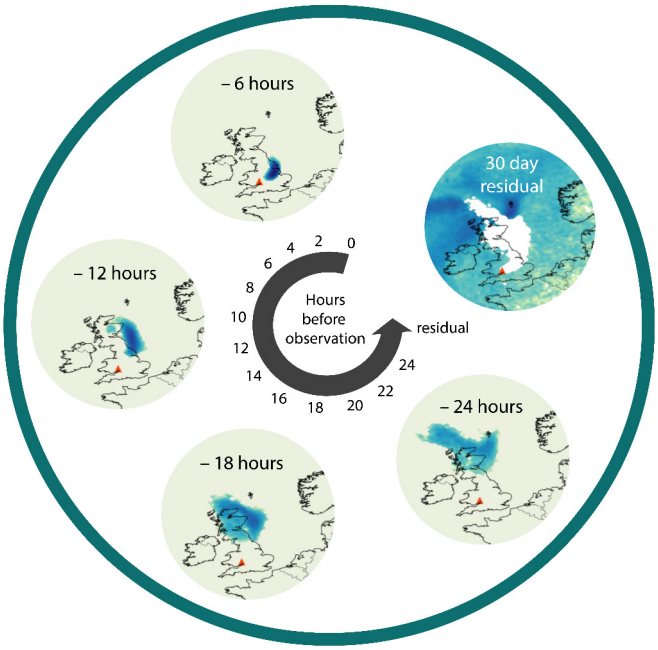

Fig. 2.4: The breakdown of NAME footprints that constitute the atmospheric transport of CO_2 to a measurement site for one 2-hourly measurement period.

varying CO_2 fluxes (Gerbig et al., 2003b; Gourdji et al., 2010) as per Denning et al. (1996). Thus far, a disaggregation such as this has not been used in NAME simulations, so the development of a suitable method has formed part of this work.

Instead of having one footprint that represents a 30-day air history, the footprints are determined for each 2-hourly average period back in time for the first 24 hours before an observation. These 24 hours of disaggregated footprints then replace the first 24 hours of integrated sensitivities (Fig. 2.4). This means that mole fractions can be simulated by multiplying the 24 hours of disaggregated footprints by biospheric flux estimates for the corresponding time, so that the ~hourly variability in the source or sink of CO_2 is represented in the modelled observations. The remaining integrated footprint is multiplied by the monthly average flux, based on the assumption that this only incurs minor errors in the simulated mole fractions. This is demonstrated in Eq. 2.2, which yields the modelled mole fraction, y_t, for one 2-hourly measurement time step, t, at one measurement site.

$$y_t = \sum_{i=0}^{12} \sum_{j=0}^{n} fp_{t-i,j} \times q_{t-i,j} + \sum_{j=0}^{n} fp_{remainder_j} \times q_{month_j} \tag{2.2}$$

Here i denotes the number of 2-hour periods back in time before the particle release at time t and j represents the grid cell where n is the total number of grid cells; $fp_{t-i,j}$ is one grid cell of the two-dimensional time-disaggregated footprint corresponding to the 2-hourly period back in time; $q_{t-i,j}$ is one grid cell of the two-dimensional, two-hourly flux field corresponding to the same time;

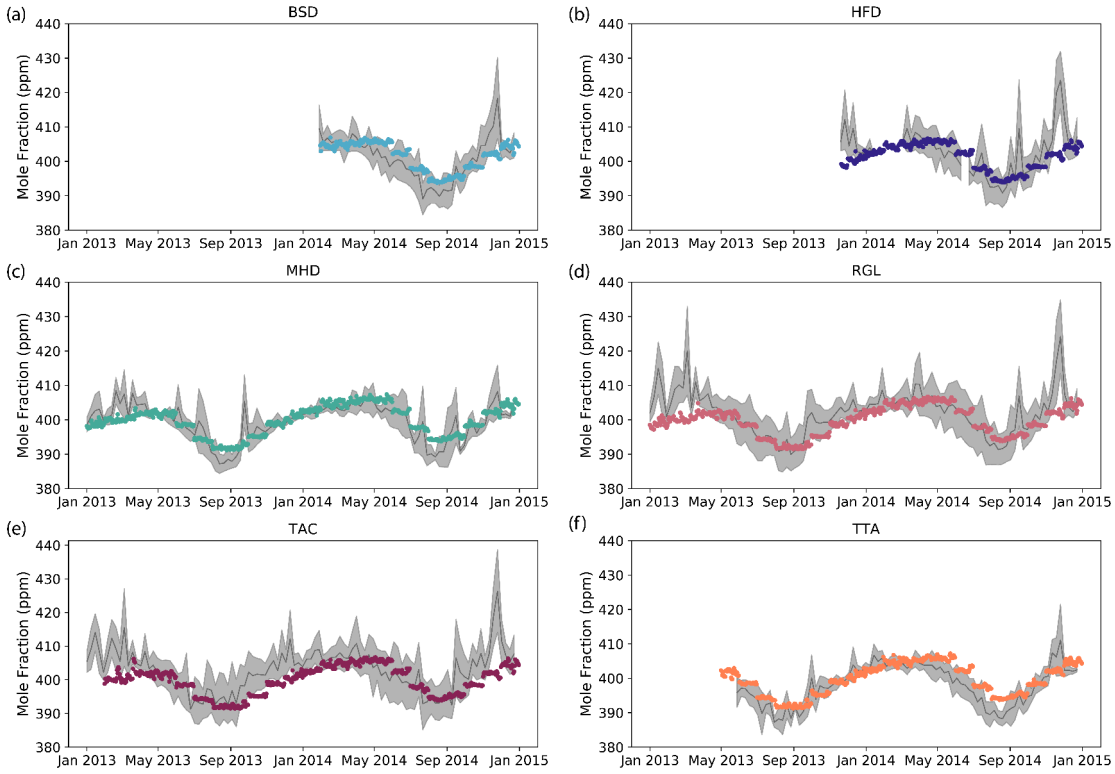

Fig. 2.5: Prior mean modelled baseline CO_2 concentrations at six measurement sites.

$fp_{remainder_j}$ is one grid cell of the remaining 29 day footprint and q_{month_j} is one grid cell of the monthly average flux.

An investigation of the impact of disaggregating footprints further back in time and a demonstration of why the disaggregation is necessary is the focus of "Test 1" in Section 2.3.2. The other tests use synthetic data created using footprints that have been disaggregated for the first 24 hours (as above) so the impact of this decision cannot be seen in those results.

2.2.2.2 Baseline

As discussed in Sect. 1.4.3, NAME is a regional model, so a set of boundary conditions is required to estimate baseline CO_2 concentrations of air before it enters the NAME domain. In the NAME simulation, when particles leave the model domain the time and location of their exit point is recorded. The Eulerian model MOZART (Emmons et al., 2010), described in Sect. 1.4.3.2, is then used to find the concentration of CO_2 at these locations to serve as prior boundary conditions. Figure 2.5 shows the prior mean modelled baseline at the six measurement sites. During the inversion, the mole fraction at each domain edge (N, E, S, W) is scaled up or down to account for uncertainties in the MOZART boundary conditions (Lunt et al., 2016).

The MOZART output used in this work was from a run using GEOS-5 meteorology (Rienecker et al., 2011) and global biospheric fluxes from the NASA-CASA biosphere model (Potter, 1999), global ocean fluxes from Takahashi et al. (2009) and global anthropogenic fluxes from the Emission Database for Global Atmospheric Research (EDGAR, EC-JRC/PBL, 2011). Since MOZART tends to produce baseline concentrations that are too high, the global MOZART initial mole fraction field for January 2014 was scaled down before commencing the 2014 MOZART run in order to match the surface South Pole value to the mean NOAA January 2014 flask value (Dlugokencky et al., 2018). This same scaling (the factor required to reconcile the MOZART concentrations at the South Pole with those of flask observations) was then also applied to any pre-January 2014 MOZART output, ensuring that the South Pole values in the MOZART output were consistent, to prevent discontinuities in the boundary mole fraction fields.

A sensitivity test has been carried out to assess the impact of assigning prior boundary conditions in this way. 1ppm was added or taken away from the mole fractions at the domain edges and it was found that in June a $\pm$1ppm change translates to a 1-3% change in the inversion result and in December a $\pm$1ppm change translates to a 7-11% change in the inversion result. These changes are substantially smaller than the posterior uncertainty, indicating that the choice of prior boundary conditions has a negligible impact on the result of the inversion.

2.2.2.3 Data filtering

LPDMs are known to perform poorly under certain meteorological conditions. In particular, it is often assumed that model-data mismatch should be smallest during periods when the boundary layer is relatively well mixed. A common approach is to only include daytime data in the inversion (e.g. Kountouris et al., 2018a; Meesters et al., 2012; Steinkamp et al., 2017) or separate morning and afternoon averages (e.g. Matross et al., 2006). To make use of as much high frequency measurement information as possible, a filter based on two metrics has been used in this work to remove times of high atmospheric stability and/or stagnant conditions. This is referred to as the "local-lapse" filter. The first metric is based on calculating the ratio of the NAME footprint magnitude in the 25 grid boxes in the immediate vicinity of the measurement station to the total for all of the grid boxes in the domain. A high ratio indicates times when a significant fraction of air influencing the observation point originates from very local sources, which may not be resolved by the model (Lunt et al., 2016). The second metric is based on the modelled lapse rate at each site, which describes the rate of change in temperature with height in the atmosphere. This a measure of atmospheric stability. A high lapse rate, i.e. a large change of temperature with height, suggests very stable conditions because the air is very stratified and this would be conducive for significant influence from local sources on the measurement. However, a low lapse rate suggests that the air is well mixed (because temperature is not changing so rapidly with height in the atmosphere) and this means that the measurement station can monitor CO_2 concentrations resulting from emissions sources further from the measurement location. Thresholds for each of these criteria were chosen to preserve as much data as possible, whilst

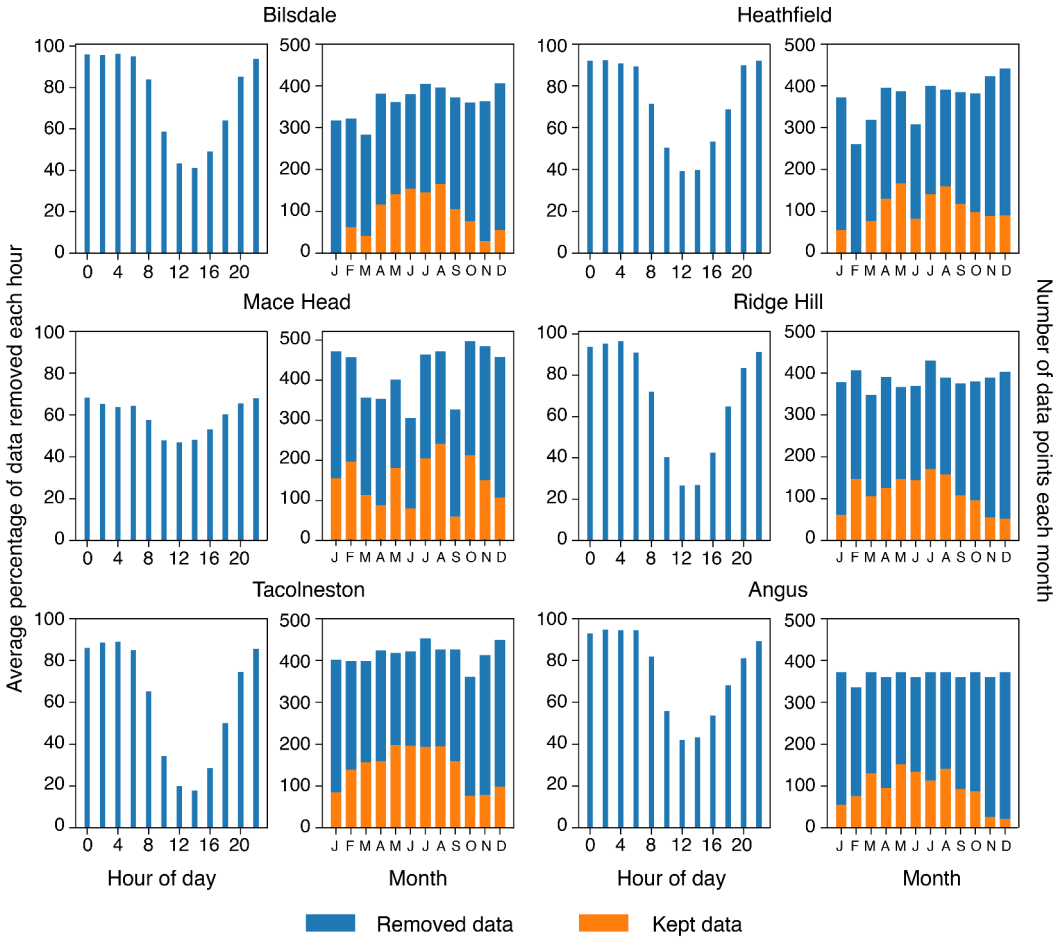

Fig. 2.6: Data filtered out in 2014 using the "local-lapse" filter. Left hand bar charts for each site show the average percentage of data removed for each 2-hour period in the day. Right hand bar charts for each site show the number of data points used in the inversion for each month (orange bars) and the number of data points removed prior to the inversion for each month (blue bars).

retaining only points that the model was (somewhat subjectively) found to resolve well. Figure 2.6 shows how much data has been removed for each site in 2014. A comparison of different data filters, including those used in other inverse modelling studies, is carried out in "Test 5" in Section 2.3.6.

2.2.2.4 Model-measurement uncertainty

Model-measurement uncertainty (or model-data mismatch) has a measurement uncertainty component and a component that takes into account the ability of the model to represent real atmospheric conditions. In these synthetic tests the synthetic measurements are assigned a fixed monthly uncertainty, relative to the monthly average synthetic mole fraction, that resembles the uncertainty of observational data. The model uncertainty is a poorly constrained quantity so a priori it is given a uniform distribution based on an appropriate range of values. The measurement uncertainty is added to the

Table 2.2: Specifications for different priors.

	Spatial Resolution	Temporal Resolution
Biogenic fluxes		
JULES	0.25° x 0.25°	2-hourly
CARDAMOM	25 km x 25 km	2-hourly
	(1° x 1° outside the UK)	
Anthropogenic fluxes		
NAEI (UK)	1 km x 1 km	2-hourly
EDGAR (outside UK)	0.1° x 0.1°	Yearly (using 2010)
Ocean fluxes	4° x 5°	Monthly (climatology)

uniform prior distribution for model uncertainty and together they make up the model-measurement uncertainty, which is one of the hyper-parameters solved in the inversion (see Table 2.3).

2.2.3 Models of CO_2 fluxes

In this work, bottom-up estimates of flux sources are required to provide prior information for the inversion. Figure 2.1 shows the spatial and temporal distribution of biospheric, anthropogenic and oceanic CO_2 sources from four different bottom-up datasets and Table 2.2 gives their spatial and temporal resolution.

NEE estimates are from the Joint UK Land Environment Simulator (JULES) and CARbon DAta MOdel fraMework (CARDAMOM). JULES is a physically based, process driven model that estimates the energy, water and carbon fluxes at the land-atmosphere boundary (Best et al., 2011; Clark et al., 2011). CARDAMOM, on the other hand, is a model-data fusion framework ingesting satellite based remotely sensed estimates of the state of terrestrial ecosystems to retrieve process parameters for the DALEC carbon balance model (Bloom et al., 2016; Bloom and Williams, 2015; Smallman et al., 2017). A more thorough description of the two models and analysis of the differences between them is given in Chapter 3.

Estimates of fluxes due to anthropogenic activity within the UK were obtained from the NAEI (http://naei.beis.gov.uk). The NAEI provides a yearly estimate of emissions, which has been disaggregated into a 2-hourly product based on temporal patterns in activity data and varies on diurnal, weekly and seasonal scales. The inventory emissions were disaggregated according to the UN-ECE/CORINAIR Selected Nomenclature for sources of Air Pollution (SNAP) sectors (UNECE/EMEP, 2001). Outside the UK, anthropogenic emissions are from EDGAR v4.2 FT2010 inventory data for 2010 (EC-JRC/PBL, 2011). This is a fixed 2D map that is used throughout the inversion period. Within the UK, the NAEI and EDGAR fluxes differ by around 15% (540 Tg CO_2 yr^{-1} for EDGAR, 460 Tg

Table 2.3: Probability density functions (PDFs) for parameter and hyper-parameter scaling factors. Mean and st. dev. in fourth and fifth columns relate to lognormal PDFs, lower bound and upper bound relate to uniform PDFs.

Parameter		PDF	Mean / lower bound	St. dev. / upper bound
Prior uncertainty				
GPP	x_{GPP}	Lognormal	1	1
	$\sigma_{x_{GPP}}$	Uniform	0.1	1.5
TER	x_{TER}	Lognormal	1	1
	$\sigma_{x_{TER}}$	Uniform	0.1	1.5
Boundary conditions	x_{BC}	Lognormal	1	1
	$\sigma_{x_{BC}}$	Uniform	0.01	0.05
Model-measurement representation uncertainty				
Standard deviation	σ_y	Uniform	0.9 ppm	45 ppm
Correlation timescale	τ	Uniform	1 hour	120 hours

CO_2 yr^{-1} for NAEI), however UK fluxes are not found to be significantly affected by perturbations of this magnitude applied to anthropogenic emissions outside the UK.

Prior ocean flux estimates are from Takahashi et al. (2009). They are based on a climatology of surface ocean partial pressure of CO_2 (pCO_2) constructed using measurements taken between 1970 and 2008. The monthly UK coastal ocean flux in Fig. 2.1h is calculated within the UK's exclusive economic zone.

The plots of monthly UK CO_2 fluxes and diurnal range in Fig. 2.1 highlight the differences in magnitude of the three flux sources. The NAEI anthropogenic emissions inventory has a reported uncertainty of around 5%, in contrast to the models of biospheric fluxes where uncertainty estimates are difficult to calculate. Due to the difficulty of separating sources and the large biospheric flux uncertainty, this work will mainly focus on biospheric fluxes as many previous studies have done. In these cases, anthropogenic and oceanic fluxes will be fixed and will not be updated in the inversion. The positive and negative biospheric fluxes, TER and GPP, are solved separately, and then combined a posteriori to determine NEE. The rationale for this is explored in "Test 2" in Section 2.3.3. The difficulties of attempting to solve for anthropogenic fluxes alongside biospheric fluxes are demonstrated in "Test 3" in Section 2.3.4.

2.2.4 Inversion set-up

The inversion method used follows the hierarchical Bayesian trans-dimensional MCMC inversion introduced in Sect. 1.4.8. The hyper-parameters are defined as in Table 2.3 along with the prior PDFs used to describe them in this inversion set-up. Lognormal PDFs are chosen for the GPP, TER and BC parameters, as opposed to Gaussian distributions for example, because it is impossible for these parameters to change sign, i.e. the fluxes/concentrations can only be either positive or negative. For the other parameters a simple uniform distribution has been chosen as there is less information about the range of possible prior values. Mean/lower bound and standard deviation/upper bound values were chosen based on a number of factors: the range of estimates found in the literature, an understanding of where in the parameter space the inverse system feels most comfortable (i.e. if a parameter was given uncertainty bounds that were not covering an appropriate range the system would predict scaling factors bunched around the highest or lowest possible values), and the plausibility of posterior results and uncertainty estimates. In this work, the trans-dimensional method is adapted to keep a fixed set of regional basis functions (described in Sect. 2.2.4.1) but allow the inversion to have a variable *time* rather than *space* dimension. The inversion calculations are performed over one month at a time, but with the trans-dimensional case in *time*, multiple scaling factors for each fixed region are found over the course of the inversion, down to a minimum daily resolution, increasing the effective temporal resolution of the inversion. Therefore, in this case k from Eqn. 1.11 is more specifically the unknown number of time periods resolved in the inversion. This is believed to be important for the highly variable temporal nature of CO_2 fluxes and is further explored in "Test 4" in Section 2.3.5.

The MCMC algorithm had a burn-in period of $5\text{x}10^4$ iterations, to allow the system to forget about the initial prior constraints, and was then run for an additional $2\text{x}10^5$ iterations to appropriately explore the posterior distribution. With an MCMC algorithm, appropriately exploring the posterior distribution and converging on a solution involves frequently accepting new values for each parameter within a large range of the proposed prior distribution. This behaviour manifests itself as a noisy, well-mixed "chain" of possible parameter values across the number of iterations that doesn't appear to be drifting towards higher or lower values. Therefore, the trace of each chain was examined qualitatively for these characteristics to ensure that the algorithm had been run for a sufficient number of iterations to converge on a result.

The likelihood function used for this inversion set-up takes a Gaussian form, as in Eq. 1.8. The form of the other components of Eq. 1.11 can be found in Lunt et al. (2016).

2.2.4.1 Basis functions

The domain is split into five spatial regions separating west-central Europe from north-east, south-east, south-west and north-west regions, shown in Fig. 2.3. Within the West-Central Europe area (the hashed region in Fig. 2.3), a map of the fraction of different plant functional types (PFTs) in each grid cell has been used to further break down the region (Fig. 2.7). This is the same PFT map used in the

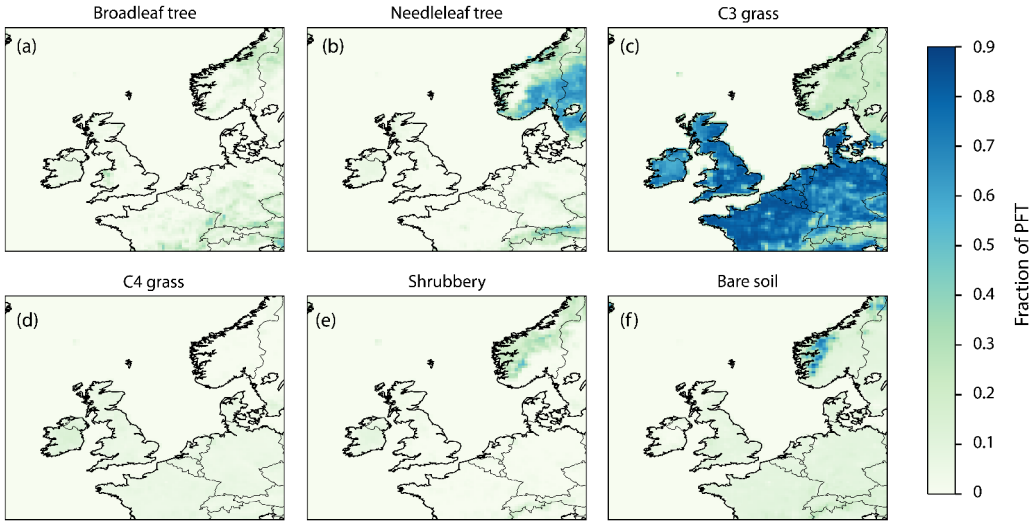

Fig. 2.7: Maps showing the fraction of each plant functional type (PFT) over the sub-domain.

JULES biospheric simulation (see Sect. 3.2.2.2). Scaling factors are derived in the inversion to scale GPP and TER within maps of five or six PFTs: broadleaf tree, needleleaf tree, C3 grasses, C4 grasses, shrubland and, in the case of TER, bare soil. As seen in Fig. 2.7, C3 grass is the dominant PFT over the UK, however scaling the PFTs separately adds a degree of flexibility to the inversion based on physical characteristics (as opposed to country boundaries, for example).

2.2.4.2 Definition of the Jacobian matrix

To create the Jacobian matrix, **H** (explained in Sect. 1.4.5), the footprints were multiplied by the prior GPP and TER fluxes separately (as per Eq. 2.2), then multiplied by the fractional map of basis functions (described in Sect. 2.2.4.1) and summed over the area covered by each basis function to create the columns of **H**. The boundary conditions were broken down by four further basis functions for each edge of the domain as explained in Sect. 2.2.2.2. The make up of **H** is illustrated in Fig. 2.8. Both the sensitivity to the boundary conditions and GPP and TER fluxes change in time, in the m dimension. Multiplying this m by n sensitivity matrix by a vector of ones of length n yields the prior modelled time-series at each site (length m). Therefore, during the inversion, this vector of ones is updated as a scaling factor, to scale up or down fluxes for each PFT and biospheric component to better agree with the data.

2.2.5 Synthetic test set-up

In the tests that follow, two-hourly synthetic data is generated using biospheric fluxes from CARDAMOM (the "true" fluxes), whilst JULES provides the the biospheric fluxes for the prior. Figures 2.1a, b, e and f show how different these two flux models are both spatially and temporally. By using different biosphere models to produce the synthetic data and the prior fluxes, instead of simply

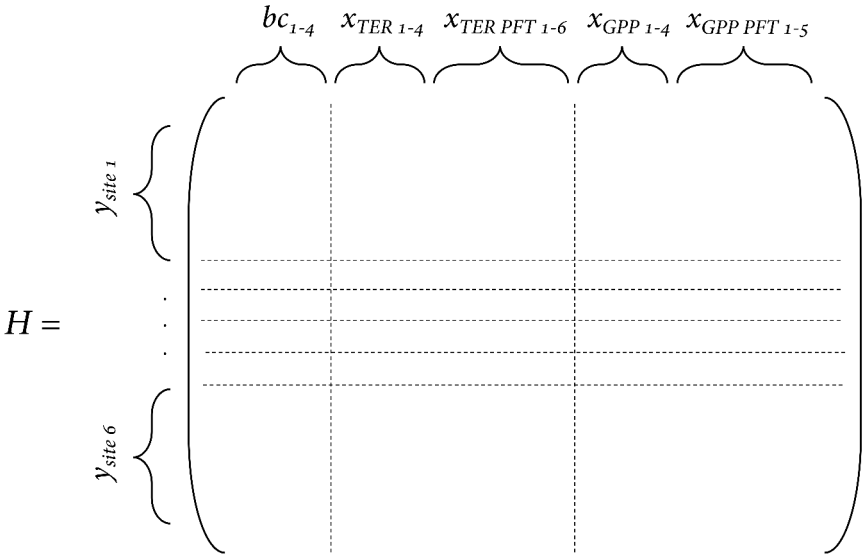

Fig. 2.8: An illustration of the components of the Jacobian (**H**) matrix. The 2-hourly measurements over the month for each measurement site are stacked on top of each other in the vertical, *m* dimension. The boundary conditions (*bc*) and fluxes (x_{TER} and x_{GPP}) along the horizontal *n* dimension have the number of columns stated in the labels (e.g. there are 4 boundary condition columns) and these relate to the basis functions for each variable (see Sect. 2.2.4.1). x_{TER} and x_{GPP} have two sets of columns as the first relates to regions north-east, south-east, south-west and north-west of the west-central Europe region and the second relates to the plant functional types used to scale x_{TER} and x_{GPP} within the west-central Europe area.

perturbing prior fluxes to generate "true" fluxes, the study allows an investigation of the underlying biosphere model structure and avoids biasing the tests in favour of one result or another depending on how perturbations are made.

2.3 Synthetic tests

2.3.1 Test 0: "Best" set-up

The "best" set-up follows the method set out in Section 2.2. Figure 2.9a shows that the posterior monthly net flux estimates are much closer to the "true" flux values than the prior, agreeing in 13 out of 24 months within the estimated 90 percentile confidence interval as opposed to 7 out of 24 months for the prior. Where the posterior estimates do not agree with the "true" fluxes within the 90 percentile confidence interval, particularly in November and December 2013 and August and December 2014, the differences could be due to the limitations of the inversion in moving between two biospheric flux estimates that have very different imposed temporal and spatial patterns.

Annual mean posterior estimates of NEE (Fig. 2.9c) agree with the "true" flux well within the estimated uncertainties. The individual TER and GPP estimates for the gross fluxes, on the other hand, do not agree with the "true" gross fluxes. This demonstrates that, although the inversion can theoretically find estimates for GPP and TER, it is not expected to estimate these correctly because they are highly spatially correlated. However, through the increased flexibilty of the inversion to apply separate scaling factors to these processes, the NEE is expected to be closer to the "truth" than the prior, which is what is seen here and was also the conclusion made in Tolk et al. (2011). Therefore, throughout this thesis the results are focussed on posterior net biospheric fluxes as opposed to the separate gross fluxes.

Whilst the posterior diurnal range of the net flux has changed considerably from the prior (Fig. 2.9b: daily maximum uptake is decreased in the first half of the year and daily maximum source is increased around summer months) there are still some differences from the "true" flux. In particular, the posterior has not been able to replicate the smooth seasonal cycle of the CARDAMOM fluxes and underestimates the daily maximum sink in late summer and autumn. In this trans-dimensional inversion the monthly inversion time period can be broken down into smaller chunks of time, however the diurnal range is probably beyond the limit that can be resolved with this system with the data available.

In terms of the spatial distribution of fluxes, Fig. 2.10b shows that, qualitatively, the difference between the posterior and "true" fluxes is smaller than the difference between the prior and "true" fluxes in Fig. 2.10a. Areas in northern Republic of Ireland, northern Scotland, Wales and eastern England have been well estimated. However, fluxes in much of the rest of England have been scaled up too much and are now slightly larger than the "true" fluxes as opposed to being slightly smaller than the "true" fluxes in the prior. Elsewhere, posterior mean fluxes are slightly smaller than the "true"

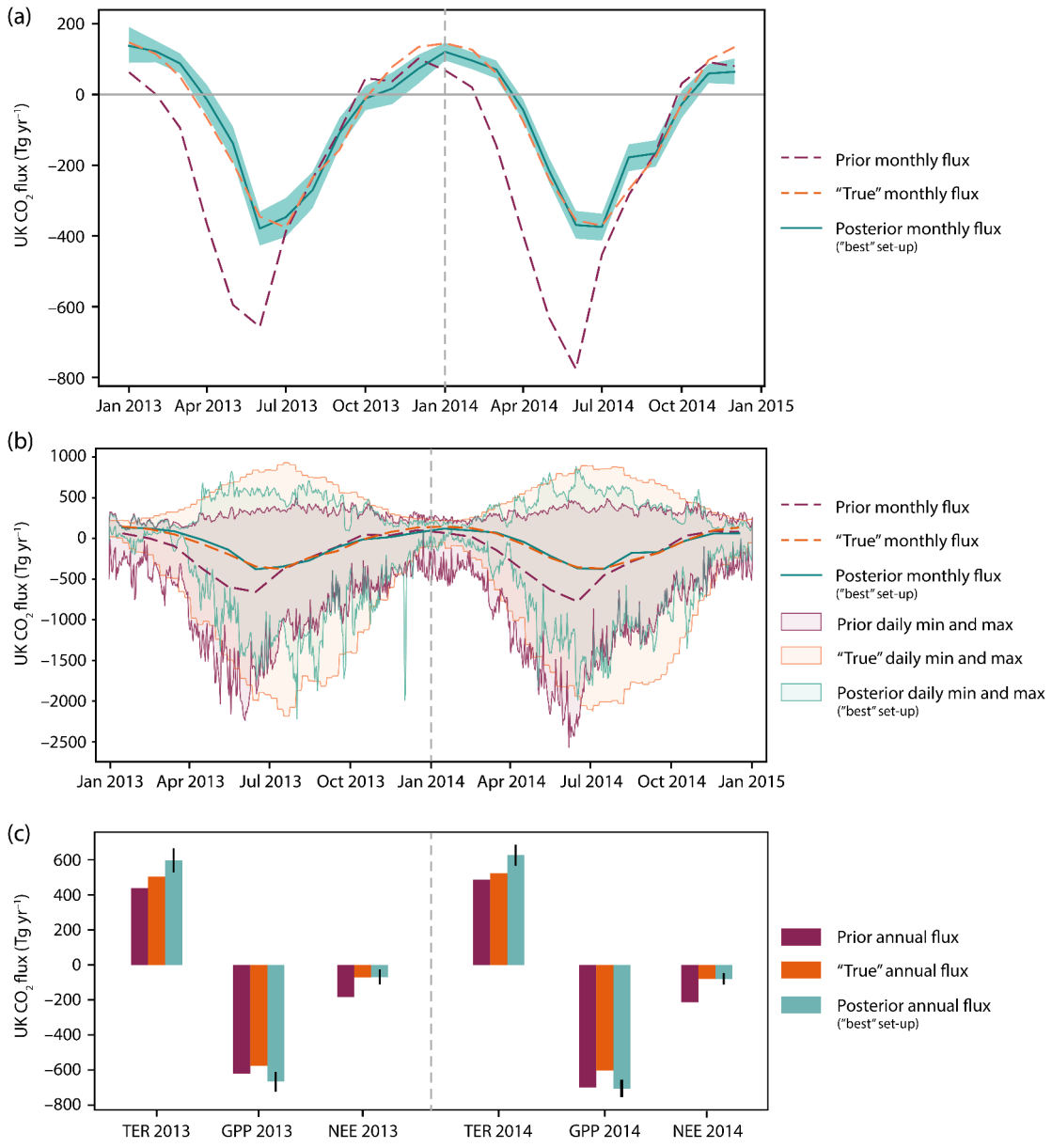

Fig. 2.9: Results of "Test 0" demonstrating the final inverse set-up. (a): Monthly average biospheric UK CO_2 fluxes. Shading represents the 5th–95th percentile. (b): Diurnal range of biospheric UK CO_2 fluxes, overlain by the monthly mean fluxes in (a). (c): Annual average biospheric UK CO_2 fluxes; error bars represent the 5th–95th percentile.

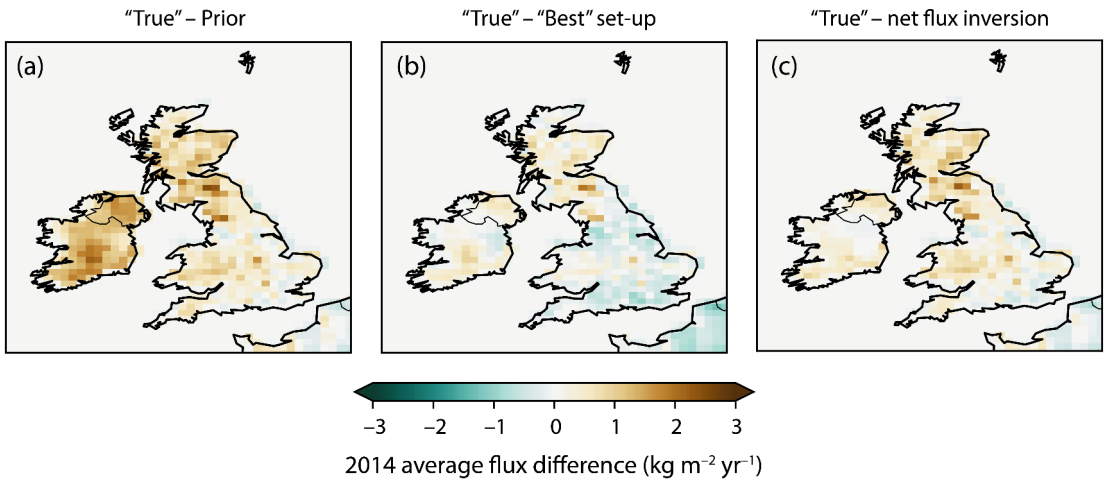

Fig. 2.10: (a): Difference between prior average 2014 flux map and "true" average 2014 flux map. (b): Difference between posterior average 2014 flux map from the "Test 0" standard inversion that scales gross fluxes and "true" average 2014 flux map. (c): Difference between posterior average 2014 flux map from the net flux inversion in "Test 2" and "true" average 2014 flux map.

fluxes although they are an improvement on the prior mean fluxes. Therefore, whilst country total estimates can be well recovered with this system, smaller scale fluxes are harder to resolve.

These inversion results are given for context in the following tests.

2.3.2 Test 1: Diurnal cycle

In this test, the choice of disaggregating only the first 24 hours of the footprint is explored and justified. Section 2.2.2.1 details the method for disaggregating NAME footprints. Assuming that disaggregating the footprint further back in time will improve the result, footprints that are disaggregated for the first 72 hours have been created for June 2014 (hereafter called 72-hours-back footprints). The impact on forward modelled mole fractions and the inversion result is presented here, along with a comparison to using integrated 30-day footprints with a monthly prior.

Figure 2.11 shows forward modelled mole fractions for integrated and disaggregated footprints along with the observations made at Ridge Hill (with the anthropogenic and coastal ocean component removed). The modelled mole fractions using integrated footprints and monthly fluxes are 12 hours out of phase with the observations and have a small amplitude, which is exactly the finding in Denning et al. (1996). Combining integrated footprints with 2-hourly fluxes over-enhances the diurnal cycle and is also slightly out of phase with observations. This is because a flux occurring at one 2 hour period (e.g. 12 noon) is constant throughout the air history for 30 days back in time, whereas 12 hours previously what was a sink of CO_2 will have become a source. Using 6-hours-back footprints (i.e. allowing the footprint to vary each 2 hours for the first 6 hours) still gives a result that is slightly out of phase from the observations, however disaggregating footprints for 12 hours upwards seems to

match the phase of the observations, implying that the diurnal cycle of CO_2 flux has the strongest impact on the mole fraction observations in the first 12 hours of transport before an observation is made. The magnitude of the observations is not captured very well here, however that is likely due to the underlying biospheric fluxes from JULES that were used to create the forward modelled mole fractions. Assuming that 72-hours-back footprints are the best option, the largest differences in the modelled mole fractions created using footprints disaggregated for 12 - 48 hours are seen at the daily maximum and minimum in certain conditions. These differences decrease as the number of hours disaggregated approaches 72.

Three inversions have been carried out for June 2014, using all six measurement sites, where the sensitivity matrix has been calculated using integrated, 24-hours-back and 72-hours-back footprints (Table 2.4). Synthetic data was created using the CARDAMOM fluxes and 72-hours-back footprints. In the two inversions that use disaggregated footprints, the posterior UK net biospheric fluxes both agree with the "true" flux and the difference between them is not statistically significant (using the 90%ile range). The inversion using the integrated footprints is not able to find the "true" flux result. The fit of modelled mole fractions to the synthetic data can be evaluated using a variety of metrics. Here, the square of the correlation coefficient (R^2), the root mean square error (RMSE) and bias statistics are calculated. R^2 evaluates how well the modelled mole fractions are able to explain the variation in the observations (in this case the synthetic data), where a high R^2 value represents a better fit. RMSE is a measure of the spread of residuals (i.e. the observations minus the modelled mole fractions), with units of ppm and a lower RMSE represents a better fit. The mean bias is calculated as the simple mean of the residuals (in ppm) and a smaller bias means a better fit. The statistics of fit to the synthetic data are given in Table 2.5. The prior fit to the data is best using 72-hours-back footprints and worst using the integrated footprints, as expected, however the statistics across all sites suggest that the prior fit is only marginally worse using the 24-hours-back footprints. Using the integrated footprints as opposed to the disaggregated footprints, R^2 calculated between synthetic data and prior modelled mole fractions can be up to around 0.3 lower (e.g. the difference between 0.56 and 0.14 at RGL), RMSE can be around 1ppm larger (e.g. the difference between 3.75 ppm and 5.34 ppm at RGL) and the mean bias can be around 1–2ppm larger (e.g. the difference between 3.4 ppm and 4.76 ppm at RGL). Like the prior fit, the posterior fit to the synthetic data using both 72 and 24-hours-back footprints is very similar, whereas the R^2 calculated between synthetic data and posterior modelled mole fractions using integrated footprints is around 0.25 lower and the RMSE is around 0.45 higher. The mean bias statistics are roughly similar across all three inversions.

Therefore, the conclusion to disaggregate the footprints for 24 hours back in time was made because, compared to 72-hours-back footprints, only minor errors in the forward simulation are incurred, the inversion results are very similar and creating the sensitivity matrix with 24-hours-back footprints is less computationally expensive.

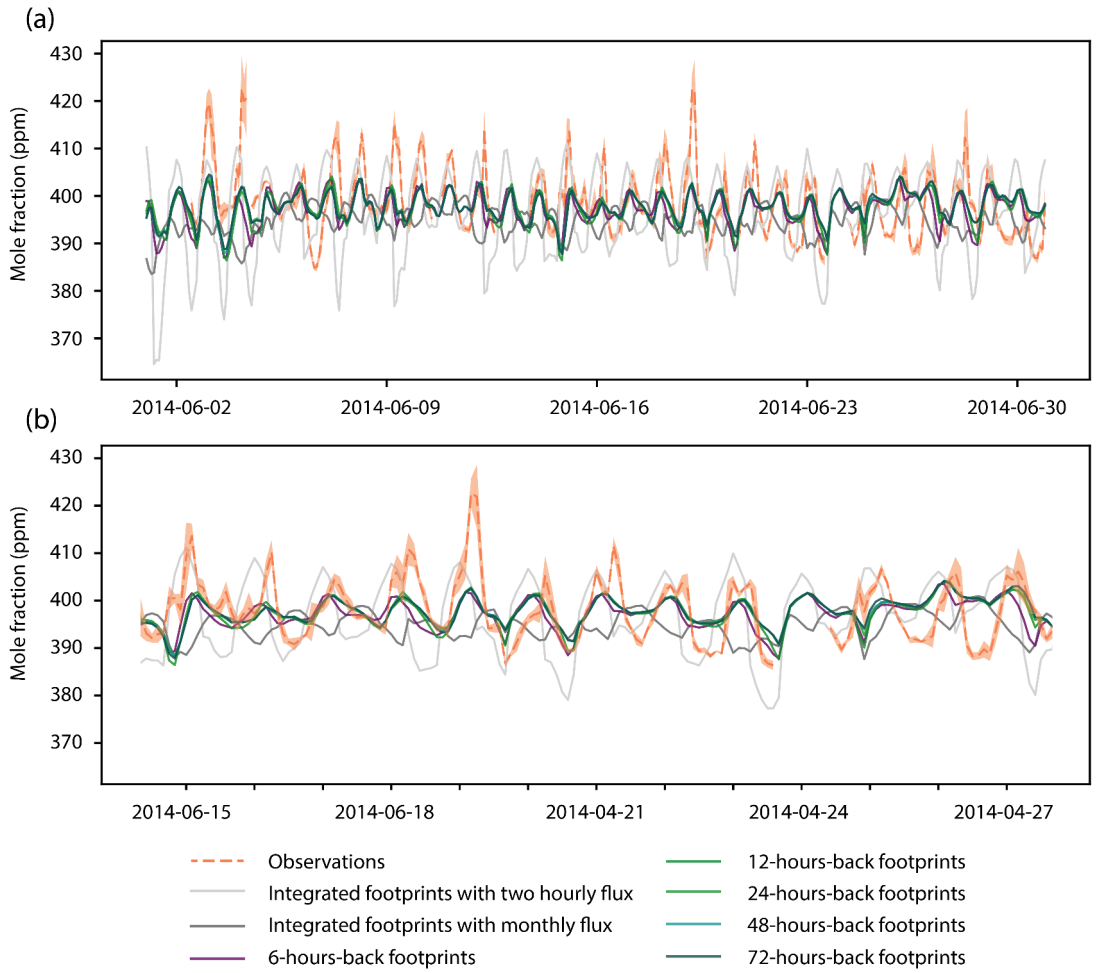

Fig. 2.11: (a) Observations at Ridge Hill in June 2014 (orange) and corresponding forward modelled mole fractions under different scenarios (greys, blues, greens). Shading on observations represents the standard deviation of sub-minutely measurements taken in each 2 hour period. (b) Zoomed in version of (a).

Table 2.4: Posterior UK CO_2 fluxes for June 2014 for "Test 1" that examines the impact of using footprints disaggregated in different ways.

Test	UK CO_2 flux (Tg yr^{-1})
	June 2014
Prior	-776
"True"	-355
72-hours-back footprints	$-365\pm^{39}_{40}$
24-hours-back footprints	$-347\pm^{41}_{43}$
30-day integrated footprints	$-0.6\pm^{55}_{59}$

Table 2.5: Statistics of fit to the synthetic data for the three inversions carried out in "Test 1" that examines the impact of using footprints disaggregated in different ways. "Prior" signifies the fit of prior modelled mole fractions to the "true" mole fractions. "Posterior" signifies the fit of posterior modelled mole fractions to the "true" mole fractions

		72-hours-back footprints		24-hours-back footprints		30-day integrated footprints	
		Prior	Posterior	Prior	Posterior	Prior	Posterior
MHD	R^2	0.35	0.45	0.31	0.7	0.27	0.48
	RMSE	1.67	1.45	2.72	1.53	3.91	1.93
	Bias	1.05	-0.19	1.42	0.03	2.8	0.87
RGL	R^2	0.56	0.77	0.54	0.64	0.14	0.25
	RMSE	3.75	0.98	3.89	1.2	5.34	1.79
	Bias	3.4	0.46	3.61	0.52	4.76	-0.77
HFD	R^2	0.41	0.66	0.38	0.64	0.11	0.22
	RMSE	2.42	1.54	2.62	1.56	4.07	2.22
	Bias	1.64	-0.4	1.91	-0.17	3.25	-0.05
TAC	R^2	0.4	0.71	0.37	0.7	0.27	0.48
	RMSE	2.71	1.51	2.72	1.53	3.91	1.93
	Bias	1.61	-0.27	1.79	-0.03	2.99	0.09
TTA	R^2	0.66	0.94	0.71	0.92	0.49	0.8
	RMSE	3.73	1.21	4.11	1.37	4.75	1.21
	Bias	3.1	1.01	3.6	1.15	3.88	-0.18
BSD	R^2	0.37	0.64	0.37	0.68	0.27	0.37
	RMSE	3.65	1.9	3.65	1.79	4.8	2.55
	Bias	2.15	-0.59	2.38	-0.39	3.38	-0.94
All sites	R^2	0.44	0.67	0.43	0.65	0.28	0.41
	RMSE	3.07	1.47	3.22	1.52	4.41	1.97
	Bias	2.12	-0.04	2.4	0.14	3.48	-0.18

2.3.3 Test 2: Gross vs. net flux scaling

This test compares an inversion that scales prior NEE (net flux) to an inversion that scales GPP and TER separately (gross fluxes).

The way the inversion is set up means that the uncertainty on prior fluxes is calculated as a percentage of the flux itself, therefore the uncertainty becomes zero when the flux is zero. For GPP and TER this does not pose a problem because the fluxes are never both zero. However for NEE this does become a problem as the flux switches between positive and negative twice a day, meaning that at times of zero flux the inversion cannot move away from the prior mean flux because it has no probability distribution related to it. In an attempt to reduce the impact of this, the scaling factor used to calculate the uncertainty on NEE scales with the flux, becoming larger if the flux is smaller, to resemble the posterior uncertainty of the gross flux inversion on an annual scale. The PDF of prior fluxes in the net flux inversion was assumed to be Gaussian as opposed to lognormal as a change of sign is physically possible in this case.

Whilst posterior monthly fluxes from the net flux inversion have changed significantly from the prior (Fig. 2.12a), they are not in agreement with the "true" flux except in July 2013 and August and September 2014. Annual flux estimates (Fig. 2.12c) also do not agree with the "true" flux, predicting a sink of nearly twice the "true" flux. The diurnal range of the net flux inversion (Fig. 2.12b) has a similar pattern of maximum daily net uptake as the gross flux inversion, however it does not estimate the maximum daily net source fluxes in spring (March, April, May) and June to be large enough. Figure 2.10c shows the "true" flux map minus the posterior flux map for the net flux inversion. Compared to the gross flux inversion in Fig. 2.10b, it is difficult to say which of these maps is closer to the "true" fluxes. The net flux inversion has not scaled up the prior fluxes enough in Scotland, Wales, central England, Northern Ireland and southern Republic of Ireland. Where the gross flux inversion overcompensated by scaling up the fluxes too much in England, the net flux inversion gives an improved flux estimate in these areas as the residual is close to zero here.

An analysis of the mean diurnal cycle in June 2014 (Fig. 2.13) reveals how the diurnal cycle is being scaled from the prior to better agree with the "true" flux. It is important to remember here that the timing of the diurnal cycle is not able to change as scaling factors can only go down to a minimum daily resolution. Figure 2.13 highlights the differences in diurnal cycle between the two models, in particular where the "true" TER flux shows very little diurnal variability (with an amplitude of 163 Tg CO_2 yr^{-1}) whereas the prior TER flux has a strong diurnal cycle (with an amplitude of 957 Tg CO_2 yr^{-1}). In the gross flux inversion the two competing TER and GPP fluxes can be adjusted leading to higher night-time fluxes that are closer to the "true" flux than the prior and a net monthly flux that agrees with the "true" flux. On the other hand, the net flux inversion can only stretch or shrink the diurnal cycle in one direction, increasing both the daytime sink and night-time source, or decreasing them. In this case it has shrunk, which does bring the mean posterior June 2014 flux closer to the

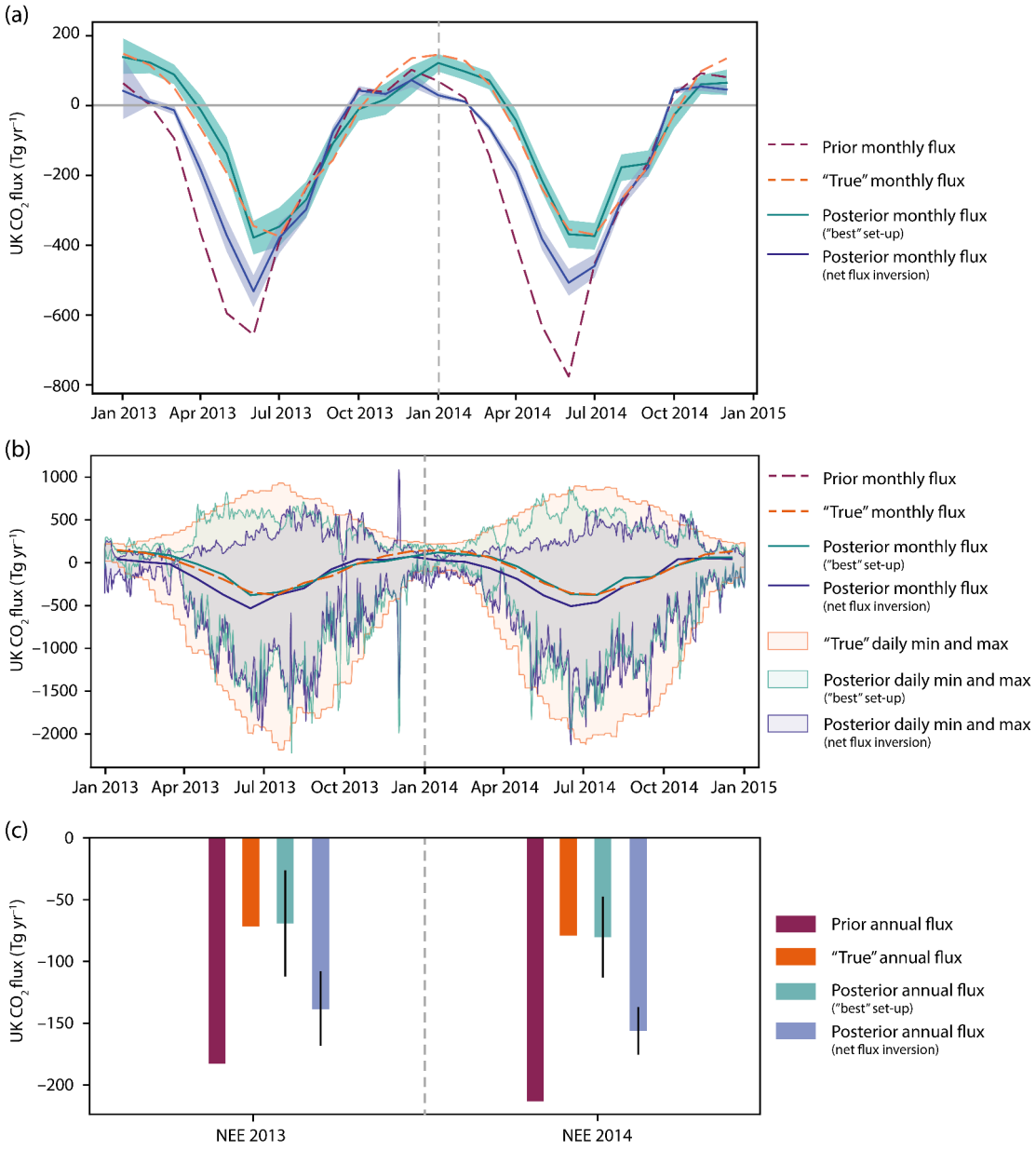

Fig. 2.12: Results of "Test 2" demonstrating the difference between scaling gross fluxes and scaling net fluxes. (a): Monthly average biospheric UK CO_2 fluxes. Shading represents the 5th–95th percentile. (b): Diurnal range of biospheric UK CO_2 fluxes, overlain by the monthly mean fluxes in (a). (c): Annual average biospheric UK CO_2 fluxes; error bars represent the 5th–95th percentile. "Best" set-up scales gross fluxes in the inversion.

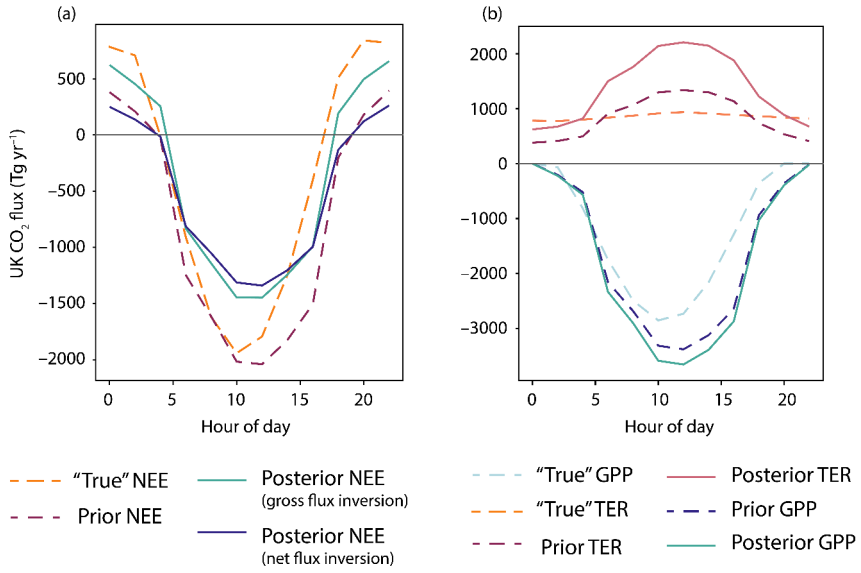

Fig. 2.13: (a): Prior, "true" and posterior average diurnal cycle of UK NEE CO_2 flux in June 2014 for "Test 2." (b): Prior, "true" and posterior average diurnal cycle of UK GPP and TER CO_2 flux in June 2014 for "Test 2."

mean "true" flux by 269 Tg CO_2 yr^{-1} but cannot go far enough to reconcile them as the posterior June 2014 sink is still 152 Tg CO_2 yr^{-1} too large compared to the "true" flux in this month.

This test demonstrates that it is very difficult for an inversion that can only scale NEE to account for disproportionate changes in the source and sink. Scaling the gross fluxes separately leads to a greatly improved result, at least in the system proposed here and likely in other inversion systems. In the real data inversions that follow in Chapters 3 and 4, a comparison of the performance of gross and net flux inversions is carried out to illustrate this point in a real data context.

2.3.4 Test 3: Disentangling different sources of CO_2

In this test, the impact of solving for the anthropogenic and ocean fluxes alongside the GPP and TER biospheric fluxes is explored. As explained in Section 2.1, the co-location of sources of CO_2 can make it difficult to resolve the separate sources. Therefore, many researchers will assume the anthropogenic source is known and fix it in the inversion. The ocean source is comparatively small so that is why it has been fixed in the other simulations presented in this work. Here, this decision to fix the anthropogenic and ocean sources is explained.

As per the synthetic test set-up, the synthetic data is generated using CARDAMOM biospheric fluxes and the prior fluxes are from JULES. The anthropogenic and oceanic component of the synthetic data and the prior anthropogenic and oceanic fluxes are the same. Therefore, this test investigates the inversion system's ability to retrieve the same anthropogenic fluxes when there are major differences in the biospheric fluxes (as the oceanic component is small, the focus will be on the anthropogenic

fluxes). The uncertainty of the prior fluxes is based on the same scaling (given in Table 2.3) for all sources.

Figure 2.14 shows the monthly fluxes from the inversion that includes the biospheric, anthropogenic and total flux sources. The posterior total flux agrees with the "true" flux in 18 out of 24 months within the 90 percentile confidence interval. However, separately, the posterior anthropogenic and biospheric fluxes do not agree with their respective "true" fluxes, the posterior anthropogenic flux agrees with the "true" anthropogenic flux in only 10 out of 24 months and the posterior biospheric flux agrees with the "true" biospheric flux in only 12 out of 24 months. Therefore this inversion system is not able to distinguish the anthropogenic fluxes from the biospheric fluxes when the anthropogenic fluxes are perfectly known, and cannot estimate anthropogenic fluxes with certainty over the UK. Increasing the number of unknowns in the inversion means that any differences will be attributed to the parameter that is easiest to change and in this case, changing a combination of the biospheric and anthropogenic fluxes has been the preferred pathway. Ultimately, even in the biospheric flux inversion, the scaling for GPP and TER is assumed to be correlated so the net flux is the result of most interest. However, as the uncertainty on anthropogenic fluxes is relatively small compared to the uncertainty on biospheric fluxes from process models, if the inversion is not able to resolve anthropogenic fluxes in even a simple case then there is a limit to the amount of information gained through solving for the different components of the total flux and it is more useful to focus on the biospheric fluxes.

Clearly in a real-data scenario, the anthropogenic fluxes are not perfectly known. This puts into question the validity of the assumption that anthropogenic fluxes can be modelled correctly before they are removed from observations, thereby leaving the remaining observations with only the biospheric influence (plus the baseline). As discussed in Section 2.1, Peylin et al. (2011) also challenges this assumption and comes to the conclusion that the uncertainties are non-negligible given the large discrepancies between different inventories. An investigation of the impact of a $\pm 10\%$ change in anthropogenic flux is carried out for the work in Chapter 3 (found in Sect. 3.3.2).

2.3.5 Test 4: Trans-dimensional basis functions in *space* vs. *time*

A trans-dimensional inversion in *space* removes the need to fix spatial regions to be scaled up and down and a trans-dimensional inversion in *time* means that scaling factors can apply to periods of less than one month, guided by the data, which may be particularly useful for CO_2 given its rapidly varying seasonal and diurnal cycle. Trans-dimensional inversions in *space* and *time* have been described in Sects. 1.4.8.1 and 2.2.4. There are positives of each approach. Here, these two methods for assigning basis-functions are compared in the context of a CO_2 inversion.

The trans-dimensional inversion in *time* follows the set-up explained in Sect. 2.2.4. The trans-dimensional inversion in *space* is set up in the following way. As the name suggests, instead of having a flexible time dimension, it is the space dimension that is flexible. This is achieved by splitting the sub-domain into an initial number of voronoi cells, or regions, created by drawing lines of equidistance

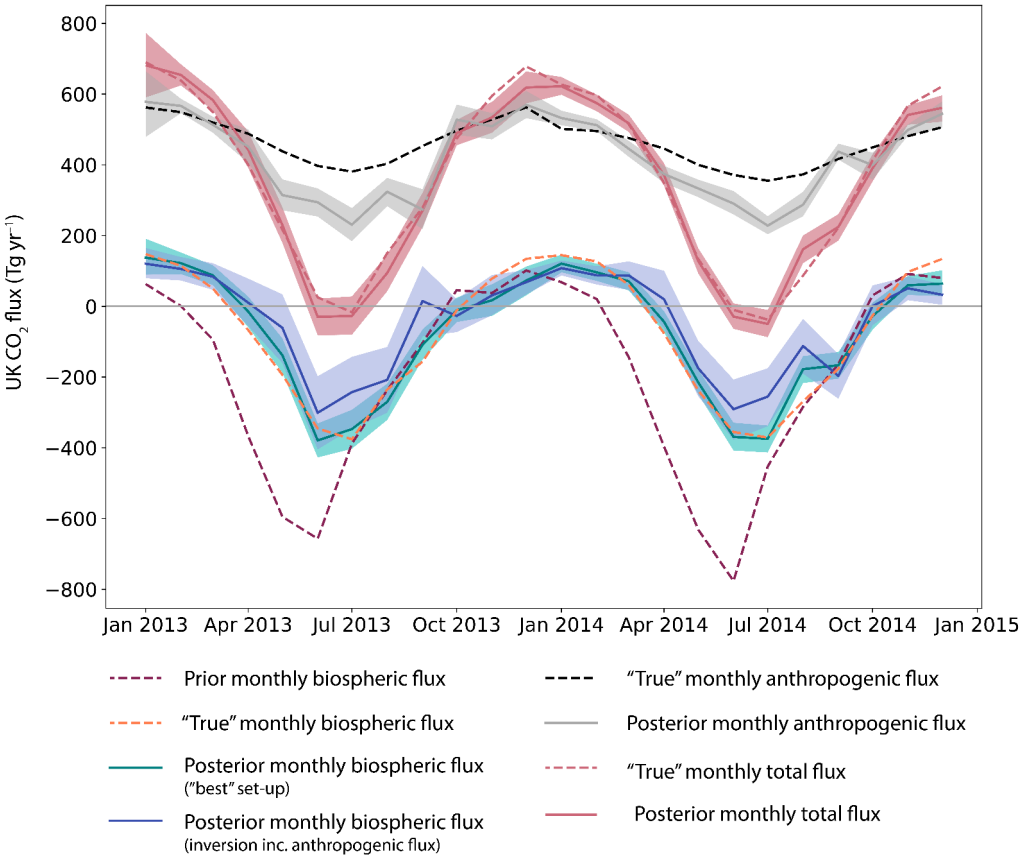

Fig. 2.14: Monthly average UK CO_2 fluxes for "Test 3" that looks at the difficulties of separating anthropogenic and biospheric fluxes.

between a number of randomly scattered points. As the MCMC algorithm progresses, the number of points used to create the voronoi cells can increase or decrease, or a point can move, changing the configuration of the cells. A scaling factor is found for each region in each configuration so that at the end of the iterations the effective spatial resolution of the inversion is higher than the resolution at each single iteration. However, the trans-dimensional inversion in space can only realistically solve for one source on the trans-dimensional grid as the large number of unknowns outweighs the data available. Due to the fact that the different sources of CO_2 need to be solved separately in the inversion (see Sect. 2.3.3), they are assumed to be fixed maps and a "residual" term is found on the trans-dimensional grid. The fixed source maps can be scaled up or down as one region and the "residual" is then able to vary spatially to account for any spatial differences between the prior maps and what is "seen" by the data. The prior uncertainty and hyper-parameters for GPP and TER are the same in both inversions. The prior uncertainty and hyper-parameters for the additional "residual" component were set so that the monthly and annual uncertainty on the net flux is roughly similar between the two inversions.

An illustration of the optimal number of spatial/temporal regions used in each of the inversions is shown in Fig. 2.15. For the temporal trans-dimensional inversion, in most months and for most spatial regions, a mean taken from the total number of temporal regions at each iteration of the MCMC algorithm (Fig. 2.15a) suggests that less than 5 scaling factors have been used to change the prior flux to better agree with the data (i.e. the month has been split into less than 5 time periods). The mean maximum number of temporal regions across all iterations (Fig. 2.15b) is around 15. The boundary conditions and the C3 grass PFT have the lowest number of regions. For the spatial trans-dimensional inversion (Fig. 2.15c), the mean number of spatial regions used each month varies between around 10 and 110 and the maximum number of regions across all iterations can be over 300 in some months.

Figure 2.16 shows the inversion results using the two approaches. The trans-dimensional inversion in *space* is not able to recreate the "true" monthly fluxes in spring and summer (Fig. 2.16a) and it is also not able to correctly estimate the annual net flux (Fig. 2.16c), predicting the net annual sink to be a factor of 1.8 too large. An investigation of the diurnal range reveals that the daily maximum in spring and summer is not large enough (Fig. 2.16b). From the flux maps in Fig. 2.17, posterior fluxes in the south of England, Wales and Republic of Ireland have been reduced to better agree with the "true" fluxes but in Northern Ireland and Scotland the posterior fluxes are not a great improvement on the prior.

Therefore, the trans-dimensional inversion in *time* is a clear improvement on that in *space*. It may be that having flexibility in the time dimension across all 23 basis functions gives a greater flexibility in the inversion overall than having flexibility in the spatial distribution of a "residual" term. Alternatively, it may be that the CO_2 inversion needs that flexibility in time to allow for the steep changes in baseline that occur in summer months (Fig. 2.2) and this is where the trans-dimensional inversion in *space* is failing. Either way, the trans-dimensional inversion in *time* is deemed the most appropriate for estimating fluxes of CO_2.

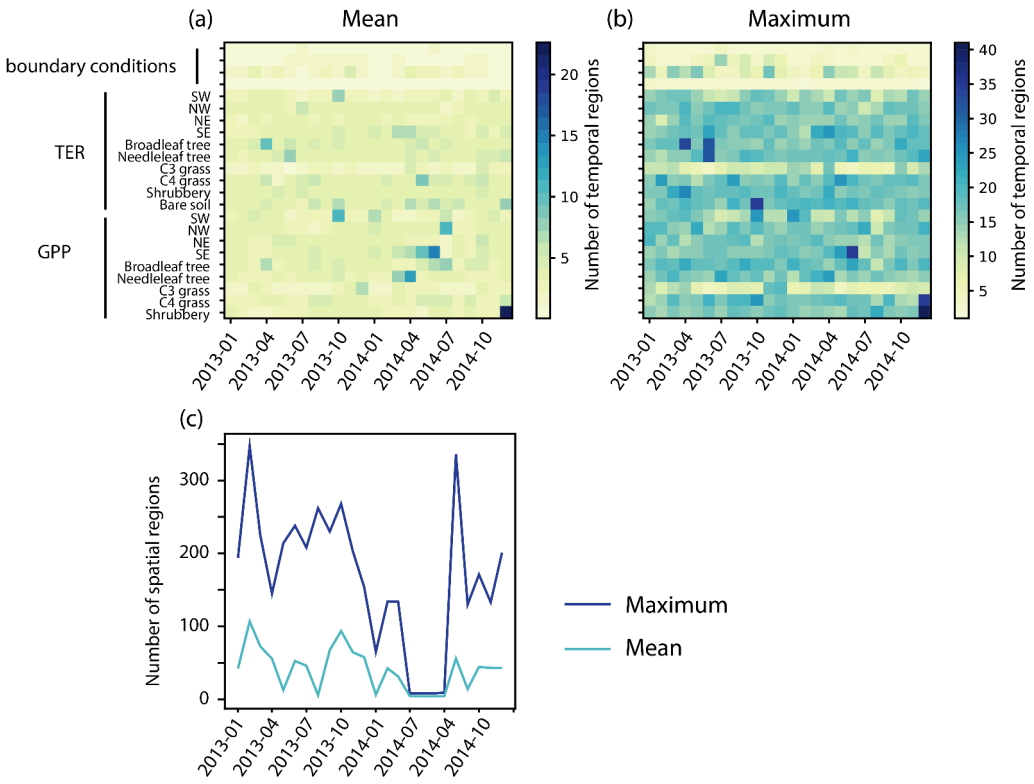

Fig. 2.15: Illustration of the mean (a) and maximum (b) number of *time* regions used in the trans-dimensional inversion in time across the 200,000 algorithm iterations. (c): Mean and maximum number of *space* regions used in the trans-dimensional inversion in space across the 200,000 algorithm iterations.

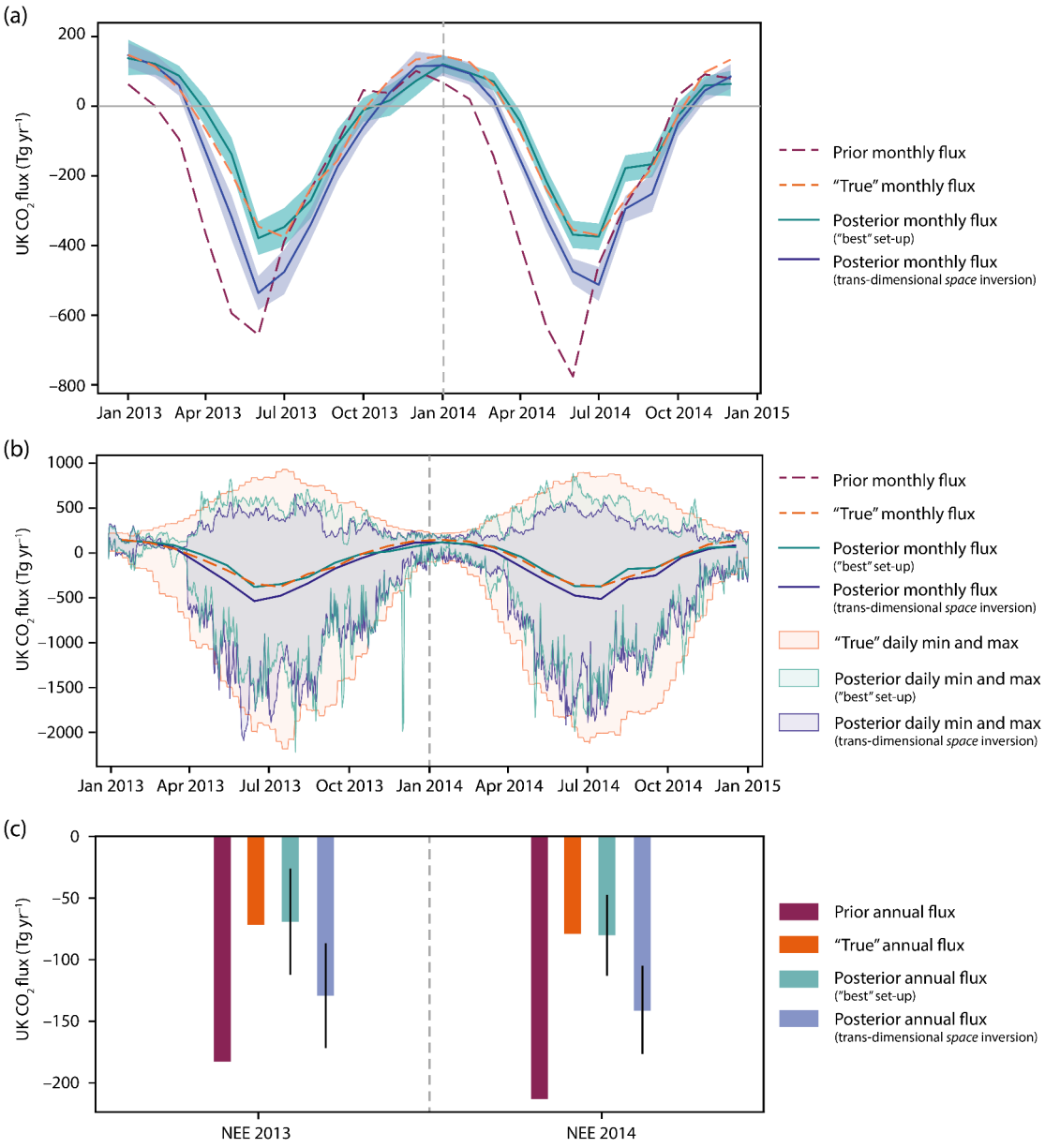

Fig. 2.16: Results of "Test 4" demonstrating the difference between trans-dimensional inversions in space and time. (a): Monthly average biospheric UK CO_2 fluxes. Shading represents the 5th–95th percentile. (c): Diurnal range of biospheric UK CO_2 fluxes, overlain by the monthly mean fluxes in (a). (c): Annual average biospheric UK CO_2 fluxes; error bars represent the 5th–95th percentile. "Best" set-up uses the trans-dimensional basis functions in *time*.

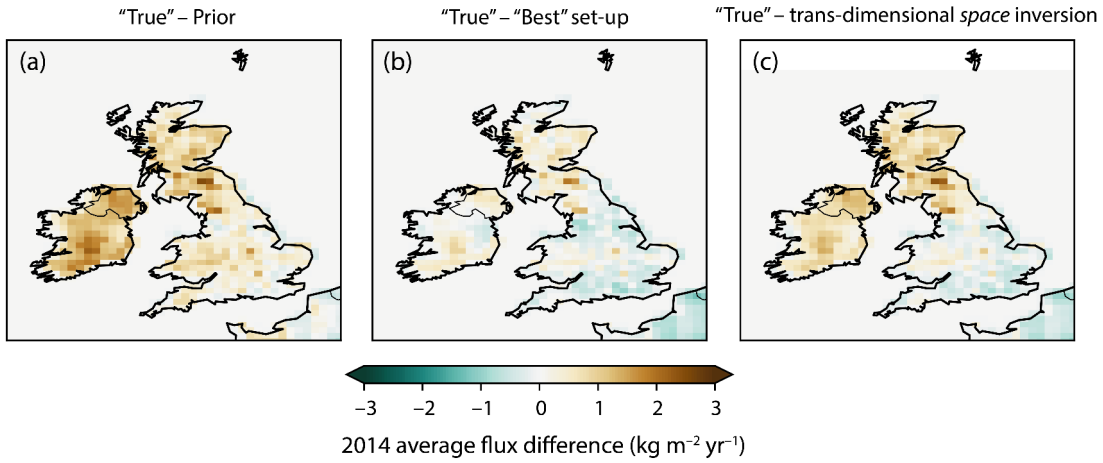

Fig. 2.17: (a): Difference between prior average 2014 flux map and "true" average 2014 flux map. (b): Difference between posterior average 2014 flux map from the "Test 0" standard inversion and "true" average 2014 flux map. (c): Difference between posterior average 2014 flux map from the trans-dimensional inversion in space and "true" average 2014 flux map.

2.3.6 Test 5: Implications of data selection

In this test the impact of the choice of data filter on the inversion is explored. The "local-lapse" filter is described in Section 2.2.2.3 and is designed to remove data collected during times when there is likely to be a high proportion of influence from local fluxes on the measurement regardless of the time of day. This filter is compared to using only daytime data, using daytime data that has also been filtered using the "local-lapse" filter and applying no filter at all. Here "daytime" includes the hours between 10 a.m. and 6 p.m. Of course, the synthetic data is created using the same LPDM as the sensitivity matrix so this test is not able to reveal the times where the model cannot replicate real atmospheric conditions (in this synthetic world, the NAME model *is* the real state of the atmosphere). However, given the different underlying biospheric fluxes, it may be able to reveal the times where the atmospheric transport cannot resolve the spatial structure of the "true" flux.

Figure 2.18 shows the results of all four inversions. The inversion using all data points does not replicate the "true" flux in summer months (Fig. 2.18a) and does not agree with the annual "true" flux (Fig. 2.18b), predicting an annual sink 20% the size of the "true" sink in 2013 and 50% the size of the "true" sink in 2014. This is important because it means that, as hypothesised above, there are times where the atmospheric transport cannot resolve the spatial structure of the "true" flux (i.e. at times of low wind speeds when the measurement station is not sampling fluxes from a large spatial area) and that some filtering is necessary. Filtering the data to use just daytime values agrees with the "true" flux within the estimated 90 percentile range in 16 out of 24 months (Fig. 2.18a) and agrees with the annual "true" flux (Fig. 2.18b). This is an improvement to using no filter at all and in December of both years the results of this inversion agrees better with the "true" flux than the "local-lapse" filter. Finally, filtering the data to use just daytime values along with filtering out times of supposed stagnant

Table 2.6: RMSE for "true" monthly average UK biospheric CO_2 flux and the inversions from "Test 5" using the "local-lapse" filter, daytime data or a combination of the two.

	"local-lapse" filter	daytime filter	daytime and "local-lapse" filter
RMSE	40	42	41

conditions provides a similarly good fit to the "true" monthly fluxes, also agreeing in 16 out of 24 months (Fig. 2.18a), agrees with the annual "true" flux (Fig. 2.18b) and, like the simple daytime filter, improves the fit to the "true" flux in December compared to the inversion using "local-lapse" filtered data.

The two daytime tests are very similar to using the "local-lapse" filter on all data points. Given the "local-lapse" filtered dataset shown in Fig. 2.6, it is not very surprising as this filter does generally retain many more daytime than night-time points. Comparing the RMSE of the monthly inversion results to the "true" monthly fluxes (Table 2.6) reveals that they all have an RMSE of around 40 Tg CO_2 yr^{-1} but that the "local-lapse" filter has the lowest RMSE and the simple daytime filter has the highest RMSE. Therefore, the "local-lapse" filter is a good choice and it is thought that the possibility to include some night-time data that is collected during favourable atmospheric conditions will be beneficial to the inversion to avoid biasing the results to daytime observations when photosynthesis is the predominant biospheric process.

2.4 Conclusions and future work

This chapter has outlined some of the challenges that are unique to atmospheric inversions of CO_2. The inverse set-up described in Chapter 1 has thus far been used to estimate fluxes of GHGs that do not have many co-located sources, do not have a diurnal and seasonal cycle and cannot be negative. Therefore, this chapter has set out the first concerted effort to adapt the hierarchical Bayesian trans-dimensional MCMC inversion to deal with the challenges of estimating fluxes of CO_2.

The multiple sources of CO_2 make it difficult to differentiate biospheric and anthropogenic fluxes. Like many other inverse studies of CO_2 fluxes, the decision has been made to focus on estimating biospheric fluxes, at least in this first attempt at developing a functional CO_2 inversion. Indeed, the results of one synthetic test indicate that there is not sufficient information in this set-up to separate biospheric and anthropogenic fluxes. Further work in this area could incorporate some of the techniques used to identify different source signatures and this could help to move this method towards solving for anthropogenic fluxes as well.

The strong diurnal variations in CO_2 mole fractions has required an adaptation to the NAME footprints that have traditionally been used in inverse studies. 30-day footprints have been partially disaggregated to result in a realistic forward modelled diurnal cycle. Tests have revealed that observed CO_2 concentrations are most sensitive to surface fluxes during the first 24 hours before a measurement

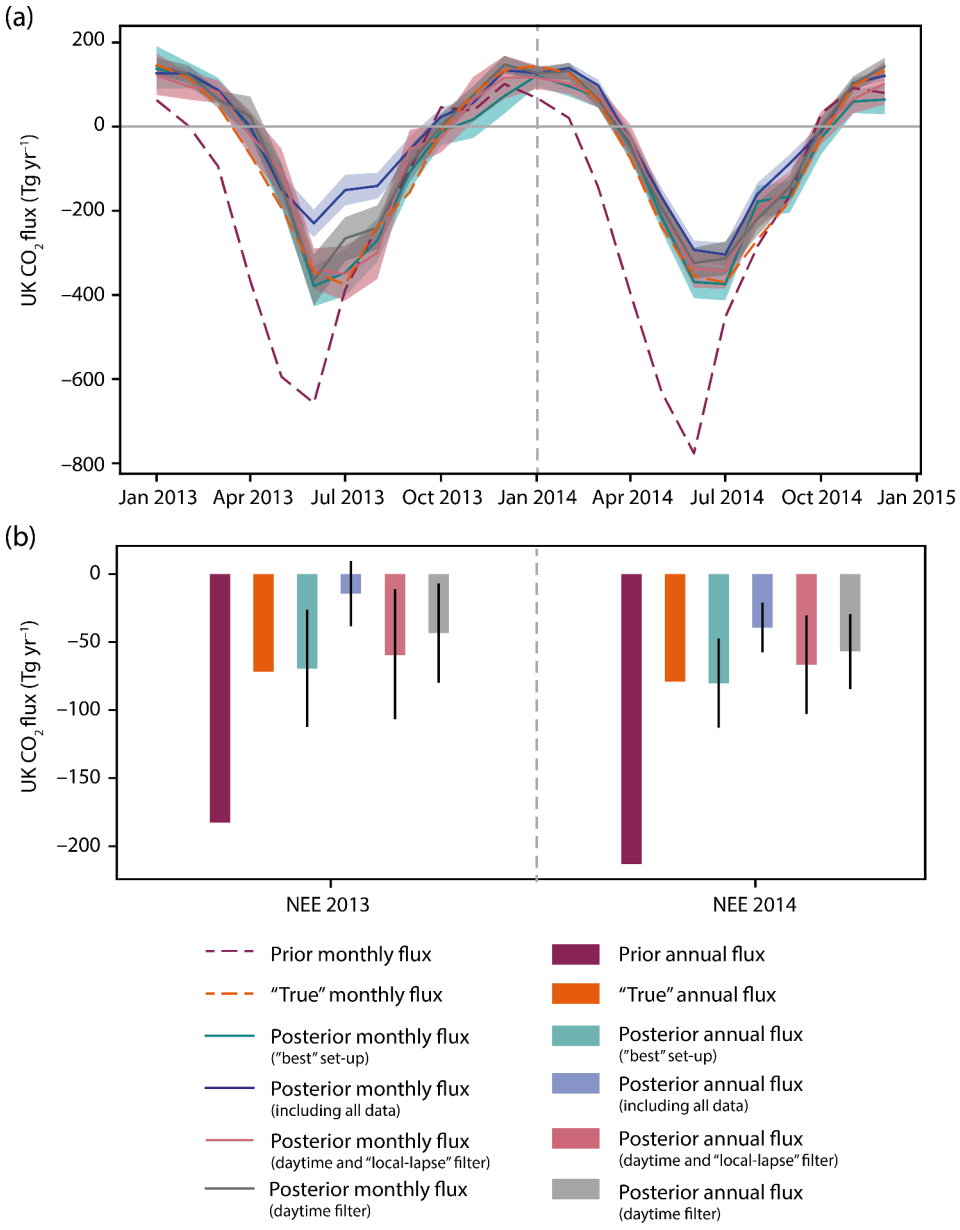

Fig. 2.18: Results of "Test 5" demonstrating the impact of using different data filters. (a): Monthly average biospheric UK CO_2 fluxes. Shading represents the 5th–95th percentile. (b): Annual average biospheric UK CO_2 fluxes; error bars represent the 5th–95th percentile. "Best" set-up uses the "local-lapse" filter.

is taken. Therefore, footprints have been disaggregated for the first 24 hours back in time and integrated footprints are used for the remainder of the time period. However, since this study has focussed on only one month, further work could test that 24 hours is sufficient by extending the study period to a full year.

Separately solving for fluxes of GPP and TER in the inversion enables a degree of flexibility that is not present in an inversion that scales only NEE. This flexibility proves to be very important for allowing the inversion to account for disproportionate changes in sources and sinks and greatly improves the inversion result. This is further explored in a real data scenario in Chapter 3 and with a different biospheric prior in Chapter 4.

Certain aspects of the inverse set-up have been tested for their appropriateness. It has been concluded that using the trans-dimensional functionality of the inversion in *time* rather than *space* benefits the CO_2 inversion due to the added temporal flexibility. The "local-lapse" filter, used to identify data points where NAME is expected to perform well, has been compared to other methods of data-filtering. Since the "local-lapse" filter mostly retains only daytime data points, the results are very similar to those using explicit daytime filters. However, the ability to retain some night time information is deemed useful for the inversion. In contrast, an inversion that included all data points did not perform well and shows that simulations are more sensitive to model errors (in the underlying flux map, for instance) under conditions when there is little mixing.

Chapter 3

Quantifying the UK's carbon dioxide flux

3.1 Introduction

This chapter takes the method set out in Chapter 2 and applies it to a real data scenario to estimate biospheric CO_2 fluxes in the UK. GPP and TER estimates from JULES and CARDAMOM are used as prior flux constraints in two separate inversions. The results and discussion of this chapter feature in White et al. (2019).

The UK government has set legally binding targets to curb GHG emissions in an attempt to prevent dangerous levels of climate change. The Climate Change Act 2008 (The UK government, 2008) commits the UK to 80% cuts in GHG emissions, from 1990 levels, by 2050. To support this legislation, a continuous and automated measurement network has been established (Stanley et al., 2018; Stavert et al., 2018) with the goal of providing estimates of GHG emissions that are independent of the UK's bottom-up anthropogenic inventory that must be reported annually to the UK Parliament and submitted to the UNFCCC. Previous studies have used data from the UK-DECC network to infer emissions of CH_4, N_2O and HFC-134a from the UK (Ganesan et al., 2015; Manning et al., 2011; Say et al., 2016). Here, the UK-DECC network and two additional sites from the GAUGE programme (Palmer et al., 2018) are used to estimate biospheric fluxes of CO_2. Whilst anthropogenic emissions, which are the remit of the UK inventory, are not estimated in this study, it represents the first step towards a framework for estimating the complete UK CO_2 budget.

The carbon cycle is subject to a lot of variability from short and long term changes in temperature, precipitation, nutrient availability and increased atmospheric CO_2 concentrations. The majority of this variability, whilst observed in the atmosphere, originates from the processes ocurring in the biosphere (Schimel et al., 2015) making it the most complex of the carbon reservoirs and consequently there are large gaps in understanding of biospheric carbon cycle dynamics. Models that represent the biosphere, frequently used as prior biospheric fluxes in atmospheric CO_2 inversions, vary significantly in internal dynamics leading to large discrepancies in estimated fluxes and, as a result, biospheric CO_2 fluxes are the most uncertain component of the global carbon budget. These models could be

land surface models (LSMs), dynamic global vegetation models (DGVMs, often used in conjunction with LSMs), or data assimilation frameworks. Jones et al. (2013) finds that the differences between the LSMs used in the Climate Model Intercomparison Project Phase 5 (CMIP5) are as large as the differences between the representative concentration pathways (RCPs) that are used in climate models to represent possible future anthropogenic emissions under different scenarios. These differences may be attributed to the differing ability of the models to represent soil carbon (Todd-Brown et al., 2013) or the difficulties in simulating leaf (autotrophic) respiration (Atkin et al., 2015), for example.

The large variations between models of biospheric fluxes have led to the use of two different biospheric flux priors in this study. This is to firstly assess the impact that the choice of biosphere model has on the inversion. As the inverse framework is sensitive to the diurnal variations of prior fluxes, and as these diurnal variations are large in biospheric fluxes with fundamental differences between models, there is potential for the choice of prior to have an important impact on the posterior flux result, even with large prior uncertainty. Secondly, through updating the biospheric flux priors in the inversion, the performance of the models that produce the prior biospheric fluxes can be evaluated against the constraint of the atmospheric data.

The potential for atmospheric inversions to evaluate the spatiotemporal patterns of biospheric fluxes from models has been explored in Fang et al. (2014). The study recognised the work done so far to compare inverse flux estimates with those from biosphere models and inventories (e.g. Hayes et al., 2012; McGuire et al., 2012) and the continued development of regional inverse systems towards a resolution at which the processes controlling flux variability in biosphere models may be able to be resolved, i.e. from monthly fluxes at regional scales (10^5-10^6 km^2) down to hourly fluxes at the grid scale of biosphere models (10^2-10^3 km^2) (e.g. Gourdji et al., 2010, 2012). Using a regression framework based on a geostatistical inverse modelling approach, Fang et al. (2014) was able to evaluate flux patterns at fine scales (3 hourly fluxes at $1^\circ \times 1^\circ$ resolution) as opposed to the aggregated scales that are used in most inversion studies. The biosphere models compared performed best in temperate broadleaf and mixed forests biomes. They were best able to represent fluxes during the growing season (May - September) and struggled during the transition seasons. The work of Fang et al. (2014) highlights the possibilities for atmospheric inversions to provide a constraint on biosphere models and to understand where the underlying processes of biosphere models may be failing. Consequently, this is something that will be explored in the work of this chapter.

3.2 Method

Much of the method used in the work of this chapter, including the inverse set-up and hyper-parameters, has been described in Chapter 2. Further details on the measurement data and prior biospheric fluxes are given here.

3.2.1 Data

The CO_2 mole fraction data used in this chapter has been introduced in Chapter 2 along with the details of each measurement site (Table 2.1). For the purposes of the inverse modelling carried out in this study, continuous CRDS data are averaged to a 2-hour time resolution. The measurement uncertainty was assumed to be equal to the standard deviation (SD) of the measurements over the 2-hour period to give an estimate of measurement repeatability and a measure of the sub-model-timescale variability in the observations. The 2-hourly measurement uncertainty was then averaged over the month to ensure that measurements of high concentrations were not de-weighted, as they are more likely to have greater variability and therefore a larger SD.

3.2.2 Prior biospheric fluxes

Two models (CARDAMOM and JULES) were used to assess how much influence the choice of biospheric prior has on the outcome of the inversion. The NAME model was used to simulate the contribution of anthropogenic and oceanic fluxes to the data, and this contribution was removed from the observations prior to the inversion. These fixed fluxes in the inversion have been described in Chapter 2. The spatial and temporal resolution of the prior information and fixed fluxes is summarised in Table 2.2.

Given the results of "Test 2" in Chapter 2, separating GPP and TER in the inversion appears to be an important improvement on scaling NEE directly and it is what has been implemented here. However, in order to assess this conclusion in a real data scenario, two further inversions have been carried out for JULES and CARDAMOM where only NEE is scaled.

3.2.2.1 CARDAMOM

The CARbon DAta MOdel fraMework (CARDAMOM) uses a model-data fusion approach to retrieve location specific ensembles of parameters for the DALEC model (Bloom et al., 2016). CARDAMOM uses a Bayesian approach within a Metropolis-Hastings MCMC algorithm to compare model states and flux estimates against observational information to determine the likelihood of potential parameter sets guiding the parameterisation processes. DALEC simulates the ecosystem carbon balance including uptake of CO_2 via photosynthesis, CO_2 loss via respiration, mortality and decomposition processes, including carbon flows between ecosystem pools (non-structural carbohydrates, foliage, fine roots, wood, fine litter, coarse woody debris and soil organic matter). GPP, or photosynthesis, is estimated using the aggregated canopy model (ACM; Williams et al. (1997)) while autotrophic respiration is estimated as a fixed fraction of GPP. Mortality and decomposition processes follow first order kinetic equations (i.e. a daily fractional loss of the C stock in question). The mortality and decomposition parameters are modified based on an exponential temperature sensitivity parameter. The current version of DALEC does not include a representation of the water cycle, rather water stress is parameterised through a sensitivity to high vapour pressure deficit. Comprehensive descriptions of

CARDAMOM can be found in Bloom et al. (2016) and Bloom and Williams (2015) and DALEC in Smallman et al. (2017).

The CARDAMOM analysis to generate the carbon flux priors was conducted at a weekly time step and 25 km × 25 km spatial resolution. The weekly time step information was downscaled to 2-hourly intervals, assuming that each day repeated throughout each week. Downscaling of GPP fluxes was assumed to be distributed through the daylight period based on intensity of incoming shortwave radiation. Respiration fluxes were downscaled assuming exponential temperature sensitivity.

The observational information used in this analysis were satellite-based remotely sensed time series of Leaf Area Index (LAI) (MODIS; MOD15A2 LAI-8 day version 5, http://lpdacc.usgs.gov/) a prior estimate of above ground biomass (Thurner et al., 2014) and a prior estimate of soil organic matter (Hiederer and Köchy, 2012). Meteorological drivers were taken from ERA-Interim reanalysis. Ecosystem disturbance due to forest clearances were imposed using Global Forest Watch information (Hansen et al., 2013).

3.2.2.2 JULES

The Joint UK Land Environment Simulator (JULES) is a process driven Land Surface Model (LSM) that estimates the energy, water and carbon fluxes at the land-atmosphere boundary (Best et al., 2011; Clark et al., 2011). JULES version 4.6 was used in this work, driven with the WATCH Forcing Data methodology applied to Era-Interim reanalysis data (WFDEI) meteorology (Weedon et al., 2014) which were interpolated to 0.25° × 0.25° (Schellekens et al., 2017). The land cover was prescribed for 9 surface types and the vegetation phenology for 5 PFTs using MODIS monthly LAI climatology and fixed MODIS land cover and canopy height data (Berry et al., 2009). The soil thermal and hydrology physics are described using the JULES implementation of the Brooks and Corey formulation (Marthews et al., 2015) with the soil properties sourced from the Harmonised World Soil Database (FAO/IIASA/ISRIC/ISS-CAS/JRC, 2009). Soil carbon was calculated as the equilibrium balance between litter-fall and soil respiration for the period 1990-2000 using the formulation of Mariscal (2015). The full JULES configuration and science options are available for download from the Met Office science repository (https://code.metoffice.gov.uk/trac/roses-u/browser/a/x/0/9/1/trunk?rev=75249).

3.3 Results

The CO_2 inversion set-up developed in Chapter 2 is applied to UK biospheric CO_2 flux estimation using output from two different models of biospheric flux as a prior constraint in two inversions. Here, the differences between output from the two prior models are first described, followed by the UK flux estimates found in the inversions, along with the spatial distribution of posterior fluxes.

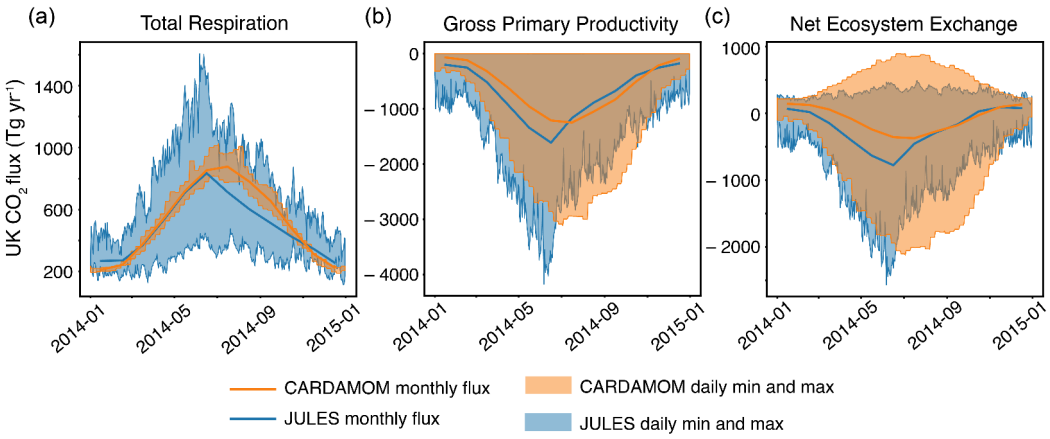

Fig. 3.1: Prior UK fluxes in 2014. (a-c) Comparison of JULES (blue) and CARDAMOM (orange) monthly mean fluxes and minimum and maximum daily values for TER, GPP and NEE respectively.

3.3.1 Comparison of prior biospheric flux estimates

The CO_2 fluxes from CARDAMOM and JULES differ both temporally and spatially. Figure 3.1 shows UK fluxes of GPP, TER and NEE from the two models. Most notable differences are seen in TER (Fig. 3.1a) where JULES has a large diurnal range whereas CARDAMOM has a small diurnal range. Averaged to monthly resolution, the fluxes are relatively similar although CARDAMOM has a higher TER flux from July to October. Diurnal ranges for GPP (Fig. 3.1b) are more similar in magnitude, however JULES exhibits a stronger sink in spring with maximum uptake in June. CARDAMOM has maximum uptake in July and exhibits a stronger sink in autumn. Combining these two fluxes leads to different NEE profiles for both models (Fig. 3.1c). The daily maximum source from JULES remains relatively constant throughout the year, whereas the daily maximum source in CARDAMOM follows a similar seasonal cycle to the daily maximum sink (albeit with a smaller magnitude). Monthly net fluxes are similar between both models for much of the year although JULES has stronger uptake between March and June.

In order to understand some of these seasonal differences it is useful to compare the processes taking place in each model. The CARDAMOM system explicitly simulates the soil and litter stocks, growth and turnover processes. LAI is retrieved from the DALEC model (which was calibrated using MODIS LAI estimates at the correct time and location of the analysis, explained in Sect. 3.2.2.1) and updated at each weekly time step. In the JULES system, soil and litter carbon stocks are fixed values for each grid cell, calibrated from 1990-2000, and a fixed climatology of LAI and canopy height is used. Therefore, variability in TER and GPP fluxes from JULES are governed by meteorology, primarily temperature but also significant signals from photosynthetically active radiation (PAR) and precipitation via the soil moisture. This gives CARDAMOM interannual variability in LAI and soil carbon stocks, whereas these parameters remain constant in JULES year to year. However, meteorology drives the JULES model at a 2-hourly timestep as opposed to a weekly time-step in

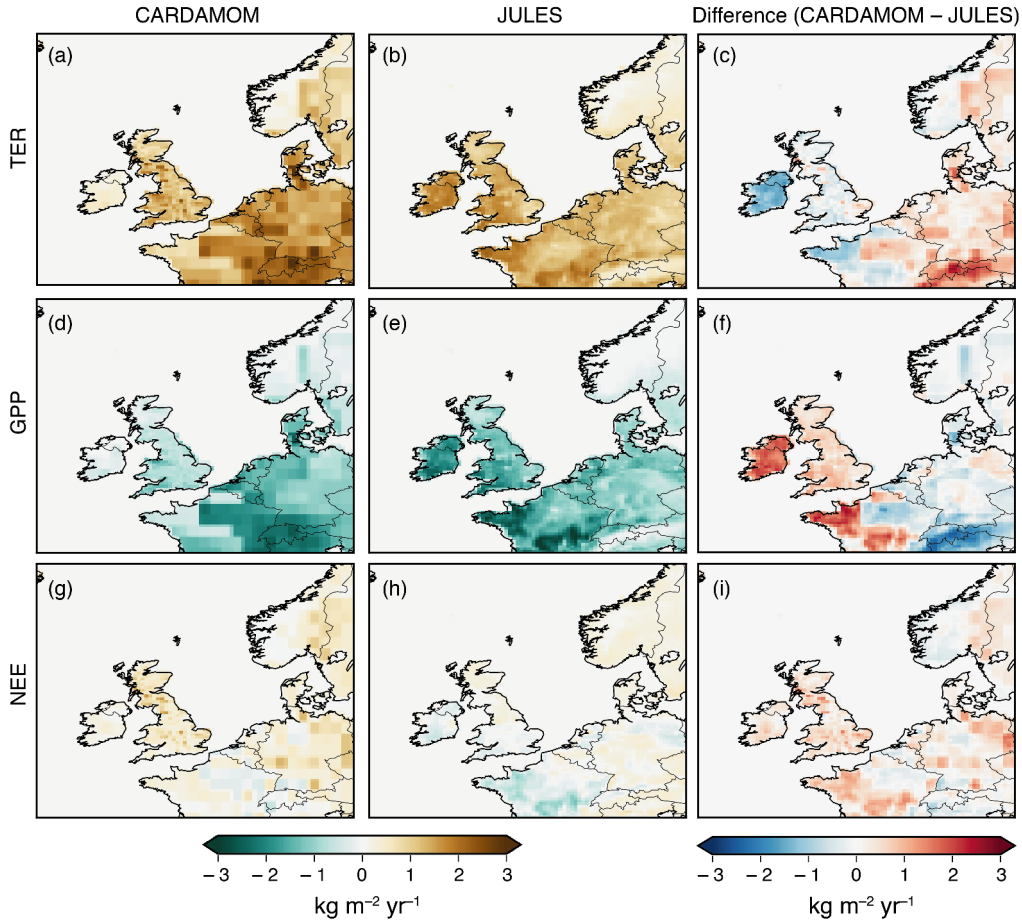

Fig. 3.2: Average prior flux maps for winter 2013 (December 2013, January – February 2014). (a) TER from CARDAMOM; (b) TER from JULES; (c) the difference between CARDAMOM and JULES TER; (d) GPP from CARDAMOM; (e) GPP from JULES; (f) the difference between CARDAMOM and JULES GPP; (g) NEE from CARDAMOM; (h) NEE from JULES; (i) the difference between CARDAMOM and JULES NEE.

CARDAMOM. Therefore, in the 2-hourly CARDAMOM product used here, the diurnal range is not explicitly simulated and is downscaled from a weekly resolution. This downscaling is done based on light and temperature curves as explained in Sect. 3.2.2.1. In CARDAMOM, the autotrophic respiration is a fixed fraction of the GPP, roughly ranging from 0.3 to 0.7. In JULES, the autotrophic respiration is made up of several PFT specific fixed fractions of GPP, totalling around 0.1 to 0.25, plus some terms related to nitrogen content. Therefore, there are some large differences between the model processes, particularly in how the respiration fluxes are simulated. This could be leading to too small a diurnal range in CARDAMOM TER and too large a diurnal range in JULES TER.

Figures 3.2 and 3.3 show spatial maps of GPP, TER and NEE from both models averaged over winter (December, January, February) and summer (June, July, August) months. The pattern of TER is similar for both models, however JULES always has a stronger source over Northern Ireland and CARDAMOM has a stronger source in east England. In winter there are only small spatial variations

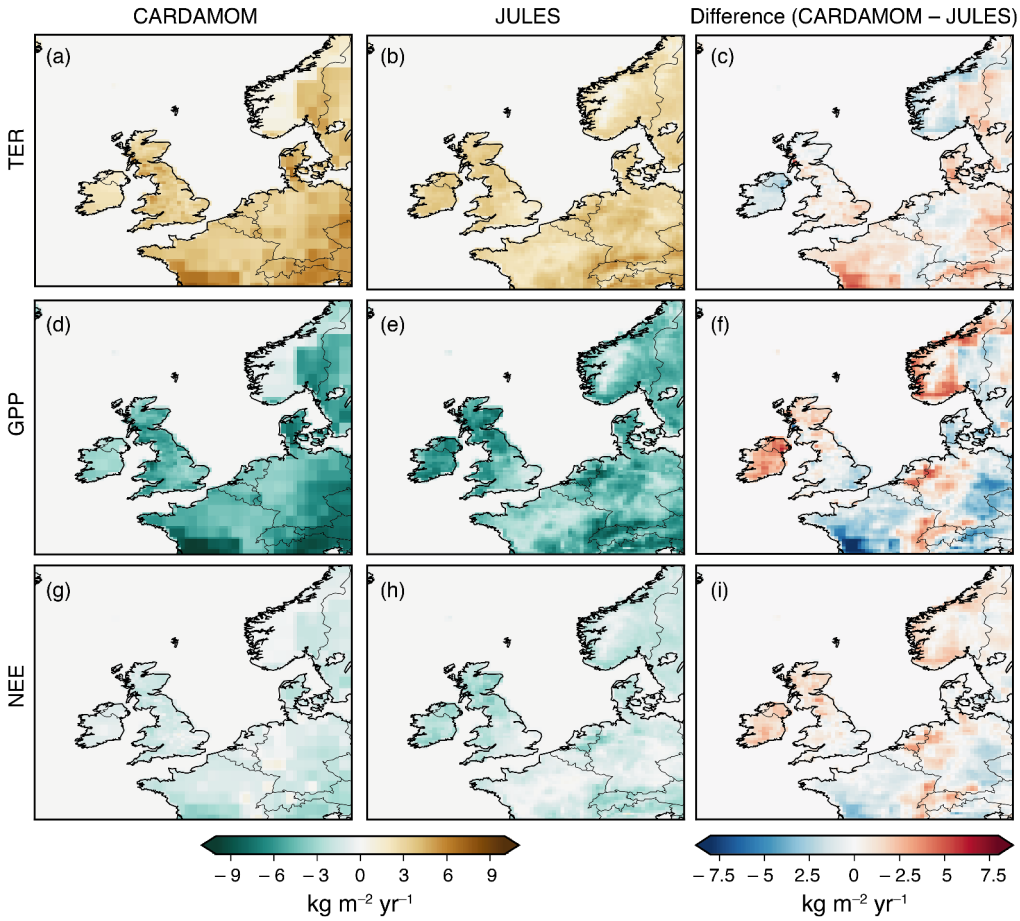

Fig. 3.3: Average prior flux maps for summer 2014 (June – August 2014). (a) TER from CARDAMOM; (b) TER from JULES; (c) the difference between CARDAMOM and JULES TER; (d) GPP from CARDAMOM; (e) GPP from JULES; (f) the difference between CARDAMOM and JULES GPP; (g) NEE from CARDAMOM; (h) NEE from JULES; (i) the difference between CARDAMOM and JULES NEE.

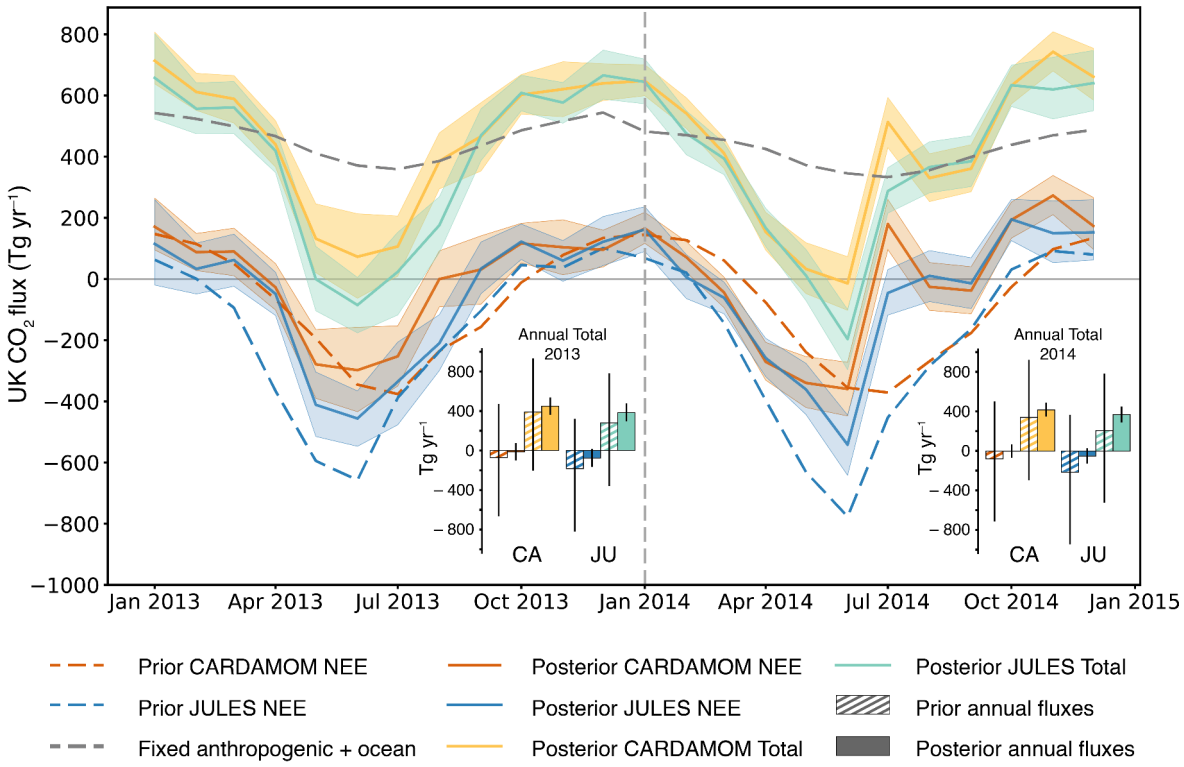

Fig. 3.4: Posterior monthly net UK CO_2 flux (emission to the atmosphere is a positive flux). Orange and blue monthly fluxes are posterior net biospheric (NEE) fluxes. Prior biosphere fluxes from JULES and CARDOMOM are shown in dashed orange and blue lines respectively. The fixed anthropogenic and ocean fluxes are denoted by the dark grey dashed line. Yellow and green monthly fluxes are the sum of the posterior NEE fluxes and the fixed anthropogenic and ocean fluxes. Shading represents 5th – 95th percentile. The bar charts represent annual net UK CO_2 flux for 2013 (left) and 2014 (right). Hashed bars denote prior annual fluxes, solid bars denote posterior annual fluxes. The bar colours correspond to the line colours: left hand bars for each model are NEE fluxes, right hand bars for each model are total fluxes (NEE + fixed sources). Uncertainty bars represent 5th – 95th percentile. CA – CARDAMOM. JU – JULES.

in CARDAMOM GPP fluxes, whereas JULES has its largest uptake in south-west England and Wales. In summer, the models are roughly in agreement in the size of the sink in Wales and the majority of England, however JULES has a stronger sink in Scotland and Northern Ireland and CARDAMOM has a stronger sink in central and south-east England. The differences between the models in GPP and TER lead to fairly different winter NEE flux maps. CARDAMOM is a net source everywhere in winter, with areas of strongest net source in southern Scotland, east and central England. JULES is a small net winter sink in Northern Ireland, Wales, and south and central England. Summer NEE fluxes are similar between the models, although JULES has a stronger net sink in Scotland and Northern Ireland.

Table 3.1: Posterior UK estimates for the maximum net biospheric source and sink for the inversions using CARDAMOM and JULES priors (values also shown in Fig. 3.4). The month in brackets indicates the month in which the maximum source/sink occurred.

	Year	Max. sink (Tg CO_2 yr^{-1})	Max. source (Tg CO_2 yr^{-1})
CARDAMOM	2013	$-298\pm^{140}_{136}$ (June)	$171\pm^{94}_{76}$ (January)
	2014	$-360\pm^{87}_{88}$ (June)	$273\pm^{65}_{63}$ (November)
JULES	2013	$-456\pm^{90}_{91}$ (June)	$122\pm^{83}_{78}$ (December)
	2014	$-542\pm^{97}_{100}$ (June)	$195\pm^{65}_{70}$ (October)

3.3.2 Posterior UK fluxes

The annual NEE estimates that have been derived for the UK using CO_2 flux output from the two different models of biospheric flux as prior information are $-13\pm^{90}_{87}$ Tg CO_2 yr^{-1} (CARDAMOM prior) and $-76\pm^{91}_{90}$ Tg CO_2 yr^{-1} (JULES prior) in 2013 and $-2\pm^{70}_{68}$ Tg CO_2 yr^{-1} (CARDAMOM) and $-51\pm^{80}_{78}$ Tg CO_2 yr^{-1} (JULES) in 2014 (Fig. 3.4 – orange and blue bars for CARDAMOM and JULES respectively). These annual net flux estimates from both models agree within the estimated uncertainties and mean values are higher than their respective priors in both cases. The uncertainties straddle the zero net flux line implying that the UK is roughly in balance between sources and sinks of biospheric CO_2. However, according to the inversion using JULES, a net biospheric source is less likely than in the inversion using CARDAMOM. When added to the anthropogenic and ocean fluxes that remained fixed during the inversion the following estimates are produced for annual total net CO_2 release from the UK (Fig. 3.4 – yellow and green bars for CARDAMOM and JULES respectively): $448\pm^{90}_{87}$ Tg CO_2 yr^{-1} (CARDAMOM prior) and $386\pm^{91}_{90}$ Tg CO_2 yr^{-1} (JULES prior) in 2013 and $418\pm^{70}_{68}$ Tg CO_2 yr^{-1} (CARDAMOM prior) and $369\pm^{80}_{78}$ Tg CO_2 yr^{-1} (JULES prior) in 2014.

Whilst it has been assumed that anthropogenic and ocean fluxes are perfectly known, in reality there are non-negligible uncertainties related to these fluxes (Peylin et al., 2011). When the anthropogenic source was varied by $\pm$ 10%, a conservatively large estimate of these uncertainties, posterior biospheric flux estimates using the CARDAMOM prior still suggest a balanced biosphere, and posterior flux estimates using the JULES prior suggest a small net sink at the lowest end of the possibilities explored here (see Fig. 3.5). All mean annual posterior estimates, regardless of the anthropogenic source used, suggest the prior net biospheric flux is underestimated, i.e. posterior biospheric uptake of CO_2 is smaller than predicted by the models. However, this is less statistically significant with the 2013 inversion using the CARDAMOM prior.

The monthly posterior UK estimates using both models (Fig. 3.4) mostly agree well with each other within the uncertainties. However, they are both notably different from the prior estimates,

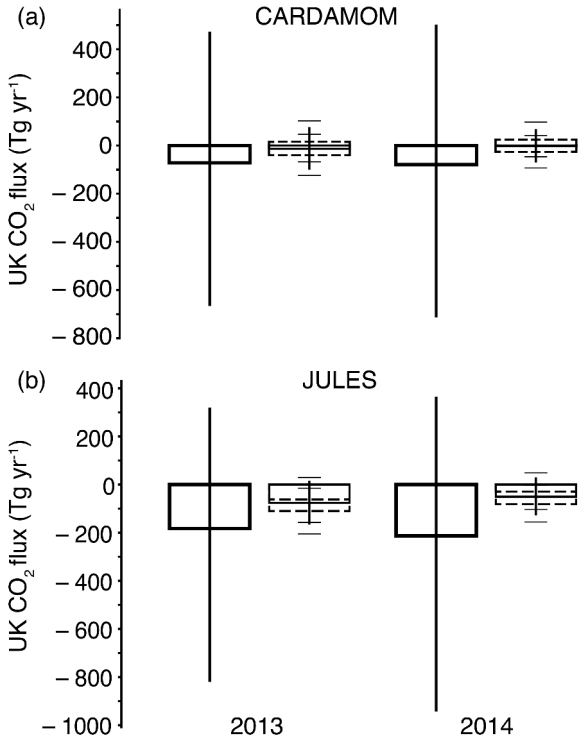

Fig. 3.5: Annual UK NEE flux estimates from CARDAMOM and JULES inversions for 2013 and 2014. Left bars are prior NEE estimates, right bars are posterior NEE estimates. Dashed bars on the posterior estimates represent annual NEE fluxes for inversions that use fixed anthropogenic fluxes multiplied by $\pm 10\%$. Uncertainty bars represent 5th – 95th percentile. Solid uncertainty bars on posterior estimates are the uncertainty on the inversions using normal anthropogenic fluxes. Whiskers on the posterior estimates are the uncertainty on the inversions using anthropogenic fluxes multiplied by $\pm 10\%$.

especially in 2014. The posterior total UK flux estimate, achieved by adding the posterior NEE fluxes to anthropogenic and coastal ocean fluxes, shows that, according to the CARDAMOM inversion, the UK may not be a net sink of CO_2 at any time of year in 2013 and 2014. However, the JULES inversion suggests the UK is a net sink of CO_2 in June of both years.

Posterior seasonal cycle amplitudes are generally smaller than the prior amplitudes, except in the CARDAMOM inversion in 2014. Table 3.1 gives the posterior maximum and minimum values of NEE, leading to seasonal cycle amplitudes of 469 Tg CO_2 yr^{-1} and 578 Tg CO_2 yr^{-1} for 2013 and 633 Tg CO_2 yr^{-1} and 737 Tg CO_2 yr^{-1} for 2014, for the CARDAMOM and JULES inversions respectively. These values are 90% and 76% of the prior amplitudes in 2013 and 123% and 85% of the prior amplitudes in 2014.

The largest differences between the prior and posterior are seen in spring and summer for both models. Posterior UK NEE estimates from the CARDAMOM inversion are in agreement with the prior for 11 months: during the first half of 2013, in the majority of winter months (December, January, February) and in June 2014. When the CARDAMOM inversion posterior UK NEE estimates are not in agreement with the prior, they are usually larger, with a maximum difference in 2013 of $235\pm^{92}_{91}$ Tg CO_2 yr^{-1} in August and a maximum difference in 2014 of $551\pm^{80}_{84}$ Tg CO_2 yr^{-1} in July, although in spring (March, April, May) 2014 they tend to be smaller than the prior, with a maximum difference of $-194\pm^{64}_{60}$ Tg CO_2 yr^{-1} in April. Posterior UK NEE from the JULES inversion agrees with the prior for nine months during the two-year period, the majority of which are between November and February. Otherwise, the posterior estimate from the JULES inversion is larger than the prior with a maximum difference in 2013 of $318\pm^{70}_{71}$ Tg CO_2 yr^{-1} in April and a maximum difference in 2014 of $407\pm^{76}_{72}$ Tg CO_2 yr^{-1} in July.

Looking at the spring and summer differences more closely, the JULES model has a lower net spring flux than the posterior, and the CARDAMOM model is either in agreement with or higher than the posterior estimate of the net spring flux. Generally the models are underestimating the net summer flux compared to the posterior flux (to the greatest extent in 2014) although the summer estimate from the JULES inversion in 2013 is not statistically different from the prior. The average spring difference between the posterior and the prior for the CARDAMOM inversion is $-2\pm^{89}_{88}$ Tg CO_2 yr^{-1} in 2013 and $-133\pm^{67}_{63}$ Tg CO_2 yr^{-1} in 2014, whereas for the JULES inversion it is 219 ± 87 Tg CO_2 yr^{-1} in 2013 and $164\pm^{67}_{65}$ Tg CO_2 yr^{-1} in 2014. The average summer difference for the CARDAMOM inversion is $135\pm^{111}_{108}$ Tg CO_2 yr^{-1} in 2013 and $263\pm^{82}_{83}$ Tg CO_2 yr^{-1} in 2014, whereas for the JULES inversion it is $94\pm^{104}_{107}$ Tg CO_2 yr^{-1} in 2013 and 312 ± 85 Tg CO_2 yr^{-1} in 2014. The prior sink in June as estimated by the JULES model is nearly twice that of CARDAMOM and posterior estimates tend to agree with the CARDAMOM prior in this month.

Figure 3.6c shows the daily minimum and maximum in the posterior net biospheric estimates for 2014. It is worth remembering at this point that while the temporal resolution of the inversion is flexible, it can go down to a minimum resolution of one day (as explained in Sect. 2.2.4). Therefore, the diurnal profile of TER and GPP for each model is imposed, however it can be scaled up or

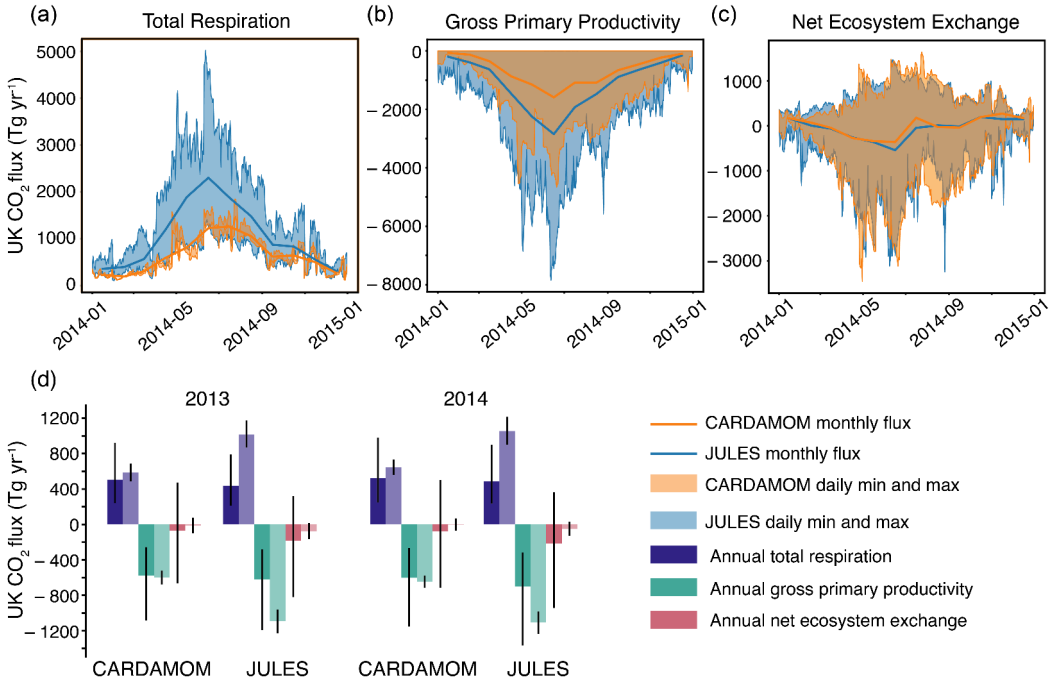

Fig. 3.6: Posterior UK fluxes in 2014. (a-c) Comparison of monthly fluxes and minimum and maximum daily values for TER, GPP and NEE respectively resulting from JULES inversion (blue) and CARDAMOM inversion (orange). (d) Annual CO_2 fluxes for TER, GPP and NEE for 2013 and 2014 from CARDAMOM and JULES inversions. Dark bars denote prior annual fluxes, light bars denote posterior annual fluxes. Uncertainty bars represent 5th – 95th percentile.

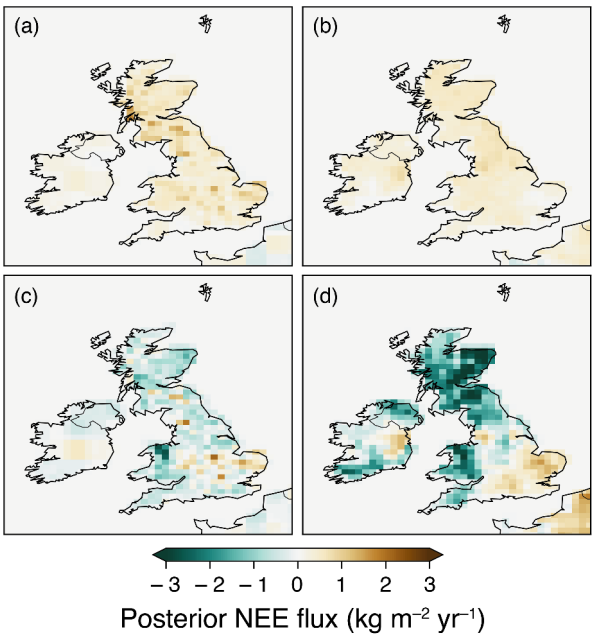

Fig. 3.7: Posterior net biospheric (NEE) flux maps averaged over winter 2013 (December 2013, January – February 2014) and summer 2014 (June – August 2014). (a) Winter NEE flux from CARDAMOM inversion. (b) Winter NEE flux from JULES inversion. (c) Summer NEE flux from CARDAMOM inversion. (d) Summer NEE flux from JULES inversion.

down from day to day. For both inversions, the posterior NEE flux has a similar profile. Compared to Fig. 3.1c the inversion tends to a seasonal cycle in daily maximum uptake that resembles that of the JULES model prior, with a turning point in maximum uptake occurring abruptly between June and July, a steep gradient in spring and a shallow gradient in autumn. On the other hand, the seasonal cycle in daily maximum source resembles that of the CARDAMOM model prior, which has a stronger seasonal variation compared to that of the JULES model prior, albeit with a larger amplitude. This would suggest that the underestimation in net spring flux seen in the JULES prior is generally due to the model underestimating the spring source, rather than overestimating the spring sink. It also suggests that the overestimation in net summer flux in the CARDAMOM prior is possibly a combination of the model overestimating the summer sink and underestimating the summer source. The overestimation in the net summer flux in JULES is more likely to be due to an underestimation of the summer source. However, as diurnal fluxes vary on a scale nearly an order of magnitude larger than that of the monthly fluxes, it is clear that any relatively small changes in the maximum source or sink will have a relatively large effect on the daily net flux. Therefore, as was also discussed in Sec. 2.3.1, the monthly net flux is the more robust result here and conclusions cannot be confidently drawn from the sub-monthly results.

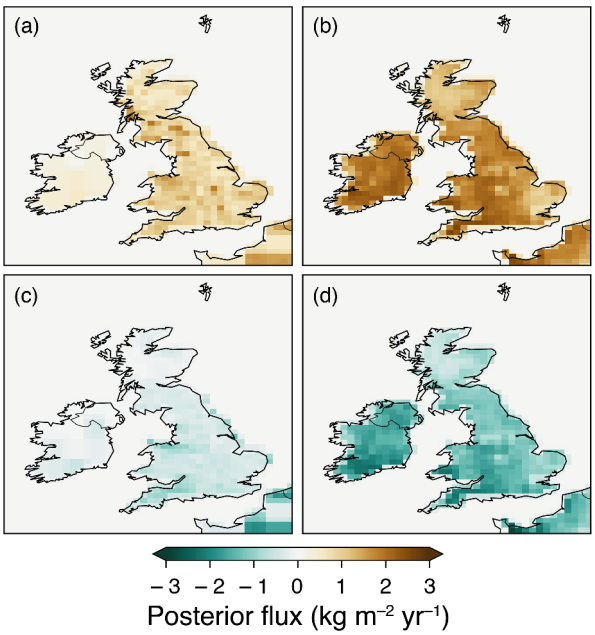

Fig. 3.8: Posterior TER and GPP flux maps averaged over winter 2013 (December 2013, January – February 2014). (a) Winter TER flux from CARDAMOM inversion. (b) Winter TER flux from JULES inversion. (c) Winter GPP flux from CARDAMOM inversion. (d) Winter TER flux from JULES inversion.

3.3.3 Posterior spatial distribution

Figure 3.7 shows mean posterior net biospheric fluxes (NEE) for winter 2013 and summer 2014 from both the CARDAMOM and JULES inversions. In winter 2013, posterior NEE fluxes from the CARDAMOM inversion are fairly heterogeneous and are largest over south-west Scotland and east and central England. This posterior spatial distribution is roughly similar to the prior. From the inversion using JULES prior fluxes, the posterior net biospheric flux is much smoother than it is for the inversion using CARDAMOM. It is largest in north-west England and almost zero in east England. The whole of south/central England, Wales, and Northern Ireland have increased posterior winter fluxes compared to the prior, turning these areas from a net sink in the prior to a net source in the posterior.

In summer 2014, NEE fluxes from the two inversions display many similarities, with areas of net source in east, central (extending further south in the JULES inversion) and north-west England and areas of net sink elsewhere. However, the net sink in the JULES inversion is larger than the CARDAMOM inversion in Scotland, south Wales, Northern Ireland and south-west England. This differs from the prior flux maps, which have only very small areas of small net uptake in central England in CARDAMOM and in east England in JULES. Both the CARDAMOM and JULES posterior fluxes generally display reduced uptake compared to the prior, except in north Wales.

Table 3.2: Prior and posterior fit to data statistics for the inversion period 2013-2014. R^2 and RMSE are calculated monthly and averaged over this period. Values in brackets are the posterior fit statistics for the corresponding net flux inversions. *Weybourne data (from February to December 2013) is used for validation of the results only and is not included in the inversions.

CARDAMOM inversion						
Measurement site	Prior R^2	Posterior R^2	Prior RMSE	Posterior RMSE	Prior mean bias	Posterior mean bias
Mace Head	0.20	0.59 (0.54)	2.88	1.53 (1.62)	-1.19	0.55 (0.38)
Ridge Hill	0.26	0.67 (0.61)	3.82	2.09 (2.30)	-1.27	-0.10 (-0.05)
Tacolneston	0.22	0.61 (0.56)	3.92	2.20 (2.44)	-1.63	-0.25 (-0.28)
Heathfield	0.21	0.71 (0.58)	4.07	1.88 (2.31)	-1.99	0.11 (0.21)
Bilsdale	0.20	0.60 (0.55)	4.62	2.02 (2.23)	-3.68	-0.52 (-0.58)
Angus	0.35	0.67 (0.63)	3.09	1.28 (1.41)	-2.35	-0.01 (0.00)
All sites	0.22	0.63 (0.58)	3.55	1.90 (2.10)	-1.73	0.02 (-0.01)
*Weybourne	*0.13*	*0.31 (0.28)*	*6.17*	*5.08 (5.32)*	*2.89*	*2.25 (2.37)*
JULES inversion						
Measurement site	Prior R^2	Posterior R^2	Prior RMSE	Posterior RMSE	Prior mean bias	Posterior mean bias
Mace Head	0.29	0.66 (0.56)	2.84	1.26 (1.44)	-1.33	0.16 (-0.01)
Ridge Hill	0.33	0.67 (0.59)	3.86	2.14 (2.41)	-1.14	-0.21 (-0.05)
Tacolneston	0.24	0.53 (0.52)	4.06	2.71 (2.70)	-1.84	-0.89 (-0.74)
Heathfield	0.28	0.66 (0.57)	4.07	2.14 (2.38)	-2.43	-0.25 (-0.23)
Bilsdale	0.33	0.61 (0.62)	4.53	2.10 (2.19)	-3.60	-0.96 (-0.82)
Angus	0.43	0.67 (0.62)	2.85	1.39 (1.55)	-1.78	0.43 (0.48)
All sites	0.25	0.58 (0.52)	3.60	2.11 (2.25)	-1.75	-0.27 (-0.21)
*Weybourne	*0.16*	*0.29 (0.23)*	*5.85*	*5.10 (5.49)*	*2.63*	*2.07 (2.56)*

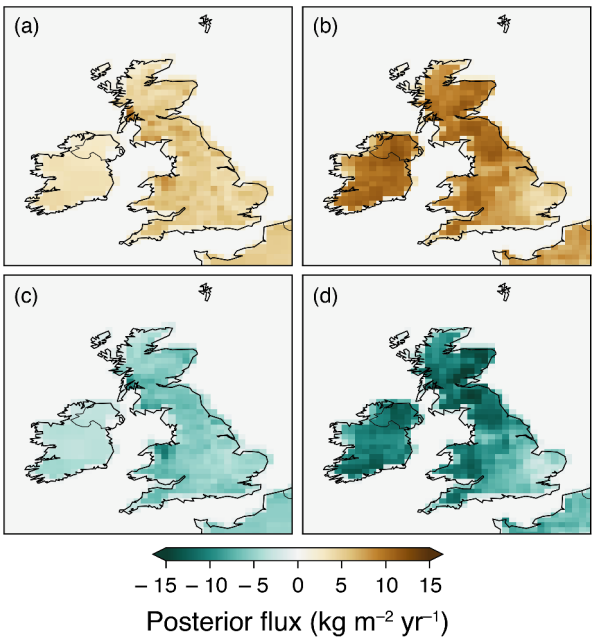

Fig. 3.9: Posterior TER and GPP flux maps averaged over summer 2014 (June – August 2014). (a) Summer TER flux from CARDAMOM inversion. (b) Summer TER flux from JULES inversion. (c) Summer GPP flux from CARDAMOM inversion. (d) Summer GPP flux from JULES inversion.

3.3.4 Model-data comparison

Agreement between the data and the posterior simulated mole fractions at the measurement sites used to constrain the inversion is greatly improved compared to prior simulated mole fractions, with R^2 values increasing by a minimum of 0.24 and up to 0.5 (to give values ranging between 0.53 and 0.71) and RMSE decreasing by at least 1.35 ppm and up to 2.6 ppm (to give values ranging between 1.26 ppm and 2.71 ppm). Table 3.2 shows all statistics for the prior and posterior mole fractions compared to the observations of atmospheric CO_2 concentrations. Overall, looking the the statistics for "All sites", the fits are relatively similar between the CARDAMOM and JULES inversions, however the CARDAMOM inversion does provide a slightly better fit by these metrics. In terms of R^2, the best fit to the data is observed at Heathfield in the CARDAMOM inversion and Angus in the JULES inversion. In terms of RMSE, the best fit to the data is observed at Angus in the CARDAMOM inversion and Mace Head in the JULES inversion. The smallest posterior mean bias is observed at Angus in the CARDAMOM inversion and Ridge Hill in the JULES inversion. Therefore, there are some small spatial differences in how well each of the inversions is able to fit the data but no clear indication of which areas of posterior flux might be subject to the largest improvement in either inversion. Figures 3.10 and 3.11 show the residual mole fractions in 2014 and indicate that residuals are somewhat larger during the summer than the winter.

To test the posterior results against data that has not been included in the inversion, the posterior fluxes have been used to simulate mole fractions at Weybourne Atmospheric Observatory (see Fig. 1.4a

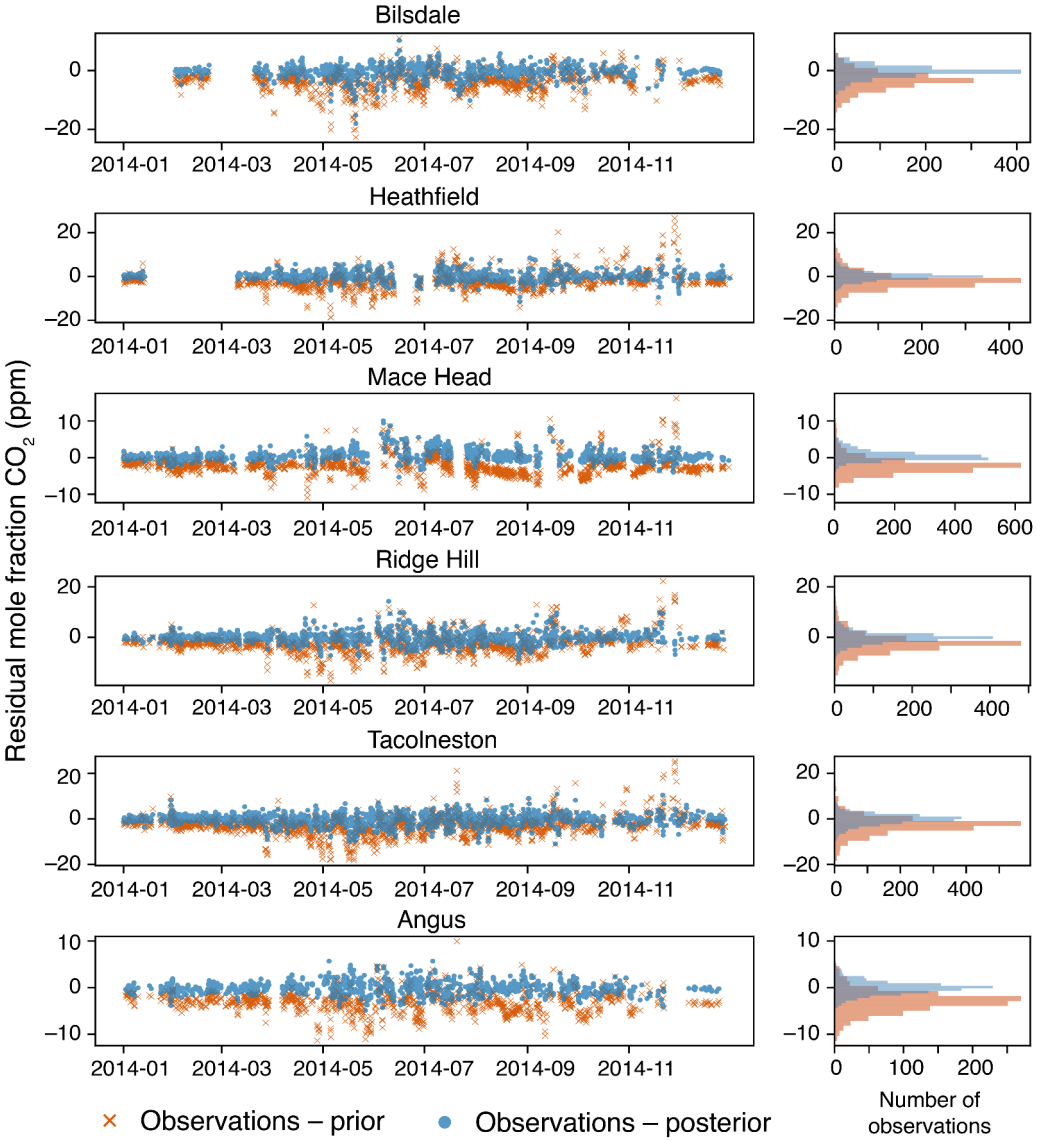

Fig. 3.10: Left: Residual mole fractions for prior and posterior modelled CO_2 concentrations in 2014 using CARDAMOM prior biospheric fluxes. Right: Histogram of prior residuals (orange) and posterior residuals (blue). The mean of the histogram represents the mean bias.

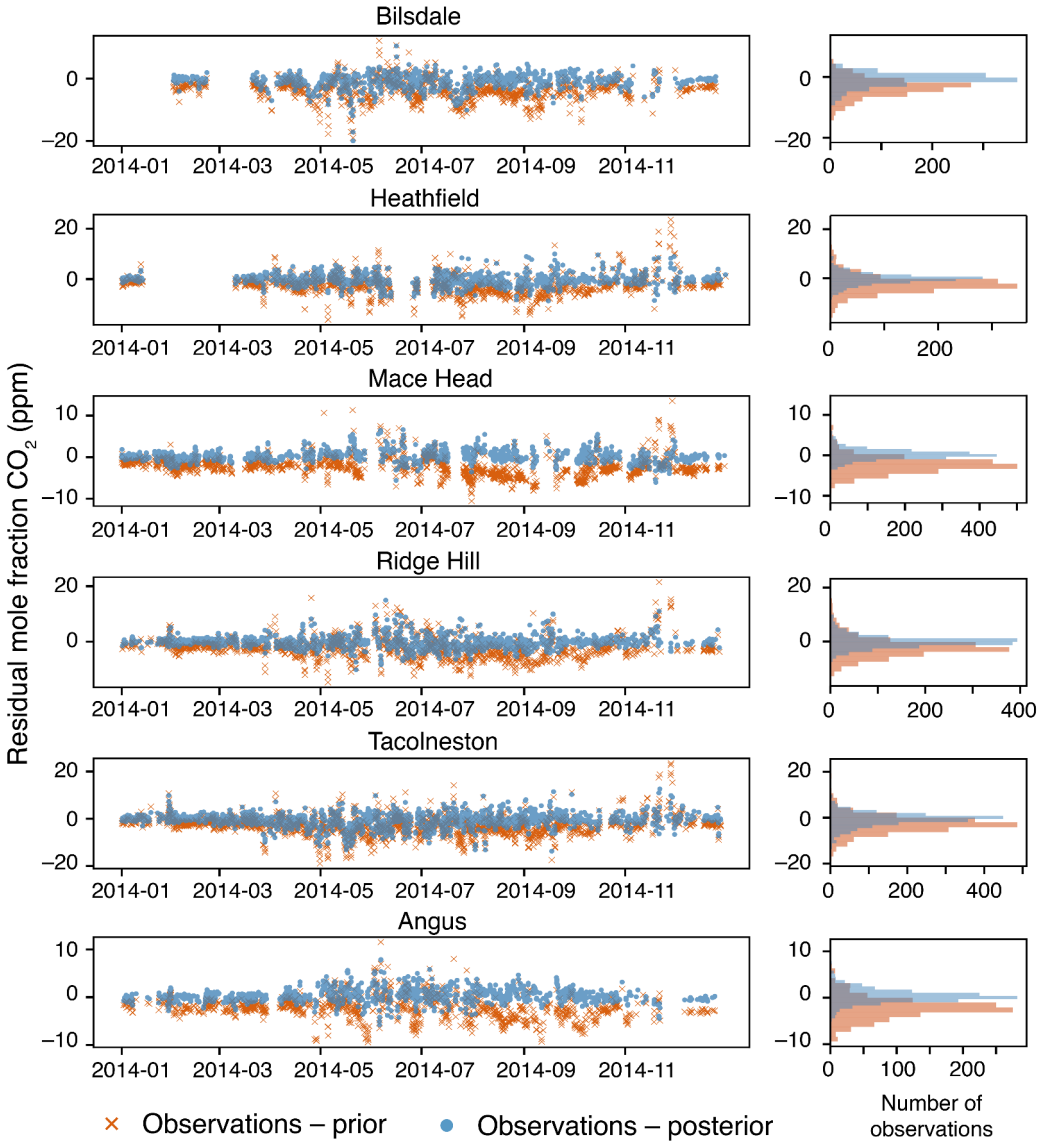

Fig. 3.11: Left: Residual mole fractions for prior and posterior modelled CO_2 concentrations in 2014 using JULES prior biospheric fluxes. Right: Histogram of prior residuals (orange) and posterior residuals (blue). The mean of the histogram represents the mean bias.

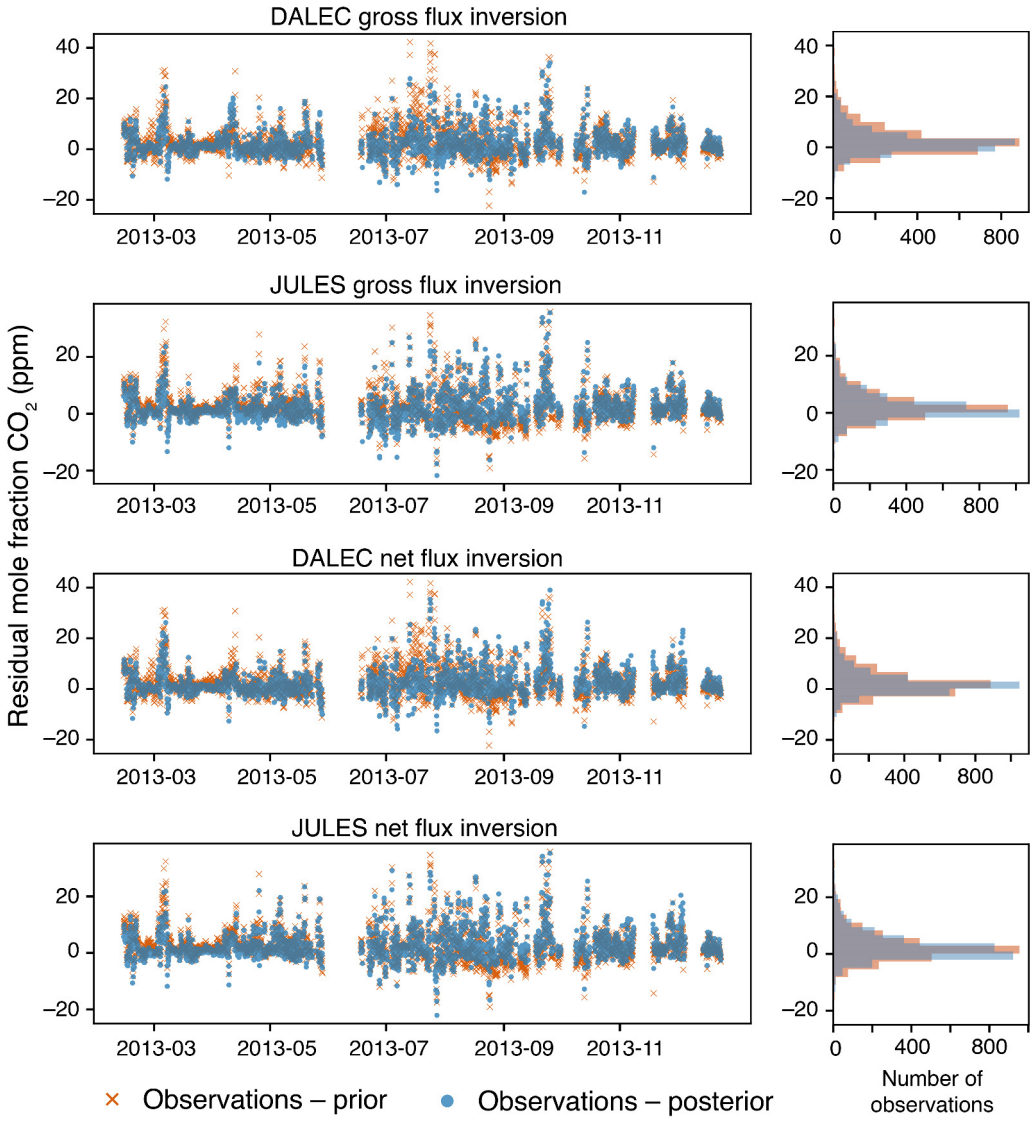

Fig. 3.12: Left: Residual mole fractions for modelled CO_2 concentrations at Weybourne in 2013 using prior CARDAMOM and JULES fluxes, and posterior CARDAMOM and JULES fluxes from both the gross (scaling GPP and TER separately) and net (scaling just NEE) flux inversions. Weybourne data was not included in the inversions. Right: Histogram of residuals. The mean of the histogram represents the mean bias.

for location in relation to the other sites and Table 2.1 for site information). The statistics of fit to the data are given in italics in Table 3.2 and show an improvement in R^2 of 0.18 with the CARDAMOM inversion and 0.13 with the JULES inversion, an improvement in RMSE of 1.09 ppm with the CARDAMOM inversion and 0.75 ppm with the JULES inversion and an improvement in the mean bias of 0.64 ppm in the CARDAMOM inversion and 0.56 in the JULES inversion. These results show that the a posteriori fluxes improve the fit to the data at a measurement station not included in the inversion. The results are very similar between the two inversions at this site, but suggest that the CARDAMOM inversion may perform slightly better, at least in this region of the UK. Figures 3.12 shows the residual mole fractions at Weybourne for each of the inversions carried out in this work.

3.4 Discussion

3.4.1 Inversion performance

Solving for both TER and GPP separately allows the JULES-prior and CARDAMOM-prior inversions to converge to a similar posterior solution. Using two very different prior NEE flux estimates, two similar posterior NEE flux estimates are produced that have a similar seasonal amplitude, and agree on the majority of monthly and all annual fluxes within the estimated uncertainties. This indicates that the results are driven primarily by the data and are less strongly influenced by the prior. However, when the same inversion is carried out that scales NEE instead of the gross fluxes (Fig. 3.13) the two posterior flux estimates do not converge on a common result. The posterior seasonal cycles remain relatively unchanged compared to the prior and annual net biospheric flux estimates tend to be similar to, or larger than, the prior. These annual net biospheric flux estimates are therefore 3 – 39 times smaller than the inversion that separates GPP and TER, meaning the posterior estimates from the two types of inversions do not overlap, even within estimated uncertainties. An evalutation of the statistics of how well the NEE inversions fit the data (Table 3.2) shows that they do not perform as well as the separate GPP and TER inversions. However, this is to be expected to some degree, because separating the two sources gives the inversion more degrees of freedom to fit the data.

As recommended by Tolk et al. (2011) and discussed in Sect. 2.3.1, this method only hopes to achieve an improved estimate for the net fluxes rather than the gross GPP and TER fluxes themselves. The correlation between the spatial and temporal distribution of GPP and TER can be seen in summer and winter flux maps (Fig. 3.8 and 3.9) and in the posterior annual flux estimates in Fig. 3.6d, in particular where JULES TER and GPP show similarly large differences from the prior. This could also be a result of the imposed diurnal cycle, as it would appear the posterior TER flux in the JULES inversion is tending to a higher daily minimum, matching that of the CARDAMOM prior, and may ultimately be trying to move towards a smaller diurnal variation in TER. However, because the whole diurnal cycle must be scaled, the daily maximum TER must also increase and may mean the GPP must increase, causing increased uptake to compensate for the increased source from TER. Allowing flexibility on sub-daily timescales may lead to similar estimates of GPP and TER between the two

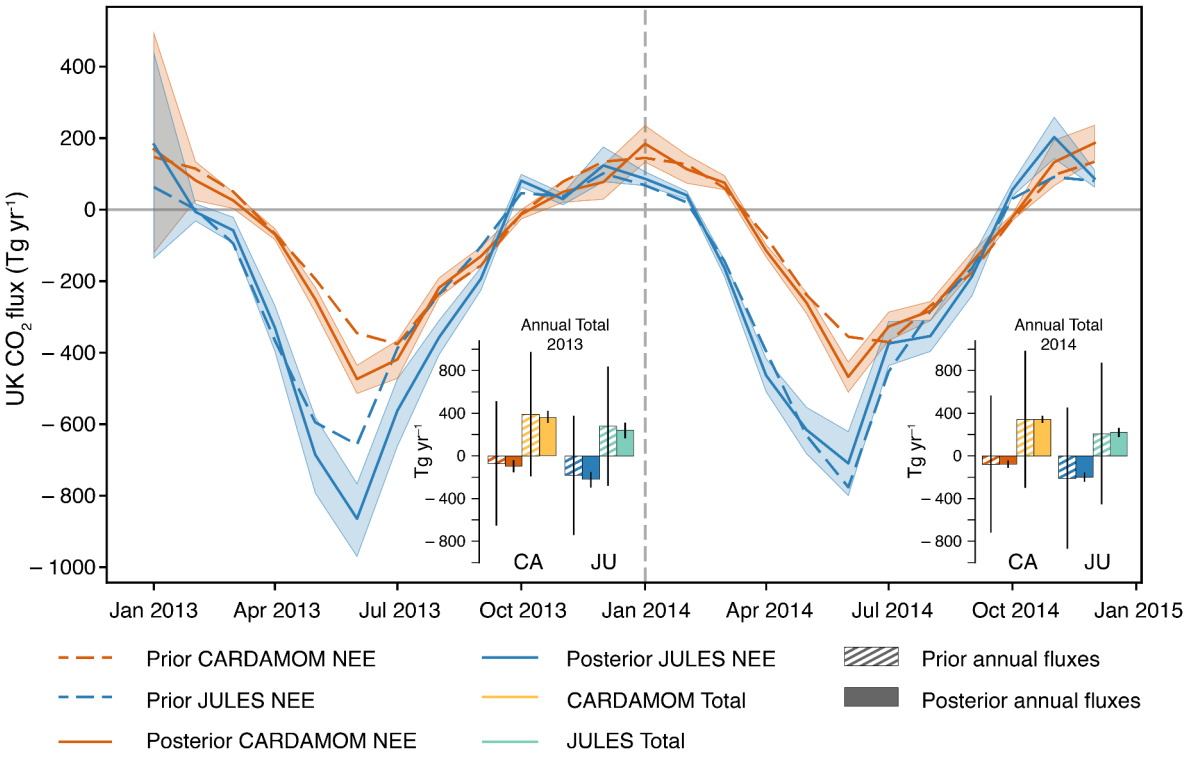

Fig. 3.13: Posterior monthly net UK CO_2 flux (emission to the atmosphere is a positive flux) for the inversion that scales only NEE rather than GPP and TER separately. Orange and blue monthly fluxes are posterior net biospheric (NEE) fluxes. Prior biosphere fluxes from JULES and CARDOMOM are shown in dashed orange and blue lines respectively. Shading represents 5th – 95th percentile. The bar charts represent annual net UK CO_2 flux for 2013 (left) and 2014 (right). Hashed bars denote prior annual fluxes, solid bars denote posterior annual fluxes. The bar colours correspond to the line colours: left hand bars for each model are NEE fluxes, right hand bars for each model are total fluxes (NEE + fixed sources). Uncertainty bars represent 5th – 95th percentile. CA – CARDAMOM. JU – JULES. NEE prior PDF (x_{NEE}) has Gaussian uncertainty distribution and its standard deviation hyper-parameter ($\sigma_{x_{NEE}}$) has a uniform distribution with a range reflecting an absolute uncertainty of approximately 40–400 Tg (see Table 2.3 for the comparable set-up for the separate GPP and TER inversion).

inversions with different priors. However, questions remain over whether there is enough temporal information for this to be the case.

The fact that common monthly and annual posterior net biospheric flux estimates are reached when the prior biospheric fluxes are spatially and temporally different would suggest that the choice of prior is not necessarily a major factor in guiding the inversion result for this network, when GPP and TER are scaled separately. In this respect, it is also particularly encouraging that the seasonal cycles in the posterior diurnal range are similar for both inversions (Fig. 3.6c).

3.4.2 Differences between prior and posterior NEE estimates

The posterior seasonal cycle in both inversions differs significantly from the prior. This implies that the biospheric models used to obtain prior GPP and TER fluxes are either over- or under-estimating the strength of some processes, or they are omitting some processes altogether. The largest differences between the posterior solution and the prior model output are seen in spring and summer. In Sect. 3.3.2 it has been shown that spring differences arise from an underestimation of the net spring flux in the JULES model and a correct/overestimation of the net spring flux in CARDAMOM. However, in summer (particularly in 2014) the posterior net UK fluxes are higher than both priors in July and August.

One process that occurs during the months July and August is crop harvest. This is not taken into account in either of the models of the biosphere used in this work, thereby providing a possible explanation for the differences between the posterior and prior in these months. Harvest typically occurs between July and September and arable agricultural land covered 26% of the UK in 2013 and 2014 (DEFRA, 2014, 2015), so there is potential for unaccounted activity in this area to cause large changes to net CO_2 fluxes. The areas of net source in summer (shown in Fig. 3.7) do also coincide with areas of large-scale agriculture (e.g. east and central England). Crop harvest potentially changes the biosphere in the following ways. Firstly, crops mature en masse, leading to an abrupt loss of productivity. Secondly, during harvest there is an abrupt removal of biomass and input of harvest residues on the field. This increases litter input that is readily available for decomposition, increasing heterotrophic respiration. Thirdly, when the field is ploughed the soil is disturbed, which will again increase heterotrophic respiration. Finally, when the crop is no longer covering the soil surface this layer can become drier and the energy balance is altered. In Smallman et al. (2014), the reduction in atmospheric CO_2 concentration due to crop uptake is reported for 2006 to 2008 and an abrupt increase in atmospheric CO_2 can be seen between June (peak sink) and August, where CO_2 uptake from crops is halted as a result of harvest. This may explain the abrupt shift from net sink to net zero / net source observed between July and August in CARDAMOM in 2013 and June and July in both models in 2014. The earlier net sink to net source transition time in 2014 does coincide with a year of early harvest (DEFRA, 2015). Later in the summer, there may be some plant regrowth in ploughed fields leading to increased GPP. This would be consistent with the shallower gradient observed in net biospheric fluxes between September and October 2013 in the CARDAMOM posterior estimate,

between August and September 2014 in the JULES posterior estimate and the decrease in net flux observed between July and September 2014 in the CARDAMOM posterior estimate.

If agricultural activity is the source of the July, August, September difference between prior and posterior UK NEE estimates, then it could amount to emissions of 4 – 10% of currently reported annual anthropogenic emissions in 2013 and 17 – 19% in 2014. However, other explanations for this difference could be large uncertainties in the seasonal disaggregation of anthropogenic fluxes, uncertainties in the transport model, or a combination of over and underestimation of other biospheric processes.

3.4.3 Implications for UK CO_2 estimates

The results of UK biospheric CO_2 fluxes using this set-up suggest the UK biosphere is roughly in balance, whereas prior estimates from models of the biosphere estimate a net sink. Even when an uncertainty on our anthropogenic fluxes of 10% is assumed (a conservative estimate), inversions using both models still give mean posterior estimates that are larger than their respective priors (see Fig. 3.5). Therefore, when using models of the biosphere to contribute to inventory estimates of CO_2 emissions, care must be taken to attribute sufficient uncertainties to model estimates, otherwise the amount of CO_2 taken up by the biosphere on an annual basis may be overestimated. Methods, such as the one described here, could provide an important constraint on the UK's biospheric CO_2 fluxes as carbon sequestration processes, such as reforestation, and other land use change activities are increasingly used as policy solutions to contribute to carbon targets.

3.5 Conclusions and future work

Here, the framework developed in Chapter 2 that takes advantage of recent innovation in atmospheric inverse modelling and a relatively dense regional network of measurement sites is used to estimate net biospheric CO_2 fluxes in the UK . Two inversions are carried out using prior flux estimates from two different models of the biosphere, CARDAMOM and JULES. Fluxes of GPP and TER are scaled separately in the inversions. Despite significant differences in prior biospheric fluxes, monthly and annual posterior flux estimates are found to be consistent, suggesting that the choice of model to provide biospheric CO_2 flux priors in the inversion is not a major factor in guiding the inversion result with this framework and network.

Further to the conclusions of "Test 2" in Chapter 2, NEE is found to be more robustly derived if GPP and TER are solved separately, and then combined a posteriori. These results suggest that inversions that scale only NEE could be underestimating net CO_2 fluxes, as posterior estimates are 3 – 39 times smaller than those obtained using an inversion where GPP and TER are separated.

The UK biosphere is found to be roughly in balance, with annual net fluxes (averaged over the study period) of –8$\pm$79 Tg CO_2 yr^{-1} and –64$\pm$85 Tg CO_2 yr^{-1} according to the CARDAMOM and JULES

inversions respectively. These mean annual fluxes are systematically higher than their respective priors, implying that net biospheric fluxes are underestimated (i.e. GPP fluxes are overestimated or TER flues are underestimated) in the models of the biosphere used in this study. The posterior seasonal cycles from both inversions differ significantly from the prior seasonal cycles and have a reduced amplitude of 90% and 76% of the prior amplitude in 2013 according to the CARDAMOM and JULES inversions respectively, and 85% of the prior amplitude in 2014 according to the JULES inversion. However, the posterior seasonal cycle amplitude from the CARDAMOM inversion in 2014 is increased by 122%. These results suggest an overestimated net spring flux in the JULES model and an overestimation of the net summer flux in both models of the biosphere. It is proposed that the difference seen between the prior and posterior flux estimates in summer and early autumn could be a result of the disturbance caused by crop harvest, leading to abrupt reduction in plant CO_2 uptake and increase in respiration sources, as crop harvest is not taken into account in either model. However, this hypothesis is just one of a combination of uncertain factors that could lead to the differences seen, so further work would be needed to investigate the importance of crop harvest in UK CO_2 emissions.

This work represents a first step towards looking at the UK biospheric CO_2 budget with a hierarchical Bayesian trans-dimensional MCMC inverse modelling framework. Further work is required to robustly constrain biospheric CO_2 fluxes, through comparison with other model set-ups.

Chapter 4

European-scale carbon dioxide flux estimation

4.1 Introduction

During this PhD project, the opportunity arose to take part in a regional-scale inverse modelling inter-comparison project focussing on European biospheric CO_2 fluxes. This project is called EUROCOM and is funded via the Swedish Research Council and the French-Swedish collaborative agreement on Climate, Environment and Energy (https://eurocom.icos-cp.eu). Participating with EUROCOM has provided a chance to test the inversion set-up set out in Chapter 2 with a different, longer dataset, a larger domain and a more mature model of prior biospheric fluxes. It has also enabled a platform to compare the results of the system presented here to other state-of-the-art systems of greater maturity.

Estimating European scale CO_2 fluxes from the terrestrial biosphere is important because all European countries have pledged to reduce emissions of CO_2 in response to the Paris Agreement and a significant portion of mitigation efforts include increasing carbon uptake from the biosphere. The ability to accurately quantify terrestrial sources and sinks will enable individual countries and Europe as a whole to track their progress in achieving the emissions reduction targets proposed during the process of the Paris Agreement.

Europe is a complex region due to the heterogeneity of land-use over small spatial scales. Since 1980 the scientific community has made a concerted effort to estimate Europe's biospheric CO_2 budget. Thus far, attempts have come from a number of different methods and results range widely from a net sink of -5600 Tg CO_2 yr^{-1} to a small net source of 1000 Tg CO_2 yr^{-1} (Fig. 4.1).

The first attempts came out of global inverse modelling studies and inter-comparisons such as Transcom. Initially these studies produced very diverse estimates for the global land sink (the net flux of CO_2 into the biosphere), which led to the development of intercomparisons to try to understand the source of these discrepancies. The latest Transcom results for Europe from Peylin et al. (2013) are shown in Fig. 4.1 along with those of other global inverse modelling studies (Gurney et al., 2004;

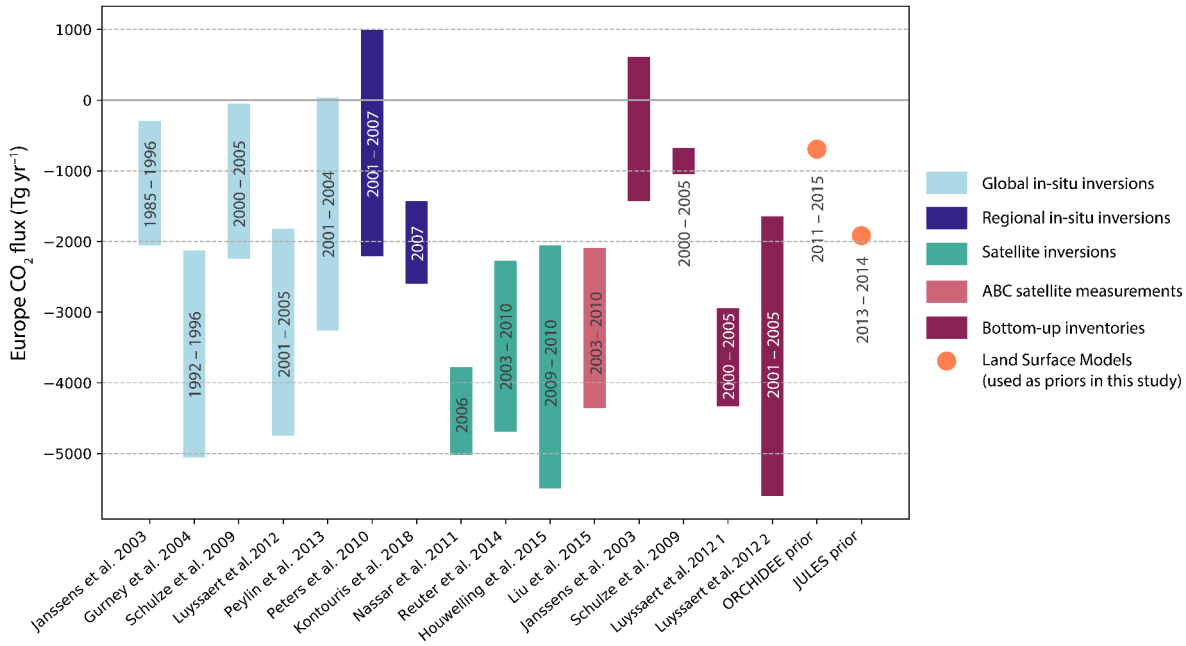

Fig. 4.1: Estimates of European biospheric CO_2 budget from previous studies. The majority of uncertainty estimates from the previous studies are 1σ, however it is sometimes difficult to calculate comparable uncertainty estimates.

Janssens et al., 2003; Luyssaert et al., 2012; Schulze et al., 2009), which demonstrates the large range of estimates (from -5060 to 40 Tg CO_2 yr^{-1}).

As the resolution of inverse modelling studies has improved and in-situ measurement networks have developed, scientists have taken a more focussed approach to estimating the European biospheric CO_2 budget using regional inverse modelling techniques (Kountouris et al., 2018a; Peters et al., 2010). These regional studies shown in Fig. 4.1 are at the upper end of the estimates produced by the global studies and suggest that Europe could be a net source of biospheric CO_2 or a net sink.

However, a weakness of global inverse modelling is that it lacks spatial resolution as fluxes are found on continental scales, and inverse modelling in general is criticised for poor spatial distribution of in-situ observations (Bruhwiler et al., 2011). To solve these problems, inversions using satellite data were developed to take advantage of the better spatial coverage of data achieved using thermal infrared spectroscopic satellite measurements of atmospheric CO_2 concentrations that are sensitive to tropospheric emisisons (Nassar et al., 2011) and near-infrared measurements (Houweling et al., 2015; Reuter et al., 2014). The scale of these measurements is also better representative of transport model scales. Results from these studies found that Europe may be a considerable sink of biospheric CO_2, which is at the lower end of estimates from global inverse studies and up to double the sink at the lower end of estimates from regional inverse studies. Alternative methods to deduce Europe's biospheric CO_2 budget using satellites include estimates of above-ground biomass (ABC) from passive

microwave satellite measurements (Liu et al., 2015). These results agreed with other satellite studies and found that the largest area of uptake is in eastern Europe.

Many bottom-up studies have also estimated the European biospheric CO_2 budget, shown in Fig. 4.1, and arrive at very different results spanning the range of results from global in-situ, regional in-situ and satellite inversions (Janssens et al., 2003; Luyssaert et al., 2012; Schulze et al., 2009). These studies have used inventory and eddy flux covariance data to build their estimates. Land Surface Models (LSMs) such as ORCHIDEE (Krinner et al., 2005) and JULES (Best et al., 2011; Clark et al., 2011) also provide bottom up estimates and these roughly lie in the middle of the range of results.

The disagreement between these different methods is puzzling and the question of how the community should proceed is concisely discussed in Reuter et al. (2016). If the majority of the large sink seen by satellites is indeed in eastern Europe, then the lack of a dense network of measurement stations in this area could explain why regional inverse modelling studies are missing this sink and arriving at larger estimates for the net CO_2 budget. Therefore, further developing the measurement network in eastern Europe could help to confirm this sink (Chevallier et al., 2010; Reuter et al., 2014). However, due to the inability to collect satellite data during cloudy conditions, there are biases in the satellite data that may not be accounted for. This has been suggested as another source of the discrepancy between satellite and in-situ data inversions (Feng et al., 2016) but cannot be proven without additional measurements. The inter-annual variability of the European biospheric carbon budget should also be considered as the studies presented here all cover different time periods, ranging from 1985 to 2015, and there is evidence for European, and indeed global, sources and sinks to be affected by large-scale meterological phenomena such at the North Atlantic Oscillation and the El Niño Southern Oscillation (Bastos et al., 2016). However, in an inversion comparison carried out by Chevallier et al. (2014) that investigated the difference between assimilating in-situ and satellite data over the same time period, the size of the sink was increased in inversions that included satellite data.

Along with the need for additional in-situ measurements and a call for improved satellite retrieval algorithms and inverse modelling techniques from Reuter et al. (2016), there is also space for a concerted collaborative effort to improve the estimates from regional inversions since the number of regional inverse studies remains fairly small. EUROCOM takes a similar form to that of Transcom and is the first regional inversion inter-comparison focussed on Europe. It aims to further knowledge of the European biospheric CO_2 budget by taking advantage of the Integrated Carbon Observing System (ICOS) network. In Europe, researchers benefit from relatively dense coverage of tall tower and surface sites and flask data and this data is being amalgamated into a single accessible dataset through ICOS. Seven different inverse systems are participating in the project from different institutes across Europe. Whilst the dataset (from ICOS) and prior anthropogenic emissions (from EDGAR) are provided, the modelling groups are free to make their own choices about the inversion set-up, prior biospheric fluxes and atmospheric transport model. The work presented here contributes to EUROCOM by incorporating an additional atmospheric transport model (NAME) and an innovative inverse modelling set-up using hierarchical Bayesian trans-dimensional MCMC.

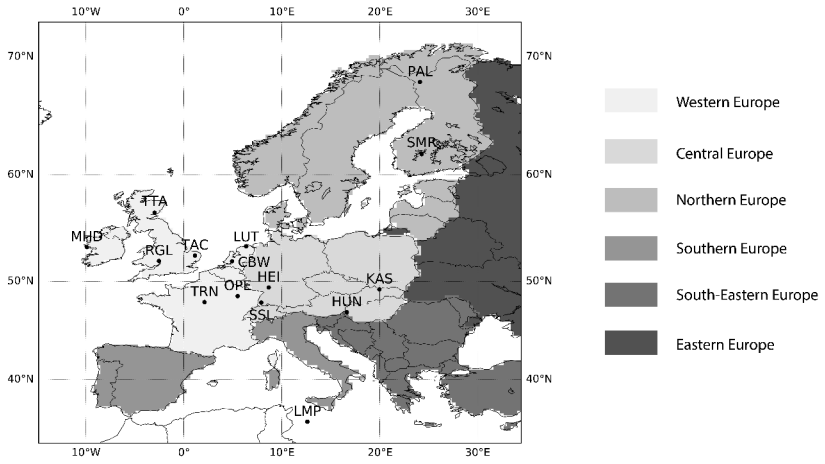

Fig. 4.2: The EUROCOM domain and location of atmospheric measurement stations used in this study. Shaded areas show the regions used for the analysis in Section 4.3.3.

4.2 Method

The EUROCOM project is mostly very flexible in terms of the inverse modelling set-up. Therefore, the method used for the work of this chapter, and to contribute to EUROCOM, is based on the method developed in Chapter 2. However, here the sub-domain is extended to cover the common EUROCOM domain and many more measurement sites from the ICOS network are incorporated from across Europe. Different prior and fixed fluxes have been used since the anthropogenic emissions dataset is dictated by the EUROCOM protocol and involvement in the project has granted access to new biospheric flux datasets.

4.2.1 Data

Data has been used from 15 tall tower and surface stations, collected between 2011 and 2015. This data is provided by the ICOS network, and in some cases where the ICOS validation process has not been completed the data is described as "pre-ICOS" (see Table 4.1). The stringent quality controls of ICOS ensure that the data are comparable across the network. For more information on the standard set-up required to become a labelled ICOS atmospheric station, see the ICOS Stakeholder Handbook 2013 (at https://icos-atc.lsce.ipsl.fr/doc_public). The data from ICOS are hourly averaged and measurement uncertainty is derived from the sub-hourly standard deviation of the continuous data.

Figure 4.2 shows the location of the sites used in this work and Table 4.1 gives further site information. The majority of the sites are located in central and western Europe, with few sites in the north, east and south. Although not all ICOS stations have been used in the first stage of inversions with this set-up, this is generally representative of the spread of ICOS stations and ICOS is working hard to expand the network in these areas. As can be seen in Fig. 4.3, not all sites are available over

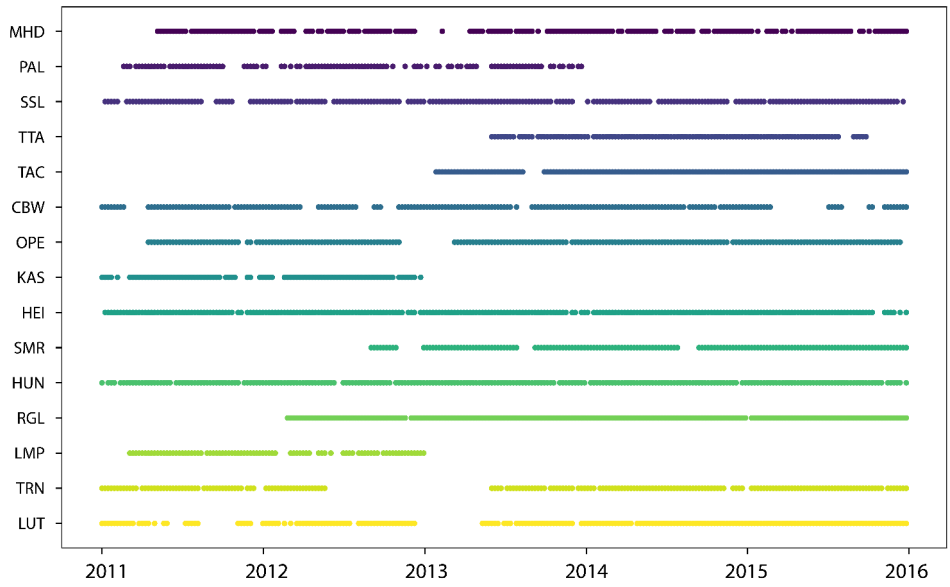

Fig. 4.3: The data availability and data points remaining following "local-lapse" filtering for each measurement site used in the inversion.

Table 4.1: Site information.

Site	**Site code**	**Country**	**Location**	**Inlet height** (m above) (ground level)	**Elevation** (m above) (sea level)	**ICOS status**
Mace Head	MHD	Ireland	53.326 °N, 9.904 °W	15	5	ICOS
Pallas	PAL	Finland	67.973 °N, 24.116 °E	5	565	ICOS
Smear/Hyytiala	SMR	Finland	61.847 °N, 24.295 °E	125	181	ICOS
OPE	OPE	France	48.562 °N, 5.504 °E	120	390	Pre-ICOS
Heidelberg	HEI	Germany	49.417 °N, 8.674 °E	30	116	ICOS
Hegyhatsal	HUN	Hungary	46.950 °N, 16.650 °E	115	248	ICOS
Ridge Hill	RGL	UK	51.998 °N, 2.540 °W	90	204	ICOS
Trainou	TRN	France	47.965 °N, 2.112 °E	180	131	Pre-ICOS
Tacolneston	TAC	UK	52.518 °N, 1.139 °E	56	180	ICOS
Kasprowy	KAS	Poland	49.232 °N, 19.982 °E	5	1989	ICOS
Angus	TTA	UK	56.555 °N, 2.986 °W	222	400	ICOS
Lampedusa	LMP	Italy	35.510 °N, 12.610 °E	5	45	Pre-ICOS
Schauinsland	SSL	Germany	47.920 °N, 7.920 °E	12	1205	ICOS
Cabauw	CBW	Netherlands	51.971 °N, 4.927 °E	200	-1	ICOS
Lutjewad	LUT	Netherlands	53.404 °N, 6.353 °E	60	1	ICOS

the time period, therefore at any one time data from a minimum of 7 or a maximum of 13 sites may be incorporated into the inversion.

4.2.2 Atmospheric transport model

The NAME LPDM has been used in this work with the same footprint disaggregation as developed in Chapter 2. Data was averaged to two-hourly to match the temporal resolution of the NAME footprints and the measurement uncertainty used was an average of the hourly measurement uncertainty over the month. As for the work in the previous chapters, a "local-lapse" filter has been applied to the data to remove data points during times of low wind speeds and stable atmospheric conditions. In some cases the ICOS data product had been pre-filtered slightly differently to the GAUGE and UK-DECC data (used in Chapter 3) from the same sites to remove some of the larger concentration peaks that are present in these other datasets. For example, some of the higher concentrations seen at Mace Head data in November 2014 had been removed in the ICOS product.

4.2.3 Prior biospheric fluxes

The land-surface model ORCHIDEE (Krinner et al., 2005) has been used as an estimate of prior biospheric fluxes in this work. This is a more mature model with a longer timespan of available model output compared to the models JULES and CARDAMOM used in the work in Chapters 2 and 3. Three-hourly fluxes of GPP and Net Biome Production (NBP) were provided at 0.5° resolution. In contrast to NEE, NBP is the net amount of carbon in the ecosystem (as opposed to the flux to the atmosphere) resulting from the combination of photosynthesis and respiration processes (this part is known as net ecosystem production), and crucially it also includes the loss of organic matter related to non-respiratory processes (IGBP Terrestrial Carbon Working Group, 1998). These non-respiratory processes include insect damage, fire and human disturbance such as harvest and forest management. TER was found by removing GPP from NBP.

Since this element of human disturbance was omitted in the biospheric flux priors provided by JULES and CARDAMOM in Chapter 3 and potentially resulted in the under-estimation of summer/harvest time fluxes, it is of interest to compare the use of ORCHIDEE as a prior (with disturbance) to the use of JULES or CARDAMOM (without disturbance). JULES was chosen since it has high resolution over the whole domain, as opposed to CARDAMOM, which is only high resolution over the UK.

As for the work in Chapters 2 and 3, the prior biospheric fluxes were separated into their positive (TER) and negative (GPP) components, which was found to give a more data-driven result. However, an additional test was carried out using the ORCHIDEE NBP fluxes since the additional disturbance information in the prior may influence the performance of a gross vs net flux inversion. Analysis focusses on the aggregated net fluxes, as opposed to the gross fluxes, as this is believed to be more robust.

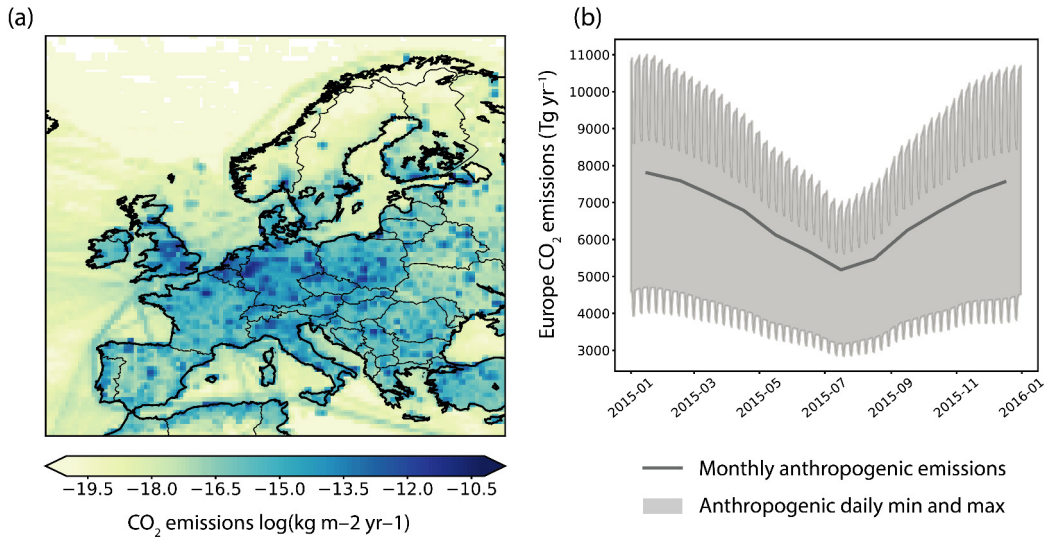

Fig. 4.4: EDGAR v4.3 anthropogenic emissions used to remove the anthropogenic component from the data prior to the inversion. (a): Average 2015 emissions map. (b): Monthly total Europe emissions for 2015 with shading representing the diurnal range.

4.2.4 Fixed CO_2 fluxes

Anthropogenic and ocean fluxes are forward modelled and removed from the data prior to the inversion. In this EUROCOM study the ocean fluxes are from Takahashi et al. (2009), and a common prior anthropogenic dataset has been provided. This dataset (shown in Fig. 4.4) is based on EDGARv4.3 CO_2 emissions from 2010, updated using BP fuel consumption statistics from 2016, with temporal extrapolation and disaggregation based on MACC-TNO (described in the CO_2 release and Oxygen uptake from Fossil Fuel Emission Estimate (COFFEE) dataset, Steinbach et al., 2011).

4.2.5 Inversion set-up

The inversion set-up used here is the same as the one set out in Chapter 2, with some small differences. Firstly, as prior information was only available at a three-hourly temporal resolution (see Section 4.2.3), once NAME footprints, prior fluxes and basis functions had been combined into the Jacobian matrix (see Sect. 1.4.5), the matrix was averaged to six-hourly temporal resolution along with the data. Secondly, the sub-domain is slightly larger to cover the whole of Europe and instead of fixing PFTs over the whole sub-domain, the area has been split up into 4 regions and 6/7 PFTs within which fluxes can be scaled up or down (Fig. 4.5).

Three inversions are carried out. Two inversions use ORCHIDEE prior biospheric fluxes, one of which scales the gross fluxes separately and the other scales the net flux. The third inversion uses JULES prior biospheric fluxes and scales the gross fluxes separately. The JULES output only covers 2013–2014 so the JULES inversion is shorter than the ORCHIDEE inversions, which cover the full 2011–2015 time period.

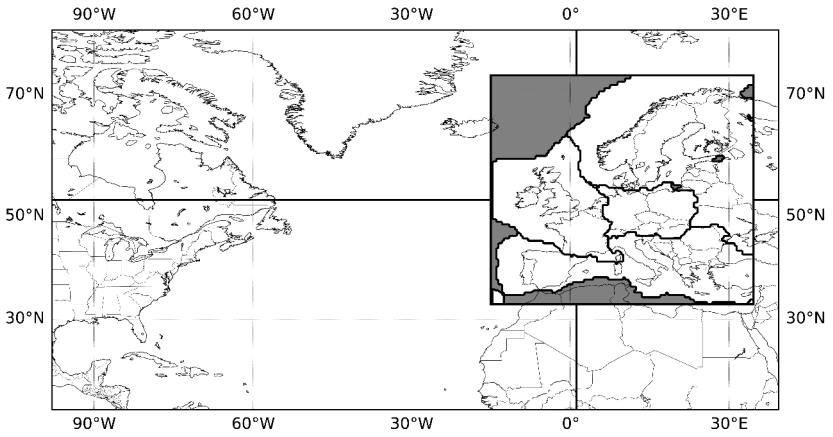

Fig. 4.5: The extent of the NAME domain, EUROCOM sub-domain (inner box) and regions within which PFTs may be scaled up or down.

4.3 Results

Analysing the inversion results over different scales reveals the regions in Europe that the set-up is able to resolve. Results are presented on the resolution of the inversion (the grid scale), at European scale and at smaller regional scales, alongside the fit of posterior modelled mole fractions to the data.

4.3.1 Grid scale fluxes

Figures 4.6 and 4.7 show the seasonal average prior and posterior fluxes respectively over the time period of the inversion (note the JULES inversion is a shorter time period than the inversions that use the ORCHIDEE prior). For much of the year, posterior results from the ORCHIDEE inversions using gross and net fluxes are very similar, although the gross flux ORCHIDEE inversion in spring (March, April, May) shows slightly stronger extremes. The posterior fluxes from the JULES inversion, on the other hand, show different spatial patterns. Notably, there is a sink over the Alps in spring and autumn (September, October, November), stronger sinks in the Republic of Ireland, central France, north Germany and Italy in spring, a weaker eastern European source in autumn and a small sink in France in winter (December, January, February). These differences broadly reflect the differences between the prior spatial distribution of ORCHIDEE and JULES fluxes (Fig. 4.6) suggesting that the inversions have not been able to spatially redistribute the fluxes to arrive at a common configuration.

However, in summer (June, July, August), the inversions using gross fluxes from ORCHIDEE and JULES do show spatial similarities, albeit with stronger extremes in the JULES inversion, and a stronger source estimated over Spain in the ORCHIDEE inversion. Areas of small sink to net zero fluxes in the ORCHIDEE inversion tend to be areas of small source in the JULES inversion. The ORCHIDEE net flux inversion results for summer are more evenly distributed over the continent, however they also see the same strong source in Spain as the ORCHIDEE gross flux inversion

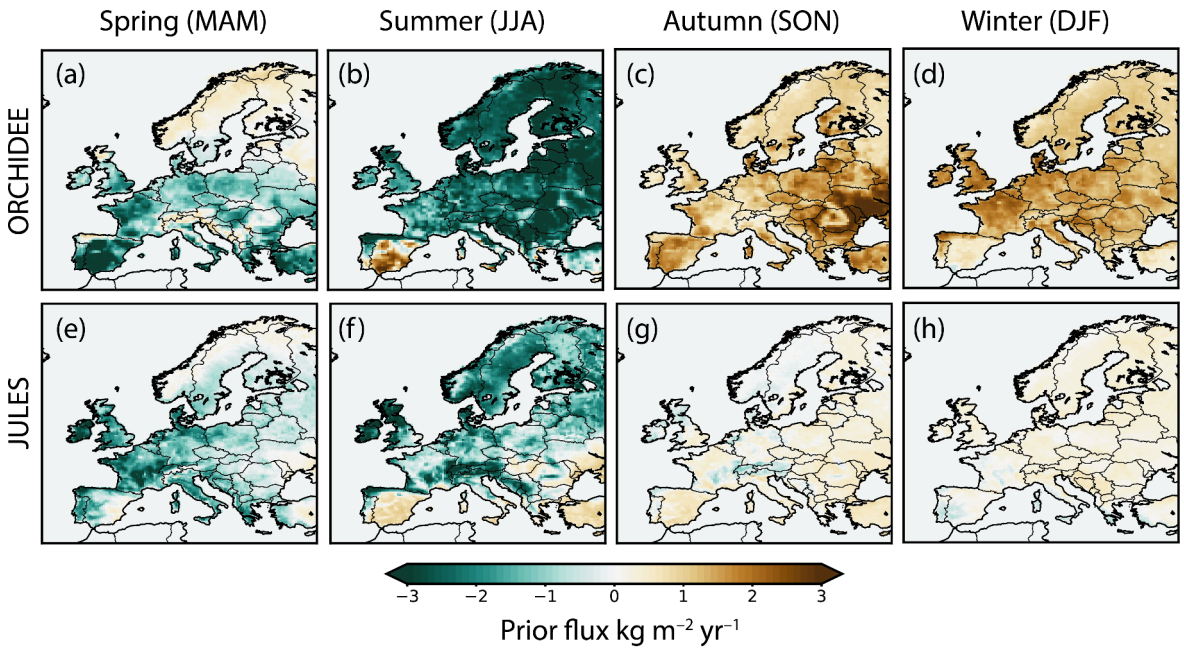

Fig. 4.6: Prior fluxes averaged over the period of the inversion for each season (2011–2015 for ORCHIDEE, 2013–2014 for JULES).

estimates. Therefore, in some circumstances it must be possible for this system to change the spatial distribution of fluxes.

The ORCHIDEE net flux inversion has relatively smooth scaling factors across Europe (Fig. 4.8) owing to the fact that there are fewer degrees of freedom scaling only the NEE. All areas are scaled down. The comparative heterogeneity of the ORCHIDEE gross flux and JULES inversions is therefore due to the competing positive and negative processes. The ORCHIDEE gross flux inversion has mostly scaled down the prior fluxes, like the ORCHIDEE net flux inversion, with the exception of areas of Scandinavia in spring and autumn and some areas of south/central Europe. The JULES inversion scaling is much more heterogeneous. In spring, fluxes are mostly scaled down except in central Europe and Scandinavia. In summer, central and east Europe are scaled up whereas everywhere else is scaled down. In autumn, most fluxes are scaled up from the prior except in some areas of Scandinavia. Finally in winter, most areas have been scaled up except for Portugal, southern Spain, the United Kingdom and the Republic of Ireland. In particular, there is a large area of increased fluxes in central/eastern Europe compared to the prior.

4.3.2 European scale fluxes

The "European scale" in this context is all of the land in the sub-domain (see Fig. 4.2) apart from North Africa. Figure 4.9 shows the monthly European fluxes for each of the three inversions. The posterior estimates are mostly in agreement within the estimated 90 percentile confidence interval; The

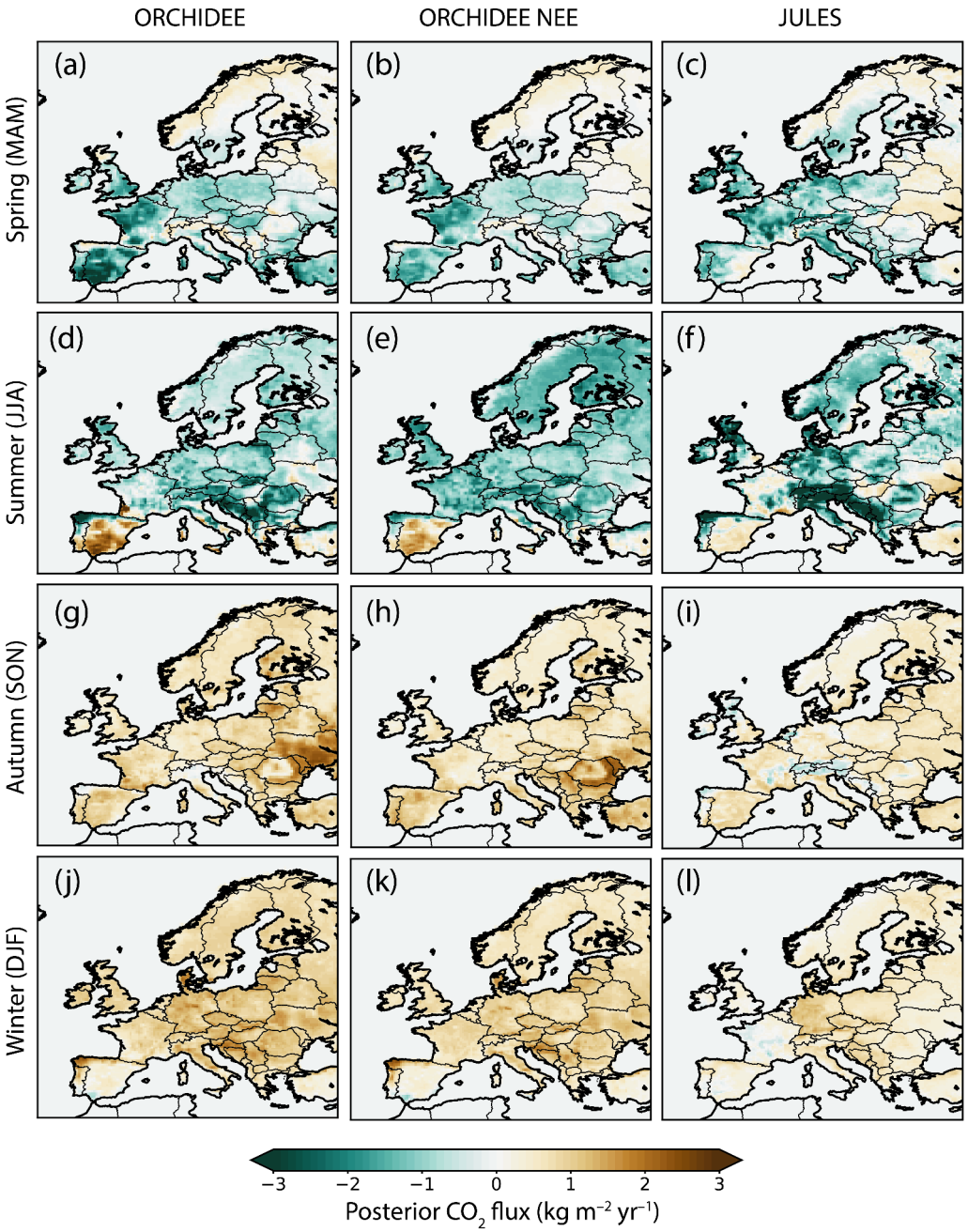

Fig. 4.7: Posterior fluxes averaged over the period of the inversion for each season (2011–2015 for ORCHIDEE, 2013–2014 for JULES). "ORCHIDEE" represents the gross flux inversion and "ORCHIDEE NEE" represents the net flux inversion.

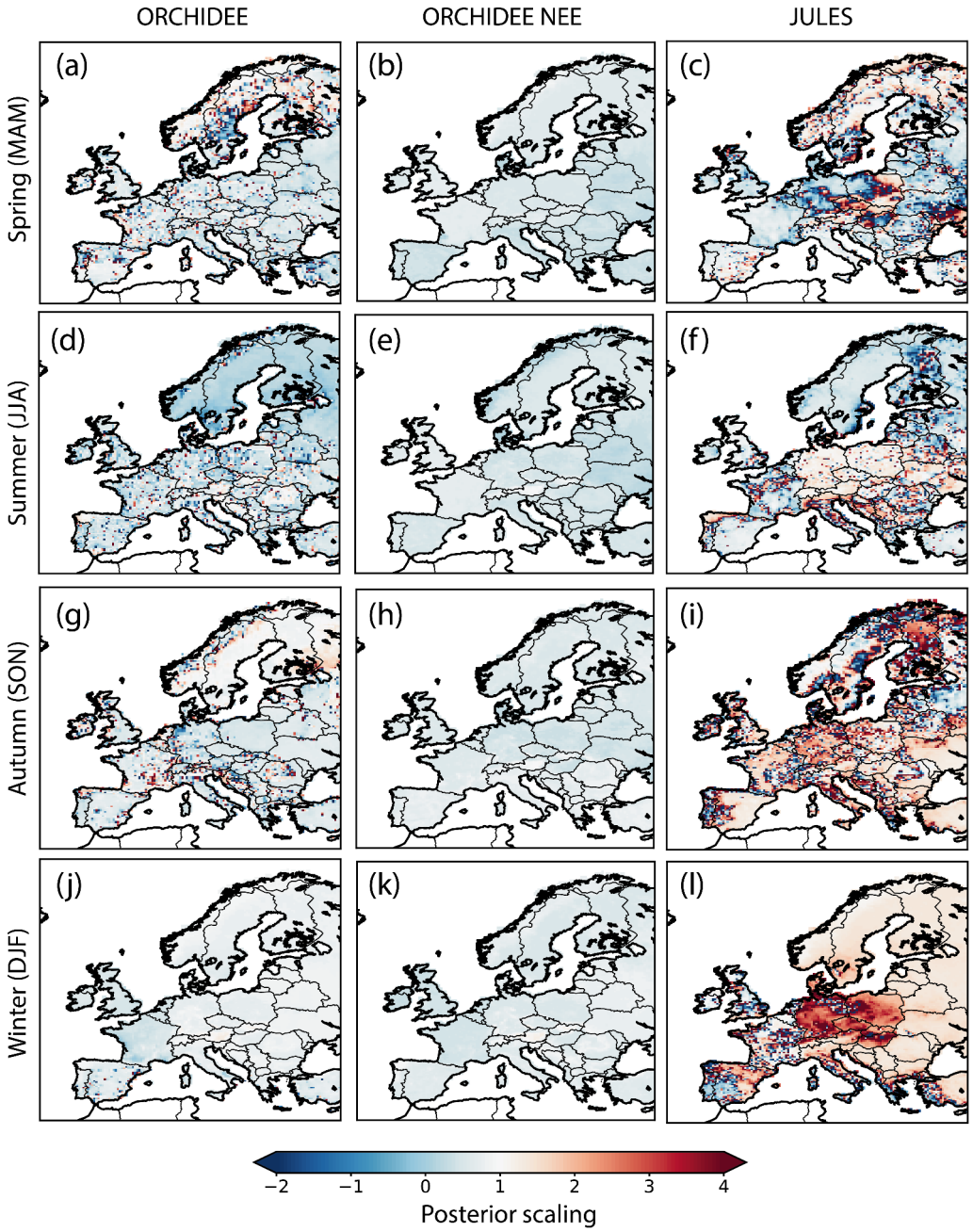

Fig. 4.8: Posterior scaling maps indicating how grid cells have been scaled compared to the prior. Light blue areas are where the fluxes have been scaled down (become a smaller sink or a smaller source) and red areas have been scaled up (become a stronger sink or source). Dark blue areas (numbers below zero) show where the flux has changed sign (a sink becomes a source or vice versa). "ORCHIDEE" represents the gross flux inversion and "ORCHIDEE NEE" represents the net flux inversion.

ORCHIDEE inversions agree in all months and the JULES inversion agrees with both the ORCHIDEE gross and net flux inversions in 20 out of 24 months. Where the JULES inversion doesn't agree with the ORCHIDEE inversions it predicts a smaller source in winter and a smaller sink in summer in 2014. The ORCHIDEE gross flux inversion generally agrees well with the net flux inversion, except in summer 2013 where it estimates a smaller sink of -2775 Tg CO_2 yr^{-1}, averaged over JJA, as opposed to -6579 Tg CO_2 yr^{-1} for the ORCHIDEE net flux inversion. This is in contrast to the findings of Chapter 3, where the gross and net flux inversions gave very different results, and will be discussed further in Section 4.4.3. In relation to prior fluxes, the ORCHIDEE inversions estimate a much reduced maximum summer sink, with the greatest reduction in June 2013 where the ORCHIDEE gross flux inversion gives a monthly flux of 13% of the prior flux and the ORCHIDEE net flux inversion is 30% of the prior. Averaging over all summer months the flux is reduced by 8943 Tg CO_2 yr^{-1} in the gross flux inversion and 7363 Tg CO_2 yr^{-1} in the net flux inversion. The autumn and winter source is also somewhat reduced. In autumn the reduction is greatest in 2011 where the posterior flux is 5073 Tg CO_2 yr^{-1} smaller than the prior in the gross flux inversion and 5954 Tg CO_2 yr^{-1} smaller than the prior in the net flux inversion. On average, the posterior winter source is reduced compared to the prior by 2164 Tg CO_2 yr^{-1} in the gross flux inversion and 2747 Tg CO_2 yr^{-1} in the net flux inversion. Meanwhile, April and August fluxes are often similar. Autumn and Winter fluxes from the JULES inversion are generally higher than the prior, by on average 1502 Tg CO_2 yr^{-1} in autumn and 1197 Tg CO_2 yr^{-1} in winter. The JULES prior also seems to over-estimate the spring sink in 2013 by 3046 Tg CO_2 yr^{-1}.

On an annual scale (Fig. 4.10) there is less agreement between the inversions, although within the uncertainties, which are comparatively large, the estimates do agree. The ORCHIDEE gross flux inversion predicts that Europe is a source of biospheric CO_2 and, over the 5 year period of the inversion, estimates an annual biospheric CO_2 source for Europe of 779 ± 1568 Tg CO_2 yr^{-1} (uncertainty is 1σ). The ORCHIDEE net flux inversion predicts Europe to be a smaller source, or a sink in 2011 and 2014, compared to the gross flux inversion leading to a smaller average annual flux of 235 ± 1449 Tg CO_2 yr^{-1}. Annual European fluxes from both inversions are always larger than the prior, by on average 1472 Tg CO_2 yr^{-1} in the gross flux inversion and 928 Tg CO_2 yr^{-1} in the net flux inversion, although prior values do sit within the uncertainties. The JULES inversion estimates that Europe is a sink of biospheric CO_2, although a smaller one than predicted by the JULES prior, giving an average annual flux (over the two years of the inversion) of -485 ± 1068 Tg CO_2 yr^{-1}. Given the uncertainties however, these results are all consistent with a net zero flux from the European terrestrial biosphere.

The relatively large discrepancies in annual values compared to monthly values highlights the sensitivity of the European biospheric CO_2 budget to small changes in monthly estimates. The amplitude of the seasonal cycle is on average 18170 Tg CO_2 yr^{-1} for the ORCHIDEE gross flux inversion, 17708 Tg CO_2 yr^{-1} for the ORCHIDEE net flux inversion and 12338 Tg CO_2 yr^{-1} for the JULES inversion, one to two orders of magnitude larger than the annual estimates. The large

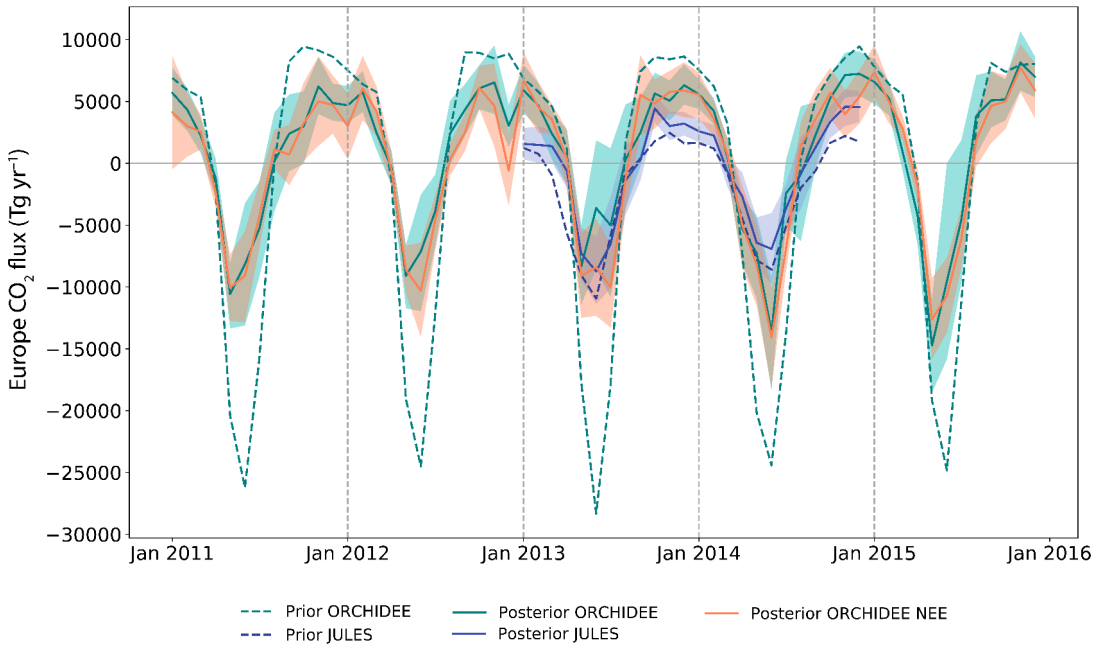

Fig. 4.9: Monthly posterior fluxes from the three inversions (solid lines) compared to the prior (dashed lines). Shaded areas represent the 5–95 percentile range. "Posterior ORCHIDEE" represents the gross flux inversion and "Posterior ORCHIDEE NEE" represents the net flux inversion.

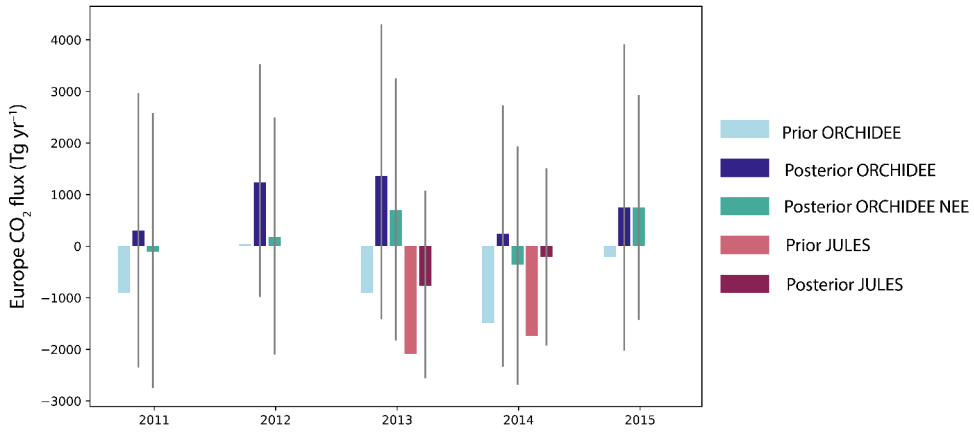

Fig. 4.10: Annual prior and posterior net fluxes (NEE). Uncertainty bars represent the 5–95 percentile range. "Posterior ORCHIDEE" represents the gross flux inversion and "Posterior ORCHIDEE NEE" represents the net flux inversion.

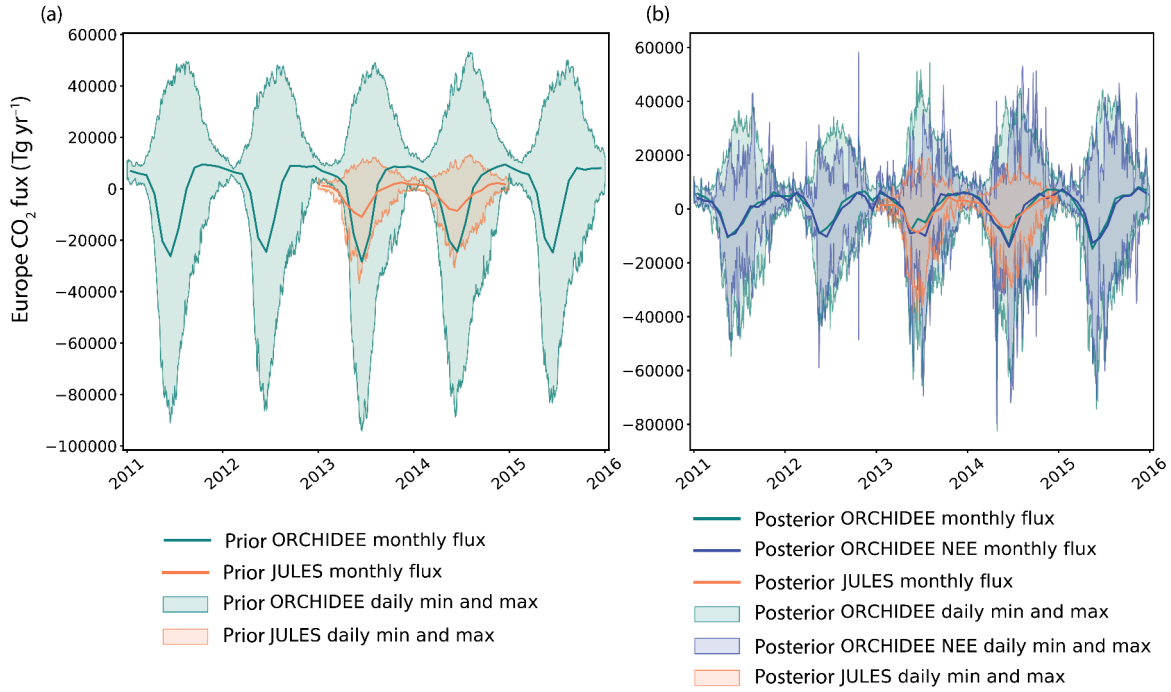

Fig. 4.11: Left: Prior monthly fluxes and diurnal range for ORCHIDEE and JULES. Right: Posterior monthly fluxes and diurnal range for the three inversions using ORCHIDEE gross and net fluxes and JULES gross fluxes. "Posterior ORCHIDEE" represents the gross flux inversion and "Posterior ORCHIDEE NEE" represents the net flux inversion.

uncertainties in fluxes on the European scale is likely due to the inability of the inversion to constrain the fluxes in certain areas where there is limited data. This will be explored in the following sections.

At the diurnal temporal scale, the results of the three inversions are also fairly different (Fig. 4.11b). The ORCHIDEE gross flux inversion has comparatively little day to day variability in diurnal range in contrast to that of the ORCHIDEE net flux inversion, which frequently increases or decreases by an order of magnitude, whilst the monthly results are very similar. The net flux inversion has fewer degrees of freedom, therefore it may have to make some unnecessarily large changes to the diurnal range at certain times to give the desired monthly average flux. The JULES inversion has a much smaller posterior diurnal range than the other two inversions, averaging 2761 Tg CO_2 yr^{-1} in minimum months (January 2013 and December 2014) and 41115 Tg CO_2 yr^{-1} in maximum months (June 2013 and 2014), whereas the diurnal range for the ORCHIDEE gross flux inversion is on average 7348 Tg CO_2 yr^{-1} in minimum months (typically January) and 78514 Tg CO_2 yr^{-1} in maximum months (typically June). However the overall profile is somewhat similar, with a less pronounced seasonal cycle in the daily maximum source. Yet, in comparison to the prior diurnal range for ORCHIDEE and JULES (Fig. 4.11a), the posterior diurnal fluxes are approaching a similar magnitude; the difference between the months of maximum diurnal range in the ORCHIDEE and JULES priors, which is 85624 Tg CO_2 yr^{-1} on average, is reduced to 44% giving an average difference

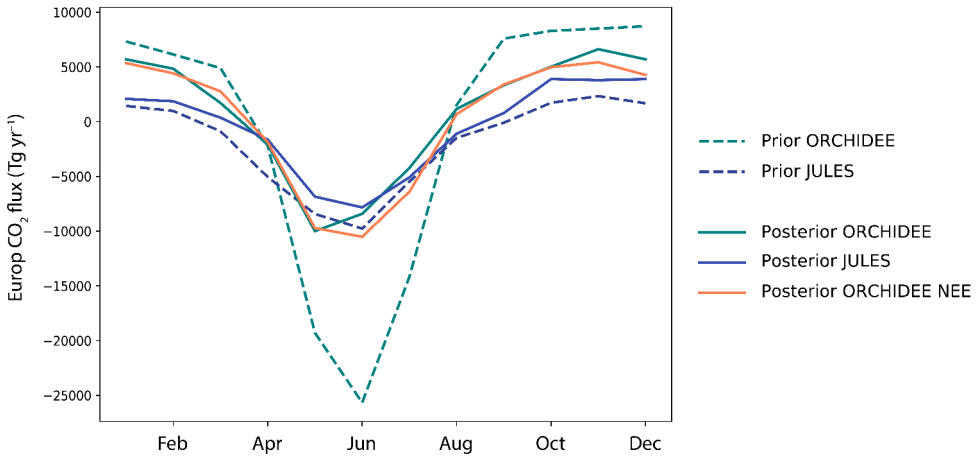

Fig. 4.12: Average seasonal cycle over the period of the inversion (2011–2015 for ORCHIDEE, 2013–2014 for JULES). "Posterior ORCHIDEE" represents the gross flux inversion and "Posterior ORCHIDEE NEE" represents the net flux inversion.

of 37399 Tg CO_2 yr^{-1} between the months of maximum diurnal range in the ORCHIDEE and JULES posteriors. The posterior results are closer to that of the JULES prior in the daily maximum sink and somewhere between the two priors in the daily maximum source.

The average seasonal cycle (Fig. 4.12) highlights the prior/posterior and inter-inversion differences (bear in mind here that the JULES inversion is only averaged over two years whereas the ORCHIDEE inversions are averaged over five years). Again, the ORCHIDEE inversions have a much shallower seasonal cycle than that of the ORCHIDEE prior; the amplitude of the ORCHIDEE prior is 34389 Tg CO_2 yr^{-1} compared to 16622 Tg CO_2 yr^{-1} in the gross flux inversion and 15943 Tg CO_2 yr^{-1} in the net flux inversion. This is closer to the amplitude of the JULES prior seasonal cycle, 12107 Tg CO_2 yr^{-1}, and the amplitude of the JULES posterior seasonal cycle is 11721 Tg CO_2 yr^{-1}. However, posterior autumn and winter fluxes fall between the two priors and the JULES prior overestimates uptake in spring by 2077 Tg CO_2 yr^{-1}. The main differences between the gross and net flux ORCHIDEE inversions are clearer here and show that despite many similarities, the posterior results from the gross flux inversion indicate a smaller sink in June and July.

4.3.3 Regional scale fluxes

Six regions have been identified as part of the EUROCOM project in order to assess fluxes on smaller spatial scales. These are described in Fig. 4.2. Figure 4.13 shows the monthly fluxes in each of the six regions and the annual total fluxes for each region can be found in Fig. 4.14.

At a first glance, it is possible to see that between the regional results there is a lot of variation in uncertainty estimates and level of agreement between the three inversions. Western and central Europe are the most well constrained, with 90 percentile confidence intervals of around 600 Tg CO_2 yr^{-1} and 900 Tg CO_2 yr^{-1} respectively, whereas fluxes in south-eastern and eastern Europe have

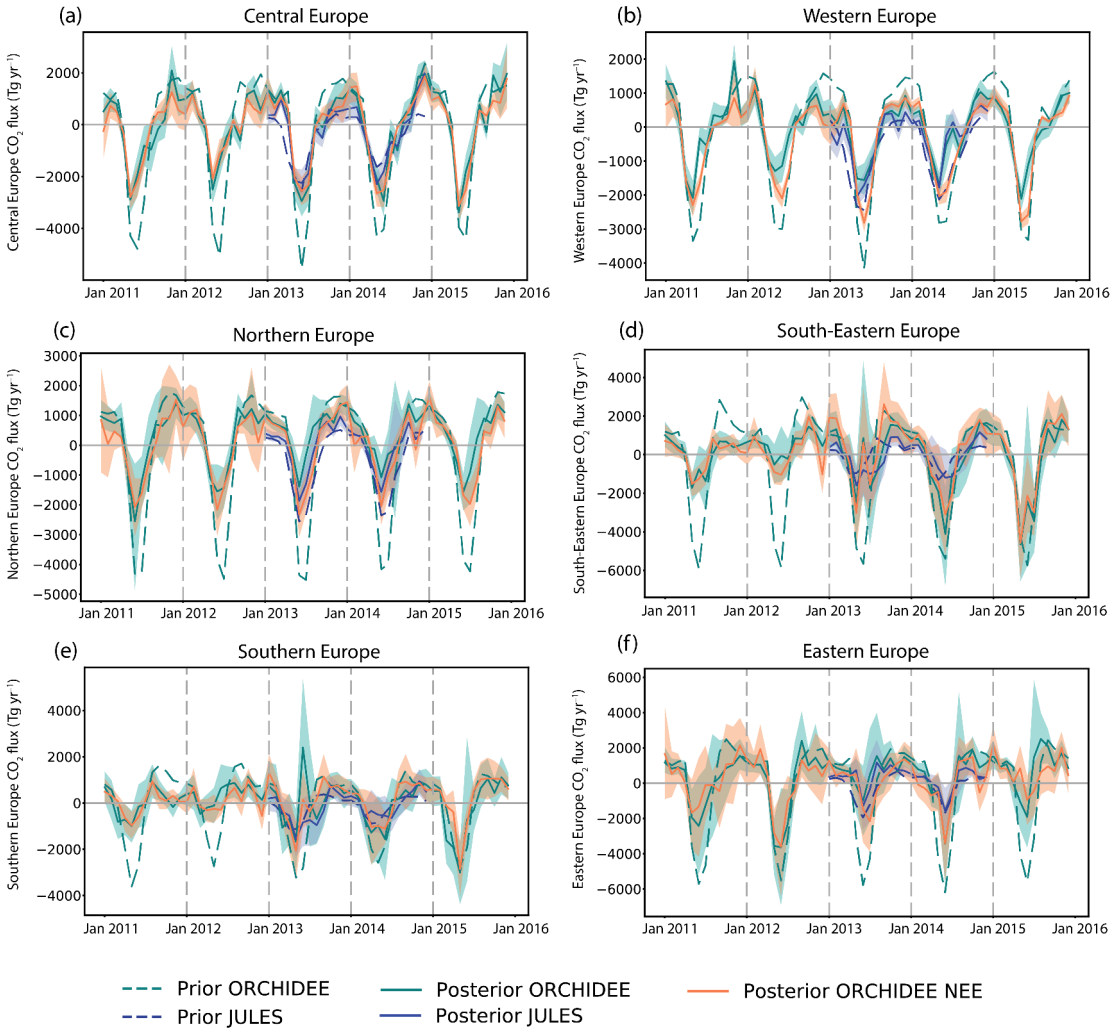

Fig. 4.13: Monthly prior and posterior fluxes for each of six regions over the EUROCOM area. Shading represents 5–95 percentile range. "Posterior ORCHIDEE" represents the gross flux inversion and "Posterior ORCHIDEE NEE" represents the net flux inversion.

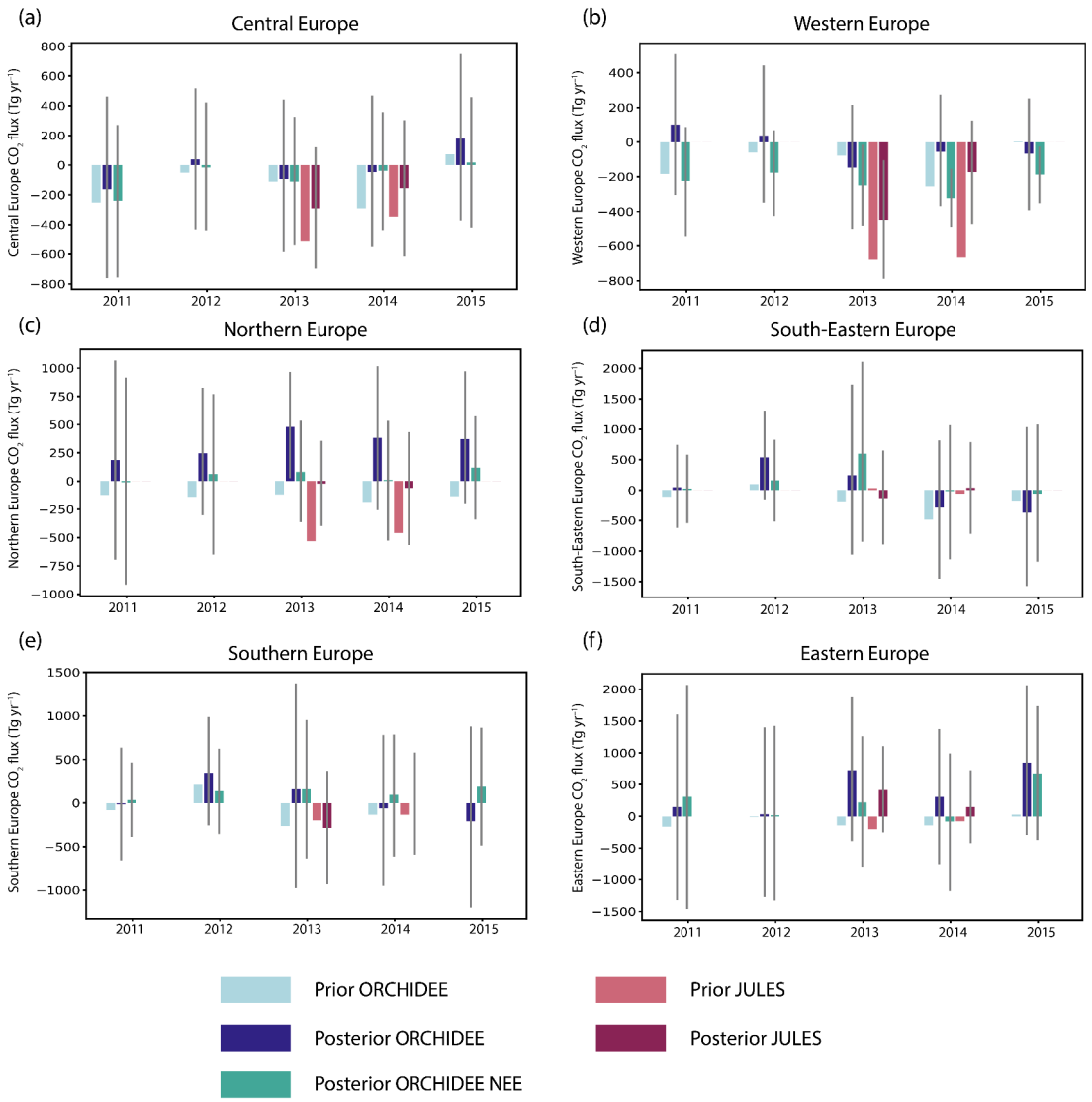

Fig. 4.14: Annual prior and posterior fluxes for each of six regions over the EUROCOM area. Uncertainty bars represent 5–95 percentile range. "Posterior ORCHIDEE" represents the gross flux inversion and "Posterior ORCHIDEE NEE" represents the net flux inversion.

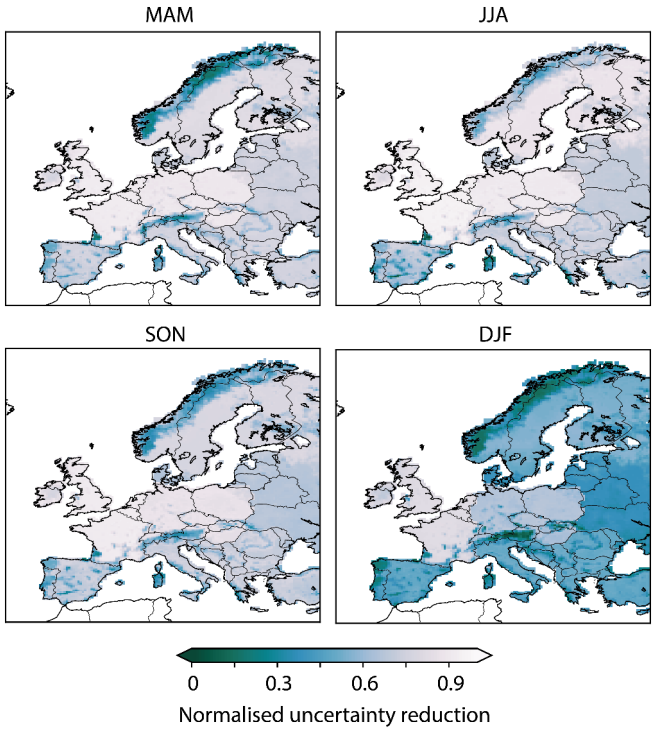

Fig. 4.15: Normalised uncertainty reduction over EUROCOM subdomain for the ORCHIDEE inversion. Uncertainty reduction is defined in Eq. 4.1

comparatively large uncertainties, with 90 percentile confidence intervals of around 1900 Tg CO_2 yr^{-1} and 2100 Tg CO_2 yr^{-1} respectively. This reflects the distribution of atmospheric measurement stations used in this study, where all bar three of the stations are in central and western Europe (see Fig. 4.2). A further two are in northern Europe and one in southern Europe. The uncertainty reduction in the ORCHIDEE inversion is shown in Fig. 4.15 and is defined as follows:

$$Uncertainty\ reduction = 1 - \left(\frac{90\%ile\ range_{posterior}}{90\%ile\ range_{prior}} \right) \tag{4.1}$$

Figure 4.15 confirms that the largest reduction is in central and western Europe and appears to show that there has been a large uncertainty reduction everywhere with the winter fluxes seeing the least improvement. However, prior uncertainties are large, especially in summer months because they scale with the size of the fluxes, so lilac colours may still signify large uncertainties.

In central Europe, the monthly fluxes of all three inversions, shown in Fig. 4.13a, are in good agreement within the estimated uncertainties; the ORCHIDEE inversions agree in 58 out of 60 months and the JULES inversion agrees with the ORCHIDEE gross and net flux inversions in 23 and 22 out of 24 months respectively. Annual estimates, Fig. 4.14a always agree on the sign of the net flux and the means of the two ORCHIDEE inversions mostly agree very well, within 80 Tg CO_2 yr^{-1}, except in 2015. All annual estimates agree within the estimated uncertainties.

Western Europe is the only region where a consistent discrepancy can be seen between the ORCHIDEE gross and net flux inversions (Fig. 4.13b). This occurs around summer in all years and patterns in the gross flux inversion somewhat resemble those seen in the inversion results in Chapter 3. The JULES inversion agrees with the ORCHIDEE gross flux inversion in all months within the estimated 90 percentile range, whereas there is only agreement with the ORCHIDEE net flux inversion in 16 out of 24 months. The annual fluxes (Fig. 4.14b) show a large difference between ORCHIDEE gross and net flux inversions, where the net flux inversion estimates a sink of -232 Tg CO_2 yr^{-1} on average (range is -324- -177 Tg CO_2 yr^{-1}) and the gross flux inversion estimates a larger net flux of -26 Tg CO_2 yr^{-1} on average (range is -148 - 101 Tg CO_2 yr^{-1}). JULES inversion annual fluxes are a larger sink than the ORCHIDEE net flux inversion in 2013 and fall between the ORCHIDEE gross and net flux inversion estimates in 2014. The disagreement of the JULES inversion to either of the ORCHIDEE inversions is largely due to smaller winter fluxes.

Monthly fluxes in the other regions have larger uncertainties. In northern Europe (Fig. 4.13c) the fluxes agree in most months, however there is a discrepancy as large as a factor of 1.9 over the maximum summer uptake. In southern, eastern and south-eastern Europe the monthly fluxes are much more variable compared to the other regions and the seasonal cycle is harder to identify, particularly in 2011 and 2012 in south and south-eastern Europe. Annual fluxes for these regions show a variety of estimates from all three inversions with no clear pattern. Annual fluxes from the JULES inversion estimate a net sink everywhere, except in eastern Europe where it estimates a net source. This is consistent with the posterior gridded fluxes in Fig. 4.7 that show the main source of increased winter fluxes is over central/eastern Europe.

4.3.4 Model-data comparison

Table 4.2 gives an overview of how well each of the inversions is able to fit the observed data. According to these statistics, the ORCHIDEE gross flux inversion gives the best fit to the data across all sites. The JULES and ORCHIDEE NEE inversions have a very similar R^2 fit across all sites however the JULES inversion has a better fit to the data in terms of RMSE. Mean bias statistics are similar across all three inversions. The JULES inversion generally fits data slightly better at sites in north west Europe, whereas the ORCHIDEE gross flux inversion fits the data best at sites everywhere else.

To give some illustration of Table 4.2, observations and prior and posterior modelled mole fractions are shown in Figures 4.16 and 4.17 for the ORCHIDEE gross flux and the JULES inversions at three measurement sites, Pallas (PAL), Heidelberg (HEI) and Mace Head (MHD). Using an R^2 statistical comparison, the ORCHIDEE inversion has the best prior and posterior fit to the data at PAL and HEI and the JULES inversion has a better fit to the data at MHD. Prior ORCHIDEE modelled mole fractions tend to under-estimate concentrations in late spring and early summer as a result of over-estimated uptake in these months. These are corrected during the inversion and lead to the smaller summer uptake seen in the monthly fluxes. This also occurs to a lesser extent in the JULES

Table 4.2: Fit to the data statistics for the three inversions averaged over the period of the inversion (2011–2015 for ORCHIDEE, 2013–2014 for JULES). Grey shading highlights the sites for which mole fractions and residual histograms are plotted in Figs. 4.16, 4.17 and 4.18. "ORCHIDEE" represents the gross flux inversion and "ORCHIDEE NEE" represents the net flux inversion.

JULES						
Site	**Prior R^2**	**Post R^2**	**Prior RMSE**	**Post RMSE**	**Prior Bias**	**Post Bias**
MHD	0.22	0.65	1.55	1.13	0.59	0.45
PAL	0.33	0.74	2.88	1.49	2.63	0.22
SMR	0.20	0.66	2.92	1.80	1.08	-0.48
OPE	0.18	0.56	3.85	3.03	0.46	-1.34
HEI	0.17	0.46	6.55	4.91	2.75	0.94
HUN	0.23	0.64	5.07	3.31	0.64	-2.01
RGL	0.31	0.72	2.80	1.84	0.79	-1.00
TRN	0.19	0.49	4.46	3.68	1.17	-0.01
TAC	0.25	0.63	2.89	2.10	0.53	-0.15
TTA	0.29	0.61	2.33	1.71	1.52	-0.67
SSL	0.28	0.57	4.07	3.34	-0.22	-3.12
CBW	0.24	0.50	3.92	3.27	0.51	-0.70
LUT	0.26	0.57	4.17	3.17	2.90	1.98
All sites	0.23	0.55	4.07	3.07	1.05	0.06
ORCHIDEE						
Site	**Prior R^2**	**Post R^2**	**Prior RMSE**	**Post RMSE**	**Prior Bias**	**Post Bias**
MHD	0.19	0.63	1.72	1.07	0.72	0.21
PAL	0.45	0.81	3.35	1.15	3.85	-0.10
SMR	0.28	0.77	3.75	1.56	0.94	-0.45
OPE	0.25	0.67	4.76	2.55	1.16	-1.41
HEI	0.23	0.51	6.36	4.52	2.56	0.78
HUN	0.27	0.73	5.23	2.76	1.03	-1.90
RGL	0.33	0.69	3.19	1.82	0.54	-1.27
TRN	0.27	0.61	4.37	2.98	0.70	-1.04
TAC	0.33	0.70	3.05	1.79	0.45	-0.61
KAS	0.18	0.53	7.18	3.55	-1.09	-3.63
TTA	0.26	0.58	2.60	1.44	0.82	-0.84
LMP	0.22	0.44	3.48	2.00	0.22	-0.14
SSL	0.25	0.55	4.78	3.15	-0.13	-2.96
CBW	0.29	0.53	4.47	3.38	-0.07	-0.75
LUT	0.33	0.52	4.38	3.48	1.63	1.37
All sites	0.29	0.61	4.55	2.95	0.88	-0.04
ORCHIDEE NEE						
Site	**Prior R^2**	**Post R^2**	**Prior RMSE**	**Post RMSE**	**Prior Bias**	**Post Bias**
MHD	0.19	0.59	1.58	0.99	0.40	0.29
PAL	0.45	0.75	3.19	1.49	3.31	-0.13
SMR	0.28	0.72	3.57	1.85	0.54	-0.49
OPE	0.25	0.57	4.47	2.97	0.71	-1.42
HEI	0.23	0.48	6.03	4.79	2.03	0.81
HUN	0.27	0.66	4.96	3.24	0.52	-1.88
RGL	0.33	0.65	3.00	1.96	0.14	-1.31
TRN	0.27	0.55	4.21	3.23	0.32	-1.01
TAC	0.33	0.65	2.88	1.93	0.04	-0.65
KAS	0.18	0.59	7.22	3.35	-1.72	-3.66
TTA	0.26	0.55	2.42	1.50	0.38	-0.86
LMP	0.22	0.46	3.22	1.81	-0.09	0.46
SSL	0.25	0.52	4.66	3.31	-0.60	-2.94
CBW	0.29	0.50	4.35	3.51	-0.62	-0.74
LUT	0.33	0.50	4.15	3.59	1.29	1.42
All sites	0.29	0.56	4.38	3.14	0.44	-0.05

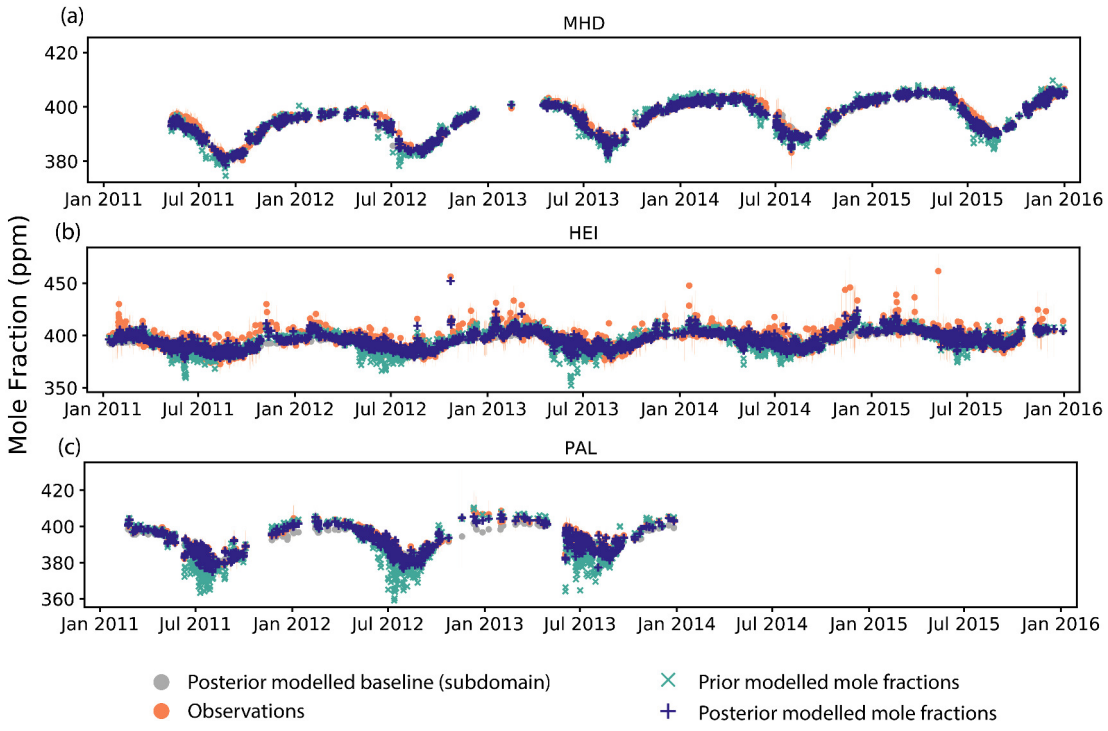

Fig. 4.16: Mole fractions from the ORCHIDEE gross flux inversion at Mace Head (MHD), Heidelberg (HEI) and Pallas (PAL).

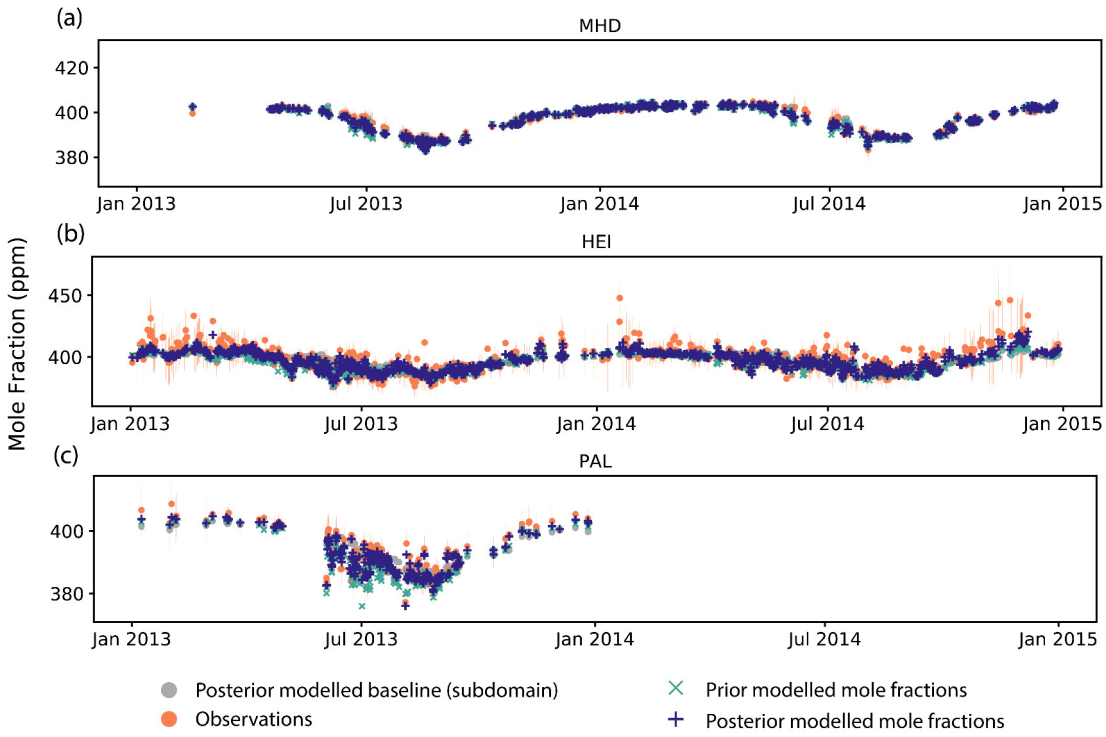

Fig. 4.17: Mole fractions from the JULES inversion at Mace Head (MHD), Heidelberg (HEI) and Pallas (PAL).

prior modelled mole fractions for PAL (Fig. 4.17c). In both inversions, the majority of the higher mole fractions seen at HEI have not been represented (Figs. 4.16b and4.17b) and unsurprisingly HEI has the worst fit to the data of these three sites for both inversions.

Figure 4.18 shows histograms of residual prior and posterior modelled mole fractions for the same three sites and for all three inversions. Prior modelled mole fractions at PAL stand out as being frequently under-estimated using both ORCHIDEE and JULES priors but this is corrected in the posterior modelled mole fractions, which gives it the smallest posterior bias of the inversions at these three sites of –0.1 to 0.22 ppm. The bias at HEI, on the other hand, is between 0.78 and 0.94 ppm.

4.4 Discussion

4.4.1 The system's ability to estimate European scale fluxes

Estimates for the European biospheric CO_2 budget from this work are all in agreement within the estimated uncertainties and mean results range from a small net source of 779±1568 Tg CO_2 yr^{-1} (ORCHIDEE gross flux inversion, uncertainty is 1σ) to a small net sink of –485±1068 Tg CO_2 yr^{-1} (JULES inversion). However, with the uncertainties straddling zero, these results are all consistent with a biosphere in balance, where sources equal sinks. The fit to the data is generally good and the ORCHIDEE gross flux inversion is able to best fit the observations. The fit of the JULES and

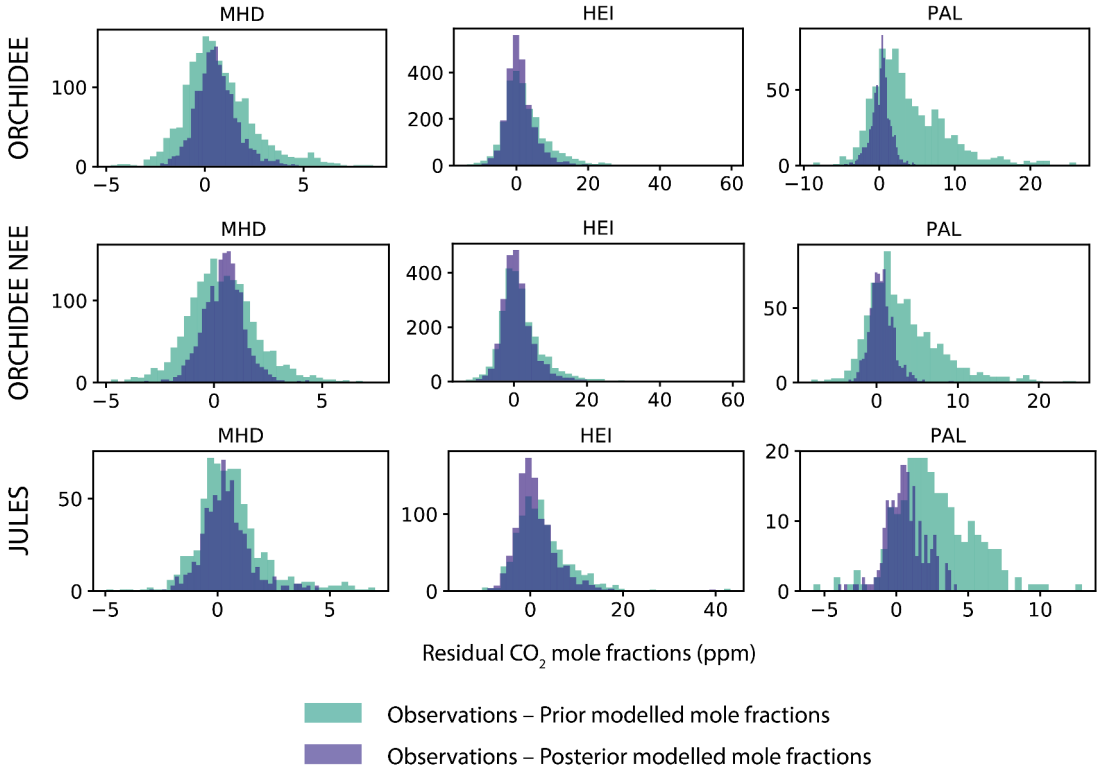

Fig. 4.18: Residual mole fraction histograms for all three inversions at Mace Head (MHD), Heidelberg (HEI) and Pallas (PAL). "ORCHIDEE" represents the gross flux inversion and "ORCHIDEE NEE" represents the net flux inversion.

ORCHIDEE net flux inversions are not significantly worse, consistent with the fact that the posterior estimates agree across all three inversions.

The uncertainties in the results presented here are large; the one standard deviation uncertainty on the annual European flux is typically 200 - 600 % of the flux itself. Analysis of regional fluxes reveals that this system is able to best constrain fluxes from western and central Europe, which is mostly due to the comparative density of measurement sites in these areas. Therefore, the European budget itself is not well constrained and highlights the need to include measurements from sites that can represent fluxes in poorly constrained areas. Such sites could include Monte Cimone in Italy, La Muela in Spain, Bialystock in Poland, Norunda in Sweden and Birkenes in Norway. One problem is that the dates and times that data are available do not always overlap in a way such that there is always a good spatial distribution of measurement data, so extending the time period of the inversion to maximise the chances of finding a good distribution of sites in any one month may help. There is also a need to continue measurements from existing sites and develop new long standing measurement sites, particularly in areas of southern, south-eastern and eastern Europe.

4.4.2 Differences between prior and posterior NEE flux estimates

Compared to prior ORCHIDEE and JULES fluxes, the posterior Europe, and some regional, totals from all inversions resemble each other very closely. According to these results, the ORCHIDEE prior strongly over-estimates the summer sink and slightly over-estimates the winter source, however the timing of the seasonal cycle is generally well modelled (except for western Europe). On the other hand, the JULES prior under-estimates the winter source of CO_2 and spring uptake is too early in 2013. This leads to posterior results with a much weaker seasonal cycle than that predicted by the ORCHIDEE prior and improved timing of the seasonal cycle as compared to JULES.

4.4.3 Gross vs. net flux inversions

In general, the gross and net flux inversions do follow the results of Chapter 3 in that the mean annual total from the gross inversion is slightly higher than the mean annual total from the net inversion, however they are in much better agreement here than in previous work. This could be due to the inclusion of disturbance fluxes in the ORCHIDEE prior, giving a better profile of diurnal net fluxes with the spring vegetation growth and autumn die-back occurring at the appropriate time, even if the magnitudes are too large (because uptake has been scaled down a lot in the inversion). The average seasonal cycle over Europe also indicates that the ORCHIDEE gross flux inversion finds a reduced summer sink in June and July, as found in Chapter 3. However the difference is small, perhaps indicating that there is not much to be gained from separately scaling the gross fluxes in the inversion. The JULES inversion gives mean annual total results that are slightly smaller than both of the ORCHIDEE inversions (1264 Tg CO_2 yr^{-1} smaller than the ORCHIDEE gross flux inversion and 720 Tg CO_2 yr^{-1} smaller than the ORCHIDEE net flux inversion), but within the uncertainties there is agreement on an annual scale between all of the inversions.

On the monthly scale, the three inversions tend to agree well over Europe as a whole and over the central Europe region, however in western Europe both gross flux inversions show a similarly reduced summer sink in all years of the study, by on average around 900 Tg CO_2 yr^{-1}. This was also seen in the work of Chapter 3 and it was thought that additional summer fluxes could be coming from harvest disturbance. There are two contributing elements here. Firstly, there is the difference between how the gross and net fluxes are dealt with in the inversion. Secondly, there is the fact that the ORCHIDEE prior should take into account fluxes from human disturbance, such as harvest. Both JULES and ORCHIDEE gross flux inversion posteriors in western Europe are larger than the ORCHIDEE net flux inversion posterior in June and July indicating that this is a signal that cannot be replicated by the ORCHIDEE net flux inversion. However, this is also a signal that is not seen in the ORCHIDEE prior, which either suggests that the ORCHIDEE prior is wrongly estimating disturbance fluxes or still omitting some element of disturbance, or that the higher summer fluxes are not due to disturbance. The fact that this is only seen in western Europe monthly fluxes and not elsewhere could be due to higher levels of disturbance in western Europe, or a denser network of sites in this region that is better able to resolve changes to the prior seasonal cycle.

On the diurnal scale, the profiles of European fluxes for the three inversions have converged somewhat on a similar result, resembling each other more closely than the prior diurnal profiles. For example the ratio of the average diurnal range for June between the JULES and ORCHIDEE posteriors is reduced by over 40% from 3.3 to 1.9. A more realistic profile is achieved with the gross flux inversions as there are less occurrences of large day-to-day variability in the diurnal range compared to the net flux inversion, indicating that fluxes at this temporal scale are best resolved by separating the gross fluxes. The main discrepancy between the JULES and ORCHIDEE posteriors is in the daily maximum source.

4.4.4 European biospheric CO_2 estimates in the context of previous studies

In the context of the previous studies discussed in Section 4.1, the results of this work are on the upper end of estimates for the European biospheric CO_2 budget, shown in Fig. 4.19. Mean estimates all lie within the results of Peters et al. (2010), which is also a regional inversion study using in-situ measurements and the 1σ range of the results presented here is also comparable to that of many of the studies. A major difference between the results presented here and the previous studies is the time period of the analysis. As discussed in Section 4.1, inter-annual variability can play a major role in the European biospheric CO_2 budget, so differences in these results could be reflecting this.

4.5 Conclusions and future work

This chapter has taken the method developed in Chapter 2 and investigated its suitability for biospheric CO_2 flux estimation over a larger region (Europe) with more data. The results from three different inversions (gross and net flux inversions using prior biospheric fluxes from ORCHIDEE and a gross

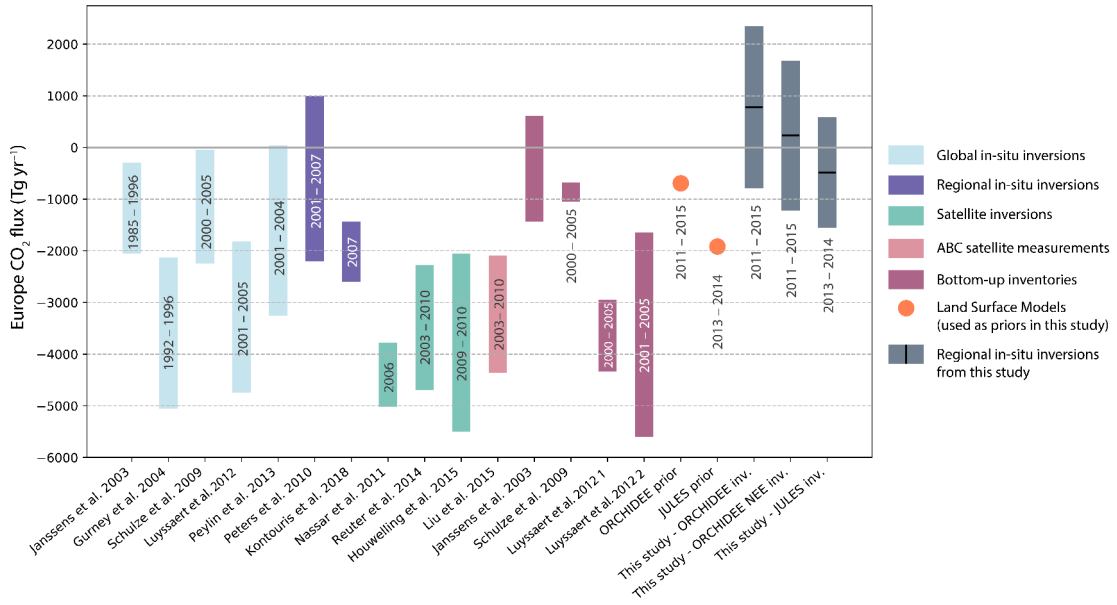

Fig. 4.19: The results of this study (grey bars showing 1σ uncertainty and black line showing mean) along with estimates of European biospheric CO_2 budget from previous studies. The majority of uncertainty estimates from the previous studies are 1σ, however it is sometimes difficult to calculate comparable uncertainty estimates.

flux inversion using prior biospheric fluxes from JULES) give a spread of results ranging from a small net source to a small net sink, however they all agree within their estimated uncertainties. European biospheric CO_2 fluxes are found to be 779 ± 1568 Tg CO_2 yr^{-1} (uncertainty is 1σ) with the ORCHIDEE gross flux inversion and 235 ± 1449 Tg CO_2 yr^{-1} with the ORCHIDEE net flux inversion over 2011–2015. The JULES inversion estimated European biospheric CO_2 fluxes of -485 ± 1068 Tg CO_2 yr^{-1} over 2013–2014. These results are consistent with a net zero CO_2 flux from the biosphere over Europe and fit within the context of previous estimates for Europe's biospheric CO_2 budget, albeit at the upper end of estimates.

The areas best constrained in this work are western and central Europe, owing to the comparative density of measurement sites in these regions. To improve overall Europe estimates, future work should incorporate available data from more sites and more measurement sites are needed in southern, south-eastern and eastern Europe. Also, the time period of the study should be extended (at least from 2006–2015) to allow additional data that has been collected between 2006–2011 to be included.

This study has revealed some interesting developments to the conclusions made in Chapters 2 and 3. Mostly, only a small difference is seen between the gross and net flux inversions except over western Europe where the density of measurements is greatest. This could mean that the gross flux inversion is only able to add additional information where there are enough measurements. However, since the ORCHIDEE prior biospheric fluxes include information about human disturbances such as harvest, it may be that this additional information is what is required to improve net flux inversions and the differences seen in western Europe could be due to poor estimation of disturbance or natural

biospheric fluxes in this area from ORCHIDEE. Monthly fluxes from the JULES inversion agree well with the ORCHIDEE inversions and agree with the ORCHIDEE gross flux inversion in western Europe, which indicates that using a prior with no disturbance does not necessarily affect the posterior results when using a gross flux inversion. A synthesis of the results from this chapter and Chapter 3 follows in Chapter 5 and investigates some remaining questions.

Chapter 5

Synthesising the results of UK and European CO_2 flux studies

5.1 Introduction

This synthesis chapter serves to bring together the results from Chapters 3 and 4. Both chapters use the method developed in Chapter 2. However, Chapter 3 presents the results of a study focussed on the UK, using a dense network of sites in and around the UK, and Chapter 4 is focussed on Europe, using a different network of sites with fewer in the UK, and a different prior flux model. In this chapter, the results of both studies will be compared, using a common flux area over the UK only, to evaluate whether they are consistent.

The main differences between the set-ups used in Chapters 3 and 4 are set out in Table 5.1. Chapter 3 concluded that the prior fluxes over-estimated the summer sink, possibly because they were missing biospheric CO_2 fluxes linked to human disturbance. In addition, carrying out the inversion with gross fluxes gave a consistent picture between two inversions with different priors, whereas using net fluxes in the inversion did not. This supported the results of a synthetic test in Chapter 2, where a gross flux inversion was able to find the "true" fluxes and a net flux inversion was not. The main conclusions from Chapter 4 were that on a European scale, the set-up used was best able to constrain fluxes in western and central Europe. There was less difference seen between ORCHIDEE gross and net flux inversions, possibly because ORCHIDEE includes disturbance fluxes, except in western Europe. It was speculated that the difference in western Europe could be due to poor estimation of disturbance or natural biospheric fluxes in these areas in ORCHIDEE compared to other parts of Europe. Alternatively, a denser network of measurement sites in this area may be able to better resolve detailed changes to the seasonal cycle, implying that ORCHIDEE could also be poorly estimating disturbance or natural biospheric fluxes elsewhere but this cannot be resolved using the data available.

Table 5.1: Distinguishing features of the inversion set-ups used in Chapters 3 and 4. Measurement sites "near" the UK are included as they are likely to provide some constraint on UK fluxes.

	Sites in UK	Sites near UK	Priors	Basis functions	Temporal resolution of data in inversion
Chapter 4	Ridge Hill (RGL) Tacolneston (TAC) Heathfield (HFD) Bilsdale (BSD) Angus (TTA)	Mace Head (MHD)	CARDAMOM gross flux CARDAMOM net flux JULES gross flux JULES net flux	PFTs over subdomain	2-hourly
Chapter 5	Ridge Hill (RGL) Tacolneston (TAC) Angus (TTA)	Mace Head (MHD) Cabauw (CBW) Lutjewad (LUT) Trainou (TRN)	ORCHIDEE gross ORCHIDEE net JULES gross	PFTs over west Europe	6-hourly

5.2 UK CO_2 fluxes using UK and European networks

5.2.1 Seasonal cycle

Figure 5.1 shows the monthly fluxes over the UK from gross and net flux inversions from Chapters 3 and 4. The Chapter 4 results over the UK are similar to those seen over the western Europe region, in that the ORCHIDEE net flux inversion has lower fluxes in June and July than the gross flux inversion. Whilst the JULES inversion does not agree with the ORCHIDEE gross flux inversion as closely as it does over the western Europe region (the inversions are in agreement in all months over the western Europe region and just 15 out of 24 months over the UK region), it does show similarities e.g. where the gross flux inversions both indicate that fluxes reduce between July and August 2014 whereas the net flux inversion has a steady increase of fluxes in the second half of the year.

Comparing the results across the two studies, there are similarities between the seasonal cycles of gross flux inversions. Both studies see an abrupt increase in fluxes between June and July 2014 and a decrease or much shallower increase between July and September 2014. The main differences are that uptake in May, June and July 2013 range between –565 and –381 Tg CO_2 yr^{-1} and in Chapter 3 the maximum uptake in 2014 is in June whereas in Chapter 4 it is in May. The July "peak" in 2014 ranges between around –120 and 180 Tg CO_2 yr^{-1} in the results from both chapters. However, within the estimated uncertainties the four gross flux inversions often all agree within the estimated 90 percentile ranges (in 12 out of 24 months) and, importantly, the JULES inversions from Chapter 3 and 4 both agree within the estimated 90 percentile confidence interval in all months except January and May 2014.

Despite overestimating the winter source and the maximum summer sink, the timing of the seasonal cycle in the ORCHIDEE prior is in best agreement with that of the gross flux inversions.

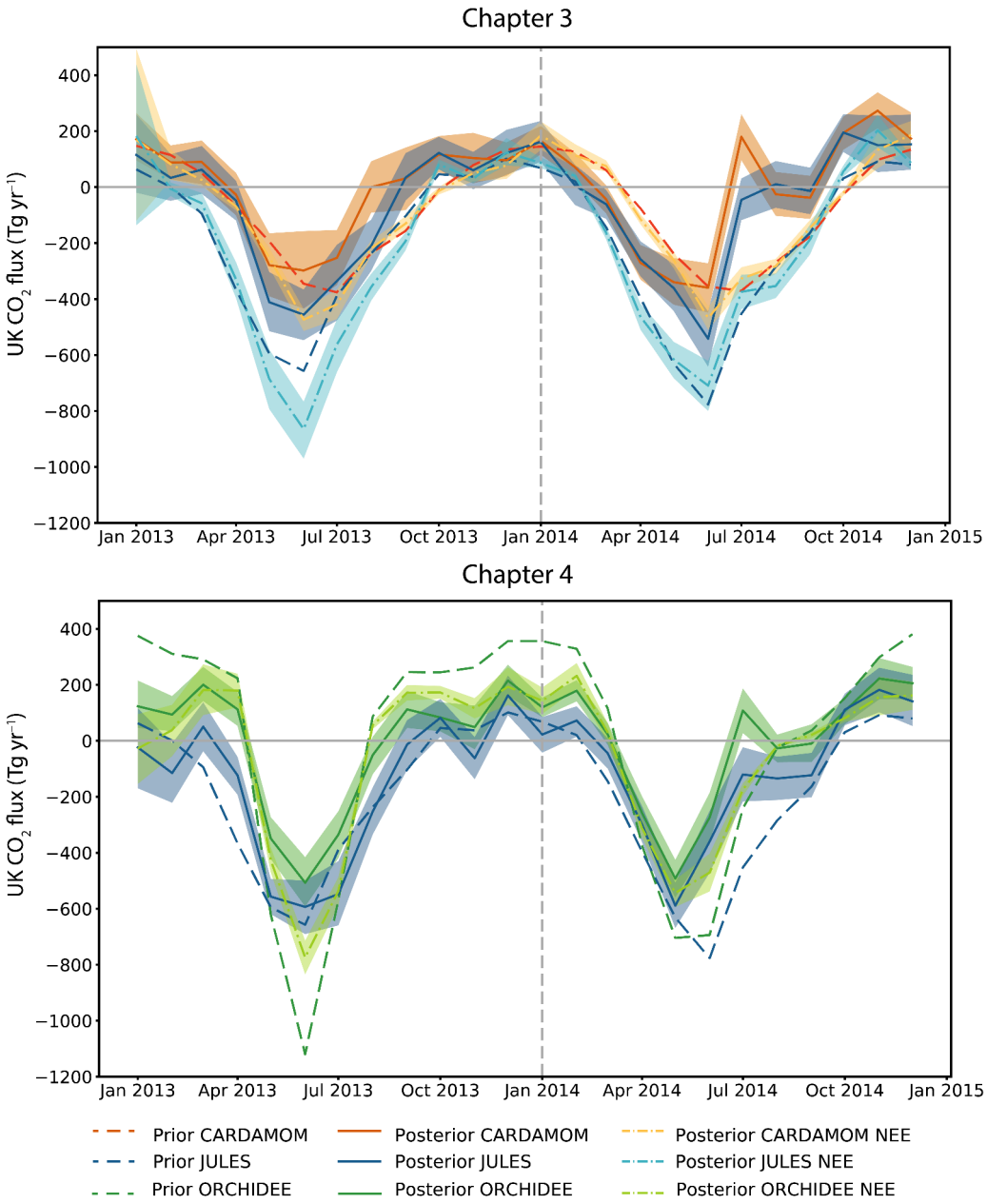

Fig. 5.1: Monthly prior and posterior biospheric CO_2 fluxes from Chapter 3 (top) and Chapter 4 (bottom) over 2013–2014. Shading represents 5th–95th percentile.

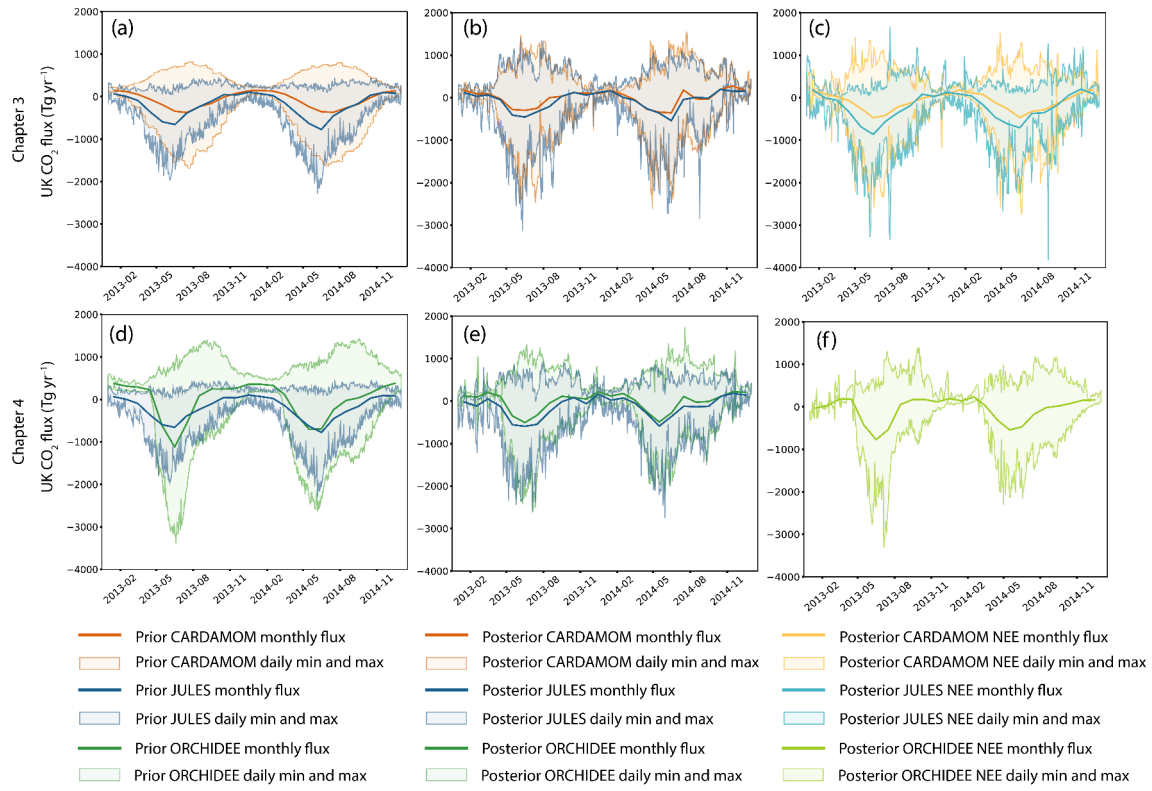

Fig. 5.2: Diurnal flux range over 2013–2014. (a-c) shows results from Chapter 3, (d-f) shows results from Chapter 4. (a and d): prior fluxes. (b and e): posterior results from gross flux inversions. (c and f): posterior results from net flux inversions. The sub-daily fluxes were averaged to 6-hourly before the diurnal range was computed as ORCHIDEE is available at 3-hourly temporal resolution and CARDAMOM and JULES are available at 2-hourly temporal resolution.

According to the posterior results, it seems to get the right timing for the growth of the spring uptake in March, April and May and provides the best fit to the summer/autumn increase in NEE during July, August and September, with the points of inflexion of the seasonal cycle occurring in April and July in 2013 and March and July in 2014. This means that the ORCHIDEE net flux inversion, whilst overestimating the sink in June and July, provides a better fit to the ORCHIDEE gross flux inversions than the JULES and CARDAMOM net flux inversions from Chapter 3. The JULES prior, on the other hand, estimates the spring uptake to be too early and the CARDAMOM prior estimates the spring uptake to be too late, according to the posterior results, with the spring points of inflexion of the seasonal cycles occurring in March of both years for JULES and April of both years for CARDAMOM. The summer/autumn increase in NEE occurs too late in both CARDAMOM and JULES, with the autumn points of inflexion of the seasonal cycles occurring in August of both years for JULES and September of both years for CARDAMOM.

5.2.2 Diurnal range

In Chapter 4, the diurnal range of the posterior gross flux inversions (Fig. 5.2e) resemble each other well in maximum daily uptake, but less so in the maximum daily source. This is in contrast to the results of Chapter 3 (Fig. 5.2b), which resemble each other well in both the maximum daily source and uptake. The ORCHIDEE net flux inversion from Chapter 4 agrees somewhat with the corresponding gross flux inversion, as does the CARDAMOM net flux inversion from Chapter 3, however this is certainly not the case for the JULES net and gross flux inversions of Chapter 3.

Common features across the posterior diurnal ranges from gross flux inversions in both chapters (Fig. 5.2b and 5.2e) are their similar magnitude and general profile. From a qualitative examination, a second minimum seen in the ORCHIDEE prior in 2014 around September (Fig. 5.2d) may also be appearing in the posterior results of the gross flux inversions.

5.2.3 Annual estimates

The annual flux estimates for all inversions from Chapters 3 and 4 are shown in Fig. 5.3. The NEE results of the three inversions in Chapter 4 agree within the uncertainties in 2013 and 2014, however they are in better agreement in 2014. The posterior TER and GPP fluxes from the gross inversions also agree well. From Chapter 3, the JULES net flux inversion is the only one that does not always agree with the other NEE estimates within the uncertainties. The TER and GPP fluxes of the two gross flux inversions from Chapter 3 do not agree.

Across the two studies, all NEE estimates agree within the estimated uncertainties except the JULES net flux inversion from Chapter 3. The JULES gross flux inversions from the two studies agree on the NEE, GPP and TER fluxes within the estimated uncertainties. Gross flux inversions all estimate that the UK source and sink fluxes are balanced, giving net zero flux from the biosphere, except for the JULES gross flux inversion from Chapter 4. The net flux inversions all estimate that the UK biosphere is a sink, albeit a fairly small one, of $-210\pm^{56}_{60}$ Tg CO_2 yr^{-1} in the JULES NEE inversion to -56 ± 47 Tg CO_2 yr^{-1} in the ORCHIDEE NEE inversion, averaged over the two years. This is generally consistent with the findings that net flux inversions estimate smaller fluxes than gross flux inversions, however the difference between the results of the two types of inversions is not statistically significant.

5.3 Discussion and conclusions

In general, the results are consistent across the studies in Chapter 3 and 4. The main difference between these two set-ups is the data used. Perhaps the extra constraint of data from the atmospheric measurement sites at Heathfield and Bilsdale is responsible for the estimation of larger May fluxes in 2014 and smaller summer uptake in 2013 in the results from Chapter 3? Or perhaps the inclusion of data outside the UK in the Netherlands and France (as in Chapter 4) is responsible for giving the

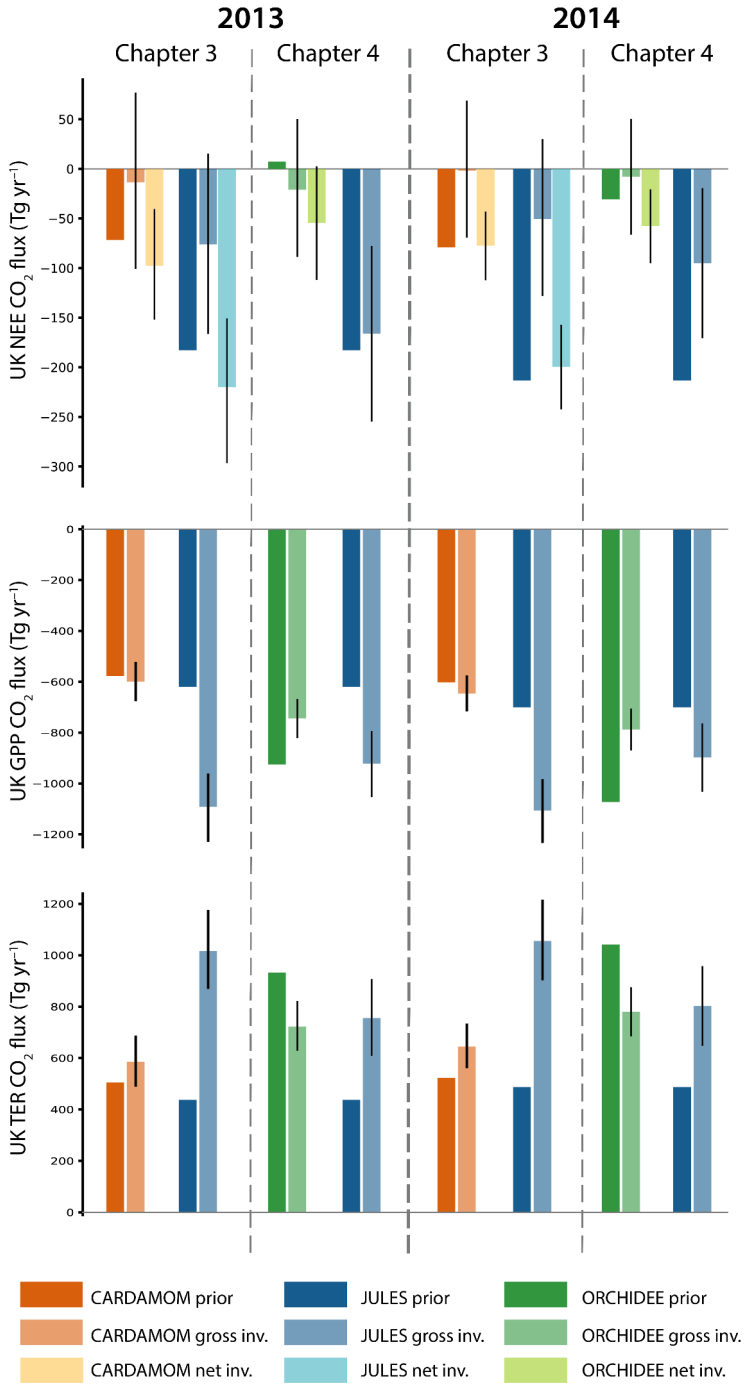

Fig. 5.3: Annual NEE, GPP and TER fluxes from Chapters 3 and 4. Bars represent 5th–95th percentile.

opposite results? Both set-ups have estimated posterior uncertainties of the same magnitude, therefore it is impossible to say whether one or other of these set ups is giving a better constrained result.

One question that remained from Chapter 4 was whether the ORCHIDEE prior was wrongly estimating disturbance fluxes in western Europe (as the seasonal cycle was well estimated elsewhere) or whether the dense network of sites in this region was allowing additional levels of detail to be resolved in the seasonal cycle. It is clear from this chapter that the ORCHIDEE prior does provide a better estimate of the timing of the seasonal cycle compared to JULES and CARDAMOM, however, it maybe has not quite captured the timing of the shut-down of the summer sink in the UK (and west Europe) as estimated by the gross flux inversions. Whether this is also the case in other areas of Europe, but cannot be seen due to the relative sparsity of data, is still an open question.

To respond to both of the questions above, a sensitivity study could be carried out for the UK using different combinations of measurement sites in the UK and nearby areas in the inversion. This may be able to pinpoint which sites are responsible for certain features in the seasonal cycle. If the responsible sites are uniquely situated in, for example a specific eco-region or representative of a range of eco-regions, then this may help to identify useful locations for future measurement sites across Europe.

It is also clear that using a prior with a good estimate of the timing of the seasonal cycle means there are fewer stark differences between net and gross flux inversions as were seen in Chapter 3. Therefore, in these cases, using a net flux inversion may be sufficient to estimate fluxes on an annual scale. However, some detail may be missed at the monthly and daily scales.

Chapter 6

Conclusion

Human activity is causing rising atmospheric CO_2 concentrations, leading to an increase in global mean temperature and a changing climate. According to the latest IPCC report, the global community has only 12 years to put in place the policies needed to limit warming to 1.5°C above natural levels and avoid some of the catastrophic effects of climate change (Masson-Delmotte et al., 2018). Monitoring biospheric CO_2 fluxes at global, continental and regional scales is important for two reasons related to climate change. Firstly, to track the success of mitigation policies that involve sequestering CO_2 in the biosphere, thought to contribute to 25% of international pledges made through the process of the Paris Agreement (Grassi et al., 2017). Secondly, to track how the biosphere is responding to increased CO_2 concentrations in the atmosphere and climate change, which are likely to have a mixture of positive and negative effects on biospheric sources and sinks.

Top-down methods at global, continental and regional scales that use atmospheric measurements of CO_2 in an inverse modelling set-up are able to evaluate the carbon cycle as a complete system. As such, the development of these methods is important for taking stock of the current state of the biosphere and tracking progress towards emissions targets and mitigation efforts at a variety of scales. In particular, regional inverse modelling has a useful role to play in estimating biospheric fluxes at scales that are relevant to national policy making, evaluating emissions targets and verifying other bottom up estimates compiled to understand national emissions.

This thesis works towards the first top-down estimates of UK biopsheric CO_2 fluxes and includes the contribution to a regional inverse modelling comparison project that focusses on European biospheric CO_2 fluxes. The development of this system is a first step towards more ambitious atmospheric CO_2 inversions that can be carried out using UK and European data networks, such as those to evaluate anthropogenic CO_2 fluxes.

Up to now, the hierarchical Bayesian trans-dimensional MCMC inversion framework described in Chapter 1 has been developed and used for GHGs of predominantly anthropogenic origin, with no diurnal cycle and a flux that cannot be negative. In Chapter 2, this framework was adapted to the unique characteristics of CO_2 fluxes, which have a strong diurnal cycle and co-located anthropogenic and

biospheric sources and biospheric sinks. One of the major changes was to introduce a disaggregation of the footprints from the LPDM NAME to enable correct simulation of the timing of the diurnal cycle in the forward model. A set of synthetic tests, using "true" fluxes created with one model of biospheric fluxes (CARDAMOM) and prior fluxes from a different model (JULES), were used to explore a number of changes to the initial framework and to find the optimum set-up for estimating biospheric CO_2 fluxes using the UK's UK-DECC and GAUGE measurement networks.

Overall, a set-up was achieved that was able to recreate the "true" fluxes well in a synthetic data experiment. Various tests concluded that: disaggregating footprints back in time for the first 24 hours is sufficient to correctly simulate the timing of the diurnal cycle in the forward model, balancing simulation accuracy and computational efficiency; attempting to find an estimate for anthropogenic as well as biospheric fluxes is not possible with the current atmospheric CO_2 concentration dataset due to the co-location of sources; allowing the data to guide the number of temporal regions as opposed to the number of spatial regions made a significant improvement to posterior flux estimates due to the added flexibility in the time dimension (particularly important to cope with rapidly varying CO_2 fluxes and boundary conditions); and that including all measurements in the inversion actually gives an incorrect posterior estimate in summer months, whilst using a filter that only includes times where the atmosphere is thought to be well-mixed improves the result. Finally, an important finding was made that a separation of NEE into its positive (TER) and negative (GPP) components (to be scaled individually in the inversion) is required to give the system the flexibility it needs to find the "true" solution.

Whilst tests with synthetic data are useful to diagnose the abilities and limitations of a modelling system, it is only with real data that the actual potential of the system can be exposed. In Chapter 3 the inverse set-up developed in Chapter 2 was applied to the real atmospheric CO_2 concentration measurements from the UK-DECC and GAUGE networks to find an estimate for UK biospheric CO_2 fluxes. The same models of biospheric fluxes as used in Chapter 2, CARDAMOM and JULES, provided prior constraints in two different inversions in order to assess the impact of the choice of prior model on the inversion result and the consistency of the underlying processes in those models with atmospheric CO_2 concentrations.

Over the period of the inversions, 2013-2014, the UK biosphere was found to be in balance as the CO_2 sources roughly equalled the CO_2 sinks, giving annual net fluxes of -8 ± 79 Tg CO_2 yr^{-1} and -64 ± 85 Tg CO_2 yr^{-1} according to the CARDAMOM and JULES inversions respectively (uncertainty is the 5th-95th percentile range). Whilst the prior models of biospheric fluxes exhibited significant differences, the posterior results were consistent between the two inversions, implying that the set-up can provide a data-driven result. The prior models were found to underestimate spring and summer fluxes, perhaps highlighting one particular limitation of these models as they do not simulate fluxes from human disturbance and the larger fluxes inferred by the inversions could be partly due to increased respiration fluxes during crop harvest. However, when the same inversions were carried out scaling the NEE as opposed to the GPP and TER fluxes separately, the results between the inversions

were not consistent and did not change dramatically from the prior mean estimate. This reinforced the finding in Chapter 2, that separating the GPP and TER fluxes is important in this set-up and can potentially allow the inversion to resolve changes in the net flux that are not accounted for in the prior models.

Extending the scope of the inversion to include the whole of Europe to contribute to the EUROCOM intercomparison project enabled a comparison of the results produced here with previous European biospheric CO_2 flux estimates. Using 15 measurement stations from the ICOS data network and prior biospheric fluxes from the ORCHIDEE and JULES models, Chapter 4 focussed on estimating the whole European biospheric CO_2 flux budget, along with regional flux estimates.

European biospheric CO_2 fluxes were found to be in balance according to the inversions carried out here. Using ORCHIDEE prior fluxes (over 2011-2015) the mean annual net flux was 779 ± 1568 Tg yr^{-1} (uncertainty is 1σ) and using JULES prior fluxes (over 2013-2014) the mean annual net flux was -485 ± 1068 Tg yr^{-1}. These results agree with other estimates from regional inverse studies (e.g. Peters et al., 2010), however they are at the upper end of estimates across a range of different methods. Given the distribution of measurement sites used in this study, biospheric CO_2 flux estimates for western and central Europe were the best constrained. Whilst there are other measurement sites that could be incorporated into the work, the distribution used is generally representative of the spread of sites in the ICOS network and highlights a need to expand the network in other areas.

The work in Chapter 4 also added new insight to the question of separating GPP and TER fluxes. As ORCHIDEE includes processes of human disturbance, biospheric CO_2 flux estimates from the model are expected to be more realistic. In two inversions that scaled the net and gross fluxes and used ORCHIDEE as the prior model, there were only small differences between monthly posterior estimates. This was true in all but one region, western Europe, where the two inversions were mostly in agreement except in summer where the net flux inversion estimated more uptake than the gross flux inversion (similar to the findings of Chapter 3). This suggested that when using a prior that includes disturbance fluxes, carrying out an inversion that scales the net flux may be sufficient. However, the differences between the gross and net flux inversions in western Europe suggested either that it is only with a denser network of sites that the benefits of a gross flux inversion can be seen and ORCHIDEE is poorly estimating disturbance and/or natural biospheric fluxes elsewhere as well, or that ORCHIDEE is not correctly estimating the disturbance and/or natural biospheric fluxes in this particular region. The inversion using JULES as the prior biospheric flux model (that does not include disturbance fluxes) agreed with the ORCHIDEE gross flux inversions at the times where the ORCHIDEE gross and net flux inversions disagreed, implying that whether or not the prior model accounts for disturbance has minimal impact on the result in a gross flux inversion.

As the inversion domains for the estimates of UK and European biospheric CO_2 fluxes overlap, it would be expected that the fluxes found over the UK in the European study (in Chapter 4) should be consistent with the fluxes found over the UK in the UK-focussed study (in Chapter 3). Chapter 5 served to bring the results of Chapters 3 and 4 together to investigate this and found that they were indeed

consistent. The main difference between the two inversion set-ups was the number of measurement sites in and around the UK. Given that the uncertainty estimates on the results from the two set-ups were of a similar size, it was difficult to say which of the two configurations of sites was best able to constrain the posterior flux. As in Chapter 4, the net and gross flux inversions using ORCHIDEE were mostly in agreement, potentially indicating that a net flux inversion is sufficient when evaluating fluxes on an annual scale if using a prior that includes disturbance fluxes. However, some detail may be missed when evaluating fluxes on a monthly scale as the net flux inversion estimated a larger summer sink than the gross flux inversion.

6.1 Future work

Although the results of Chapter 4 are contributing to an intercomparison project of European biospheric CO_2 fluxes, the project is ongoing so the results of the intercomparison have not been presented here. However, it is through intercomparisons such as this that a more thorough investigation of the strengths and weaknesses of each set-up can be carried out and the results of the project are sure to highlight some areas for improvement for the set-up developed in this thesis. Equally, a similar comparison should be attempted with a focus over the UK to assess the particular ability of this set-up to evaluate UK biospheric fluxes with data from the UK-DECC and GAUGE networks, and in fact work along these lines is currently in the preparation stages.

This thesis has also left some specific unanswered questions that further work could help to answer. Firstly, there is the speculation that the GPP and TER fluxes may be separately resolved if changes could be made to the diurnal cycle within the inversion. Currently the trans-dimensional inversion in *time* is able to split the one month inversion window into smaller chunks of time down to a minimum daily resolution. If that time could be further broken down into perhaps six-hourly chunks it is possible that sub-daily fluxes could be scaled to improve the timing or amplitude of the diurnal cycle and this is worth investigating. However, as it currently stands it is likely that there would not be enough data available for the inversion to make sub-daily changes to fluxes.

Secondly, it is not known whether the dense network of sites in western Europe is responsible for the differences seen between the ORCHIDEE net and gross flux inversions or whether ORCHIDEE is poorly estimating biospheric fluxes in this area. To investigate this question a site sensitivity analysis could be carried out, trialling different combinations of measurement sites, to see which sites are responsible for certain features of the seasonal cycle. There are also monthly differences between the inversion results compared in Chapter 5 that use different sets of measurement sites so this same sensitivity test could also help to identify where these different sets of sites provide different constraints. This would help to understand the sites that give information about particular areas of fluxes and could aid the future identification of new measurement sites across Europe.

6.2 Outlook

The purpose of developing a top-down inverse method for CO_2 flux estimation over the UK was to advance the scientific community's ability to report CO_2 fluxes to the UK government and to track changes to the biosphere that might reflect mitigation strategies or the biosphere's response to climate change. Neither of these goals are possible yet. To achieve this the inverse system needs to move towards estimation of anthropogenic emissions and even flux estimates for individual sectors. This will involve improvements across all components of the inverse modelling framework.

In order to separate source sectors, measurements of co-emitted gases, introduced in Sect. 2.1 (e.g. CO, ^{14}C, APO), must be made routinely at measurement sites across the UK. Incorporating these measurements into inverse modelling frameworks will help to disentangle the anthropogenic and biospheric components of the atmospheric CO_2 signal. Although the measurement network in the UK and Republic of Ireland is thought to be relatively dense compared to other regions, there are still potentially large gaps in what can be inferred about surface fluxes from the measurements at the six UK-DECC and GAUGE sites. The use of satellite data in atmospheric inversions, from satellites such as OCO-2, is growing as researchers overcome the problems associated with handling large data-sets (e.g. Ganesan et al., 2017). Introducing satellite data into CO_2 inversions in the UK may improve understanding of biospheric and anthropogenic fluxes with increased coverage. It would also provide further insight to the simple site analysis suggested earlier that may decipher which measurements provide a constraint on which parts of the seasonal cycle.

The uncertainties in the atmospheric transport model are the most difficult to assess and have not been given much attention in this thesis, since only one atmospheric transport model has been used. This is another reason why intercomparison projects that compare set-ups using different transport models are so important. In particular, it is at times of stagnant wind conditions that atmospheric transport models tend to struggle to represent the actual transport patterns. Inverse studies repeatedly state that improvements to atmospheric transport models may help to improve results (e.g. Chevallier et al., 2014; Peylin et al., 2011). Promising developments in studies using measurements of Radon (^{222}Rn), commonly used as a tracer in atmospheric transport experiments, could help to further understand the dynamics of transport models and the times at which they are well representing atmospheric conditions (e.g. Taguchi et al., 2011).

From the range of estimates produced by the models of biospheric fluxes used in this thesis (JULES, CARDAMOM and ORCHIDEE), it is clear that there is a long way to go to harmonise bottom-up estimates of biospheric CO_2 fluxes. Atmospheric inverse modelling can go some way to identify the processes in the models leading to inconsistencies with atmospheric CO_2 measurements. However, a more thorough approach would be to couple the transport model and the model of biospheric fluxes, which would enable parameters in the biospheric flux model to be directly updated in response to atmospheric measurements and allow a more robust analysis of the uncertainties in the system. This has been attempted before in carbon cycle data assimilation systems (e.g Kaminski et al.,

2013; Peylin et al., 2016). However, a dedicated effort to assimilate high resolution data over the UK could provide important insight to the UK's biospheric processes on both managed and un-managed land.

Looking further afield to improving estimates of European biospheric CO_2 fluxes, one of the main limiting factors for inverse modelling studies is the lack of measurement sites in the north, east and south of Europe. Increasing the number of measurement sites in eastern Europe may shed light on whether regional inverse modelling studies can infer the same large sink in this area as is found in inverse modelling studies using satellite measurements (Houweling et al., 2015; Nassar et al., 2011; Reuter et al., 2014).

To conclude, this thesis takes an important first step in the estimation of UK and European CO_2 budgets, through developing an appropriate method and finding estimates for biospheric CO_2 fluxes across different scales. According to the inversion results, both the UK and Europe are found to be in balance in regards to biospheric sources and sinks, in general estimating less negative fluxes than those found using models of biospheric fluxes. This work will provide the foundation to future atmospheric CO_2 inversion studies, using NAME within a hierarchical Bayesian inversion framework and also makes a recommendation to the wider inverse modelling community to consider separately scaling positive and negative fluxes. Tracking CO_2 fluxes using atmospheric inverse modelling approaches holds a lot of promise and will be a key tool for guiding the world towards the emissions reductions required for a safe climate in the future.

References

Atkin, O. K., Bloomfield, K. J., Reich, P. B., Tjoelker, M. G., Asner, G. P., Bonal, D., Bönisch, G., Bradford, M. G., Cernusak, L. A., Cosio, E. G., Creek, D., Crous, K. Y., Domingues, T. F., Dukes, J. S., Egerton, J. J. G., Evans, J. R., Farquhar, G. D., Fyllas, N. M., Gauthier, P. P. G., Gloor, E., Gimeno, T. E., Griffin, K. L., Guerrieri, R., Heskel, M. A., Huntingford, C., Ishida, F. Y., Kattge, J., Lambers, H., Liddell, M. J., Lloyd, J., Lusk, C. H., Martin, R. E., Maksimov, A. P., Maximov, T. C., Malhi, Y., Medlyn, B. E., Meir, P., Mercado, L. M., Mirotchnick, N., Ng, D., Niinemets, Ü., O'Sullivan, O. S., Phillips, O. L., Poorter, L., Poot, P., Prentice, I. C., Salinas, N., Rowland, L. M., Ryan, M. G., Sitch, S., Slot, M., Smith, N. G., Turnbull, M. H., VanderWel, M. C., Valladares, F., Veneklaas, E. J., Weerasinghe, L. K., Wirth, C., Wright, I. J., Wythers, K. R., Xiang, J., Xiang, S., and Zaragoza-Castells, J. (2015). Global variability in leaf respiration in relation to climate, plant functional types and leaf traits. *New Phytologist*, 206(2):614–636.

Baldocchi, D. D. and Wilson, K. B. (2001). Modeling CO_2 and water vapor exchange of a temperate broadleaved forest across hourly to decadal time scales. *Ecological Modelling*, 142(1-2):155–184.

Bastos, A., Janssens, I. A., Gouveia, C. M., Trigo, R. M., Ciais, P., Chevallier, F., Peñuelas, J., Rödenbeck, C., Piao, S., Friedlingstein, P., and Running, S. W. (2016). European land CO_2 sink influenced by NAO and East-Atlantic Pattern coupling. *Nature Communications*, 7:10315.

Basu, S., Guerlet, S., Butz, A., Houweling, S., Hasekamp, O., Aben, I., Krummel, P., Steele, P., Langenfelds, R., Torn, M., Biraud, S., Stephens, B., Andrews, A., and Worthy, D. (2013). Global CO_2 fluxes estimated from GOSAT retrievals of total column CO_2. *Atmospheric Chemistry and Physics*, 13(17):8695–8717.

Berchet, A., Pison, I., Chevallier, F., Bousquet, P., Conil, S., Geever, M., Laurila, T., Lavrič, J., Lopez, M., Moncrieff, J., Necki, J., Ramonet, M., Schmidt, M., Steinbacher, M., and Tarniewicz, J. (2013). Towards better error statistics for atmospheric inversions of methane surface fluxes. *Atmospheric Chemistry and Physics*, 13(14):7115–7132.

Berry, J., Collatz, G., Defries, R., and Still, C. (2009). ISLSCP II C4 Vegetation Percentage. Technical report, Environmental Sciences Division, Oak Ridge National Laboratory, Oak Ridge, Tennessee.

Best, M. J., Pryor, M., Clark, D. B., Rooney, G. G., Essery, R. L. H., Ménard, C. B., Edwards, J. M., Hendry, M. A., Porson, A., Gedney, N., Mercado, L. M., Sitch, S., Blyth, E., Boucher, O., Cox, P. M., Grimmond, C. S. B., and Harding, R. J. (2011). The Joint UK Land Environment Simulator (JULES), model description – Part 1: Energy and water fluxes. *Geosci. Model Dev.*, 4(3):677–699.

Bloom, A. A., Exbrayat, J.-F., van der Velde, I. R., Feng, L., and Williams, M. (2016). The decadal state of the terrestrial carbon cycle: Global retrievals of terrestrial carbon allocation, pools, and residence times. *Proceedings of the National Academy of Sciences*, 113(5):1285–1290.

Bloom, A. A. and Williams, M. (2015). Constraining ecosystem carbon dynamics in a data-limited world: integrating ecological "common sense" in a model–data fusion framework. *Biogeosciences*, 12(5):1299–1315.

References

Boden, T. A., Marland, G., and Andres, R. J. (2018). Global, regional and national fossil-fuel co$_2$ emissions. Technical report, Oak Ridge National Laboratory, U.S. Department of Energy.

Brown, P., Broomfield, M., Cardenas, L., Choudrie, S., Kilroy, E., Jones, L., MacCarthy, J., Passant, N., Thistlethwaite, G., Thomson, A., Wakeling, D., Buys, G., Gilhespy, S., Glendining, M., Gluckman, R., Hampshire, K., Henshall, P., Hobson, M., Malcolm, H., Manning, A., Matthews, R., Milne, A., Misselbrook, T., Moxley, J., Murrells, T., Salisbury, E., Walker, C., and Watterson, J. (2018). UK Greenhouse Gas Inventory, 1990 to 2016: Annual Report for submission under the Framework Convention on Climate Change. Technical report, Ricardo Energy and Environment.

Bruhwiler, L. M. P., Michalak, A. M., and Tans, P. P. (2011). Spatial and temporal resolution of carbon flux estimates for 1983–2002. *Biogeosciences*, 8(5):1309–1331.

Campbell, J. E., Berry, J. A., Seibt, U., Smith, S. J., Montzka, S. A., Launois, T., Belviso, S., Bopp, L., and Laine, M. (2017). Large historical growth in global terrestrial gross primary production. *Nature*, 544(7648):84–87.

Chevallier, F., Ciais, P., Conway, T. J., Aalto, T., Anderson, B. E., Bousquet, P., Brunke, E. G., Ciattaglia, L., Esaki, Y., Fröhlich, M., Gomez, A., Gomez-Pelaez, A. J., Haszpra, L., Krummel, P. B., Langenfelds, R. L., Leuenberger, M., Machida, T., Maignan, F., Matsueda, H., Morguí, J. A., Mukai, H., Nakazawa, T., Peylin, P., Ramonet, M., Rivier, L., Sawa, Y., Schmidt, M., Steele, L. P., Vay, S. A., Vermeulen, A. T., Wofsy, S., and Worthy, D. (2010). CO_2 surface fluxes at grid point scale estimated from a global 21 year reanalysis of atmospheric measurements. *Journal of Geophysical Research: Atmospheres*, 115(D21).

Chevallier, F., Palmer, P. I., Feng, L., Boesch, H., O'Dell, C. W., and Bousquet, P. (2014). Toward robust and consistent regional CO_2 flux estimates from in situ and spaceborne measurements of atmospheric CO_2. *Geophysical Research Letters*, 41(3):1065–1070.

Ciais, P., Sabine, C., Bala, G., Bopp, L., Brovkin, V., Canadell, J., Chhabra, A., DeFries, R., Galloway, J., Heimann, M., Jones, C., Quéré, C. L., Myneni, R., Piao, S., and Thornton, P. (2013). 2013: Carbon and Other Biogeochemical Cycles. In Stocker, T., Qin, D., Plattner, G.-K., Tignor, M., Allen, S., Boschung, J., Nauels, A., Xia, Y., Bex, V., and Midgley, P., editors, *Climate Change 2013: The Physical Science Basis. Contribution of Working Group I to the Fifth Assessment Report of the Intergovernmental Panel on Climate Change*. Cambridge University Press, Cambridge, United Kingdom and New York, NY, USA.

Clark, D. B., Mercado, L. M., Sitch, S., Jones, C. D., Gedney, N., Best, M. J., Pryor, M., Rooney, G. G., Essery, R. L. H., Blyth, E., Boucher, O., Harding, R. J., Huntingford, C., and Cox, P. M. (2011). The Joint UK Land Environment Simulator (JULES), model description – Part 2: Carbon fluxes and vegetation dynamics. *Geoscientific Model Development*, 4(3):701–722.

Cullen, M. J. P. (1993). The unified forecast/climate model. *The Meteorological Magazine*, 122:81–94.

DEFRA (2014). Agriculture Statistics in 2013. Technical report, Department for Environment Food and Rural Affairs, UK government.

DEFRA (2015). Agriculture Statistics in 2014. Technical report, Department for Environment Food and Rural Affairs, UK government.

Denning, A. S., Randall, D. A., Collatz, G. J., and Sellers, P. J. (1996). Simulations of terrestrial carbon metabolism and atmospheric CO_2 in a general circulation model. *Tellus B*, 48(4):543–567.

Dlugokencky, E., Lang, P., Mund, J., Crotwell, A., Crotwell, M., and Thoning, K. (2018). Atmospheric Carbon Dioxide Dry Air Mole Fractions from the NOAA ESRL Carbon Cycle Cooperative Global Air Sampling Network, 1968-2017, Version: 2018-07-31. Technical report.

Dlugokencky, E. and Tans, P. (2018). Trends in atmospheric carbon dioxide. Technical report, National Oceanic and Atmospheric Administration, Earth System Research Laboratory (NOAA/ESRL).

EC-JRC/PBL (2011). Emissions Database for Global Atmospheric Research. Technical report, European Comission, Joint Research Centre (JRC)/ Netherlands Environmental Assessment Agency (PBL).

Emmons, L. K., Walters, S., Hess, P. G., Lamarque, J.-F., Pfister, G. G., Fillmore, D., Granier, C., Guenther, A., Kinnison, D., Laepple, T., Orlando, J., Tie, X., Tyndall, G., Wiedinmyer, C., Baughcum, S. L., and Kloster, S. (2010). Description and evaluation of the Model for Ozone and Related chemical Tracers, version 4 (MOZART-4). *Geosci. Model Dev.*, 3(1):43–67.

Enting, I. G. and Mansbridge, J. V. (1989). Seasonal sources and sinks of atmospheric CO_2 Direct inversion of filtered data. *Tellus B*, 41B(2):111–126.

Enting, I. G., Trudinger, C. M., and Francey, R. J. (1995). A synthesis inversion of the concentration and δ^{13}C of atmospheric CO_2. *Tellus B*, 47(1-2):35–52.

Fang, Y., Michalak, A. M., Shiga, Y. P., and Yadav, V. (2014). Using atmospheric observations to evaluate the spatiotemporal variability of CO_2 fluxes simulated by terrestrial biospheric models. *Biogeosciences*, 11(23):6985–6997.

FAO/IIASA/ISRIC/ISS-CAS/JRC (2009). Harmonized World Soil Database (version 1.1). Technical report, FAO, Rome, Italy and IIASA, Laxenburg, Austria.

Feng, L., Palmer, P. I., Parker, R. J., Deutscher, N. M., Feist, D. G., Kivi, R., Morino, I., and Sussmann, R. (2016). Estimates of european uptake of CO_2 inferred from GOSAT X_{CO_2} retrievals: sensitivity to measurement bias inside and outside europe. *Atmospheric Chemistry and Physics*, 16(3):1289–1302.

Friedlingstein, P., Cox, P., Betts, R., Bopp, L., von Bloh, W., Brovkin, V., Cadule, P., Doney, S., Eby, M., Fung, I., Bala, G., John, J., Jones, C., Joos, F., Kato, T., Kawamiya, M., Knorr, W., Lindsay, K., Matthews, H. D., Raddatz, T., Rayner, P., Reick, C., Roeckner, E., Schnitzler, K.-G., Schnur, R., Strassmann, K., Weaver, A. J., Yoshikawa, C., and Zeng, N. (2006). Climate–Carbon Cycle Feedback Analysis: Results from the C4MIP Model Intercomparison. *Journal of Climate*, 19(14):3337–3353.

Ganesan, A. L., Manning, A. J., Grant, A., Young, D., Oram, D. E., Sturges, W. T., Moncrieff, J. B., and O'Doherty, S. (2015). Quantifying methane and nitrous oxide emissions from the UK and Ireland using a national-scale monitoring network. *Atmospheric Chemistry and Physics*, 15(11):6393–6406.

Ganesan, A. L., Rigby, M., Lunt, M. F., Parker, R. J., Boesch, H., Goulding, N., Umezawa, T., Zahn, A., Chatterjee, A., Prinn, R. G., Tiwari, Y. K., Schoot, M. v. d., and Krummel, P. B. (2017). Atmospheric observations show accurate reporting and little growth in India's methane emissions. *Nature Communications*, 8(1):836.

Ganesan, A. L., Rigby, M., Zammit-Mangion, A., Manning, A. J., Prinn, R. G., Fraser, P. J., Harth, C. M., Kim, K.-R., Krummel, P. B., Li, S., Mühle, J., O'Doherty, S. J., Park, S., Salameh, P. K., Steele, L. P., and Weiss, R. F. (2014). Characterization of uncertainties in atmospheric trace gas inversions using hierarchical Bayesian methods. *Atmospheric Chemistry and Physics*, 14(8):3855–3864.

Gerbig, C., Dolman, A. J., and Heimann, M. (2009). On observational and modelling strategies targeted at regional carbon exchange over continents. *Biogeosciences*, 6(10):1949–1959.

Gerbig, C., Lin, J. C., Wofsy, S. C., Daube, B. C., Andrews, A. E., Stephens, B. B., Bakwin, P. S., and Grainger, C. A. (2003a). Toward constraining regional-scale fluxes of CO_2 with atmospheric observations over a continent: 1. Observed spatial variability from airborne platforms. *Journal of Geophysical Research: Atmospheres*, 108(D24):n/a–n/a.

Gerbig, C., Lin, J. C., Wofsy, S. C., Daube, B. C., Andrews, A. E., Stephens, B. B., Bakwin, P. S., and Grainger, C. A. (2003b). Toward constraining regional-scale fluxes of CO_2 with atmospheric observations over a continent: 2. Analysis of COBRA data using a receptor-oriented framework. *Journal of Geophysical Research: Atmospheres*, 108(D24).

Göckede, M., Michalak, A. M., Vickers, D., Turner, D. P., and Law, B. E. (2010). Atmospheric inverse modeling to constrain regional-scale CO_2 budgets at high spatial and temporal resolution. *Journal of Geophysical Research*, 115(D15).

Gourdji, S. M., Hirsch, A. I., Mueller, K. L., Yadav, V., Andrews, A. E., and Michalak, A. M. (2010). Regional-scale geostatistical inverse modeling of North American CO_2 fluxes: a synthetic data study. *Atmos. Chem. Phys.*, page 17.

Gourdji, S. M., Mueller, K. L., Yadav, V., Huntzinger, D. N., Andrews, A. E., Trudeau, M., Petron, G., Nehrkorn, T., Eluszkiewicz, J., Henderson, J., Wen, D., Lin, J., Fischer, M., Sweeney, C., and Michalak, A. M. (2012). North American CO_2 exchange: inter-comparison of modeled estimates with results from a fine-scale atmospheric inversion. *Biogeosciences*, 9(1):457–475.

Grassi, G., House, J., Dentener, F., Federici, S., den Elzen, M., and Penman, J. (2017). The key role of forests in meeting climate targets requires science for credible mitigation. *Nature Climate Change*, 7(3):220–226.

Grassi, G., House, J., Kurz, W. A., Cescatti, A., Houghton, R. A., Peters, G. P., Sanz, M. J., Viñas, R. A., Alkama, R., Arneth, A., Bondeau, A., Dentener, F., Fader, M., Federici, S., Friedlingstein, P., Jain, A. K., Kato, E., Koven, C. D., Lee, D., Nabel, J. E. M. S., Nassikas, A. A., Perugini, L., Rossi, S., Sitch, S., Viovy, N., Wiltshire, A., and Zaehle, S. (2018). Reconciling global-model estimates and country reporting of anthropogenic forest CO_2 sinks. *Nature Climate Change*, 8(10):914–920.

Graven, H. D., Keeling, R. F., Piper, S. C., Patra, P. K., Stephens, B. B., Wofsy, S. C., Welp, L. R., Sweeney, C., Tans, P. P., Kelley, J. J., Daube, B. C., Kort, E. A., Santoni, G. W., and Bent, J. D. (2013). Enhanced Seasonal Exchange of CO_2 by Northern Ecosystems Since 1960. *Science*, 341(6150):1085–1089.

Green, P. J. (1995). Reversible jump Markov chain Monte Carlo computation and Bayesian model determination. *Biometrika*, 82(4):711–732.

Griscom, B. W., Adams, J., Ellis, P. W., Houghton, R. A., Lomax, G., Miteva, D. A., Schlesinger, W. H., Shoch, D., Siikamäki, J. V., Smith, P., Woodbury, P., Zganjar, C., Blackman, A., Campari, J., Conant, R. T., Delgado, C., Elias, P., Gopalakrishna, T., Hamsik, M. R., Herrero, M., Kiesecker, J., Landis, E., Laestadius, L., Leavitt, S. M., Minnemeyer, S., Polasky, S., Potapov, P., Putz, F. E., Sanderman, J., Silvius, M., Wollenberg, E., and Fargione, J. (2017). Natural climate solutions. *Proceedings of the National Academy of Sciences*, 114(44):11645–11650.

Gurney, K. R., Law, R. M., Denning, A. S., Rayner, P. J., Baker, D., Bousquet, P., Bruhwiler, L., Chen, Y.-H., Ciais, P., Fan, S., Fung, I. Y., Gloor, M., Heimann, M., Higuchi, K., John, J., Kowalczyk, E., Maki, T., Maksyutov, S., Peylin, P., Prather, M., Pak, B. C., Sarmiento, J., Taguchi, S., Takahashi, T., and Yuen, C.-W. (2003). TransCom 3 CO_2 inversion intercomparison: 1. Annual mean control results and sensitivity to transport and prior flux information. *Tellus B*, 55(2):555–579.

Gurney, K. R., Law, R. M., Denning, A. S., Rayner, P. J., Pak, B. C., Baker, D., Bousquet, P., Bruhwiler, L., Chen, Y.-H., Ciais, P., Fung, I. Y., Heimann, M., John, J., Maki, T., Maksyutov, S., Peylin, P., Prather, M., and Taguchi, S. (2004). Transcom 3 inversion intercomparison: Model mean results for the estimation of seasonal carbon sources and sinks. *Global Biogeochemical Cycles*, 18(1).

Hansen, M. C., Potapov, P. V., Moore, R., Hancher, M., Turubanova, S. A., Tyukavina, A., Thau, D., Stehman, S. V., Goetz, S. J., Loveland, T. R., Kommareddy, A., Egorov, A., Chini, L., Justice, C. O., and Townshend, J. R. G. (2013). High-Resolution Global Maps of 21st-Century Forest Cover Change. *Science*, 342(6160):850–853.

Hansis, E., Davis, S. J., and Pongratz, J. (2015). Relevance of methodological choices for accounting of land use change carbon fluxes. *Global Biogeochemical Cycles*, 29(8):1230–1246.

Hayes, D. J., Turner, D. P., Stinson, G., McGuire, A. D., Wei, Y., West, T. O., Heath, L. S., Jong, B. d., McConkey, B. G., Birdsey, R. A., Kurz, W. A., Jacobson, A. R., Huntzinger, D. N., Pan, Y., Post, W. M., and Cook, R. B. (2012). Reconciling estimates of the contemporary North American carbon balance among terrestrial biosphere models, atmospheric inversions, and a new approach for estimating net ecosystem exchange from inventory-based data. *Global Change Biology*, 18(4):1282–1299.

Hiederer, R. and Köchy, M. (2012). Global Soil Organic Carbon Estimates and the Harmonized World Soil Database. Technical report, Joint Research Centre of the European Commission.

Houghton, R. A. and Nassikas, A. A. (2017). Global and regional fluxes of carbon from land use and land cover change 1850–2015. *Global Biogeochemical Cycles*, 31(3):456–472.

Houweling, S., Baker, D., Basu, S., Boesch, H., Butz, A., Chevallier, F., Deng, F., Dlugokencky, E. J., Feng, L., Ganshin, A., Hasekamp, O., Jones, D., Maksyutov, S., Marshall, J., Oda, T., O'Dell, C. W., Oshchepkov, S., Palmer, P. I., Peylin, P., Poussi, Z., Reum, F., Takagi, H., Yoshida, Y., and Zhuravlev, R. (2015). An intercomparison of inverse models for estimating sources and sinks of CO2 using GOSAT measurements. *Journal of Geophysical Research: Atmospheres*, 120(10):5253–5266.

IGBP Terrestrial Carbon Working Group (1998). The Terrestrial Carbon Cycle: Implications for the Kyoto Protocol. *Science*, 280(5368):1393–1394.

Janssens, I. A., Freibauer, A., Ciais, P., Smith, P., Nabuurs, G.-J., Folberth, G., Schlamadinger, B., Hutjes, R. W. A., Ceulemans, R., Schulze, E.-D., Valentini, R., and Dolman, A. J. (2003). Europe's terrestrial biosphere absorbs 7 to 12% of European anthropogenic CO_2 emissions. *Science (New York, N.Y.)*, 300(5625):1538–1542.

Jones, A., Thomson, D., Hort, M., and Devenish, B. (2006). The U.K. Met Office's Next-Generation Atmospheric Dispersion Model, NAME III. In Borrego, C. and Norman, A.-L., editors, *Air Pollution Modeling and Its Application XVII*, pages 580–589. Springer US, Boston, MA.

Jones, G. S., Stott, P. A., and Christidis, N. (2013). Attribution of observed historical near-surface temperature variations to anthropogenic and natural causes using CMIP5 simulations. *Journal of Geophysical Research: Atmospheres*, 118(10):4001–4024.

Joos, F. and Spahni, R. (2008). Rates of change in natural and anthropogenic radiative forcing over the past 20,000 years. *Proceedings of the National Academy of Sciences*, 105(5):1425–1430.

Kaminski, T., Knorr, W., Schürmann, G., Scholze, M., Rayner, P. J., Zaehle, S., Blessing, S., Dorigo, W., Gayler, V., Giering, R., Gobron, N., Grant, J. P., Heimann, M., Hooker-Stroud, A., Houweling, S., Kato, T., Kattge, J., Kelley, D., Kemp, S., Koffi, E. N., Köstler, C., Mathieu, P.-P., Pinty, B., Reick, C. H., Rödenbeck, C., Schnur, R., Scipal, K., Sebald, C., Stacke, T., Scheltinga, A. T. v., Vossbeck, M., Widmann, H., and Ziehn, T. (2013). The BETHY/JSBACH Carbon Cycle Data Assimilation System: experiences and challenges. *Journal of Geophysical Research: Biogeosciences*, 118(4):1414–1426.

Kaminski, T., Rayner, P. J., Heimann, M., and Enting, I. G. (2001). On aggregation errors in atmospheric transport inversions. *Journal of Geophysical Research: Atmospheres*, 106(D5):4703–4715.

Keeling, C. D., Bacastow, R. B., Bainbridge, A. E., Ekdahl, C. A., Guenther, P. R., Waterman, L. S., and Chin, J. F. S. (1976). Atmospheric carbon dioxide variations at Mauna Loa Observatory, Hawaii. *Tellus*, 28(6):538–551.

Kiehl, J. T. and Trenberth, K. E. (1997). Earth's Annual Global Mean Energy Budget. *Bulletin of the American Meteorological Society*, 78(2):197–208.

Kountouris, P., Gerbig, C., Rödenbeck, C., Karstens, U., Koch, T. F., and Heimann, M. (2018a). Atmospheric CO_2 inversions on the mesoscale using data-driven prior uncertainties: quantification of the European terrestrial CO_2 fluxes. *Atmospheric Chemistry and Physics*, 18(4):3047–3064.

Kountouris, P., Gerbig, C., Rödenbeck, C., Karstens, U., Koch, T. F., and Heimann, M. (2018b). Technical Note: Atmospheric CO_2 inversions on the mesoscale using data-driven prior uncertainties: methodology and system evaluation. *Atmospheric Chemistry and Physics*, 18(4):3027–3045.

Krinner, G., Viovy, N., Noblet-Ducoudré, N. d., Ogée, J., Polcher, J., Friedlingstein, P., Ciais, P., Sitch, S., and Prentice, I. C. (2005). A dynamic global vegetation model for studies of the coupled atmosphere-biosphere system. *Global Biogeochemical Cycles*, 19(1).

Laan, V. D., Karstens, U., Neubert, R. E. M., Laan-Luijkx, V. D., and Meijer, H. A. J. (2010). Observation-based estimates of fossil fuel-derived CO_2 emissions in the netherlands using $\Delta^{14}C$, CO and ^{222}Radon. *Tellus B: Chemical and Physical Meteorology*, 62(5):389–402.

Le Quéré, C., Andrew, R. M., Friedlingstein, P., Sitch, S., Pongratz, J., Manning, A. C., Korsbakken, J. I., Peters, G. P., Canadell, J. G., Jackson, R. B., Boden, T. A., Tans, P. P., Andrews, O. D., Arora, V. K., Bakker, D. C. E., Barbero, L., Becker, M., Betts, R. A., Bopp, L., Chevallier, F., Chini, L. P., Ciais, P., Cosca, C. E., Cross, J., Currie, K., Gasser, T., Harris, I., Hauck, J., Haverd, V., Houghton, R. A., Hunt, C. W., Hurtt, G., Ilyina, T., Jain, A. K., Kato, E., Kautz, M., Keeling, R. F., Klein Goldewijk, K., Körtzinger, A., Landschützer, P., Lefèvre, N., Lenton, A., Lienert, S., Lima, I., Lombardozzi, D., Metzl, N., Millero, F., Monteiro, P. M. S., Munro, D. R., Nabel, J. E. M. S., Nakaoka, S.-i., Nojiri, Y., Padin, X. A., Peregon, A., Pfeil, B., Pierrot, D., Poulter, B., Rehder, G., Reimer, J., Rödenbeck, C., Schwinger, J., Séférian, R., Skjelvan, I., Stocker, B. D., Tian, H., Tilbrook, B., Tubiello, F. N., van der Laan-Luijkx, I. T., van der Werf, G. R., van Heuven, S., Viovy, N., Vuichard, N., Walker, A. P., Watson, A. J., Wiltshire, A. J., Zaehle, S., and Zhu, D. (2018). Global Carbon Budget 2017. *Earth System Science Data*, 10(1):405–448.

Le Quéré, C., Moriarty, R., Andrew, R. M., Peters, G. P., Ciais, P., Friedlingstein, P., Jones, S. D., Sitch, S., Tans, P., Arneth, A., Boden, T. A., Bopp, L., Bozec, Y., Canadell, J. G., Chini, L. P., Chevallier, F., Cosca, C. E., Harris, I., Hoppema, M., Houghton, R. A., House, J. I., Jain, A. K., Johannessen, T., Kato, E., Keeling, R. F., Kitidis, V., Klein Goldewijk, K., Koven, C., Landa, C. S., Landschützer, P., Lenton, A., Lima, I. D., Marland, G., Mathis, J. T., Metzl, N., Nojiri, Y., Olsen, A., Ono, T., Peng, S., Peters, W., Pfeil, B., Poulter, B., Raupach, M. R., Regnier, P., Rödenbeck, C.,

Saito, S., Salisbury, J. E., Schuster, U., Schwinger, J., Séférian, R., Segschneider, J., Steinhoff, T., Stocker, B. D., Sutton, A. J., Takahashi, T., Tilbrook, B., Werf, G. R. v. d., Viovy, N., Wang, Y.-P., Wanninkhof, R., Wiltshire, A., and Zeng, N. (2015). Global carbon budget 2014. *Earth System Science Data*, 7(1):47–85.

Leip, A., Skiba, U., Vermeulen, A., and Thompson, R. L. (2018). A complete rethink is needed on how greenhouse gas emissions are quantified for national reporting. *Atmospheric Environment*, 174:237–240.

Liu, Y. Y., Dijk, A. I. J. M. v., Jeu, R. A. M. d., Canadell, J. G., McCabe, M. F., Evans, J. P., and Wang, G. (2015). Recent reversal in loss of global terrestrial biomass. *Nature Climate Change*, 5(5):470–474.

Lokupitiya, R. S., Zupanski, D., Denning, A. S., Kawa, S. R., Gurney, K. R., and Zupanski, M. (2008). Estimation of global CO_2 fluxes at regional scale using the maximum likelihood ensemble filter. *Journal of Geophysical Research*, 113(D20).

Lunt, M. F., Rigby, M., Ganesan, A. L., and Manning, A. J. (2016). Estimation of trace gas fluxes with objectively determined basis functions using reversible-jump Markov chain Monte Carlo. *Geosci. Model Dev.*, 9(9):3213–3229.

Luyssaert, S., Abril, G., Andres, R., Bastviken, D., Bellassen, V., Bergamaschi, P., Bousquet, P., Chevallier, F., Ciais, P., Corazza, M., Dechow, R., Erb, K.-H., Etiope, G., Fortems-Cheiney, A., Grassi, G., Hartmann, J., Jung, M., Lathière, J., Lohila, A., Mayorga, E., Moosdorf, N., Njakou, D. S., Otto, J., Papale, D., Peters, W., Peylin, P., Raymond, P., Rödenbeck, C., Saarnio, S., Schulze, E.-D., Szopa, S., Thompson, R., Verkerk, P. J., Vuichard, N., Wang, R., Wattenbach, M., and Zaehle, S. (2012). The European land and inland water CO_2, CO, CH_4 and N_2O balance between 2001 and 2005. *Biogeosciences*, 9(8):3357–3380.

Manning, A. J., O'Doherty, S., Jones, A. R., Simmonds, P. G., and Derwent, R. G. (2011). Estimating UK methane and nitrous oxide emissions from 1990 to 2007 using an inversion modeling approach. *Journal of Geophysical Research*, 116(D2).

Mariscal, A. (2015). Dynamique du carbone du sol et rétroactions climatiques. M.S., Univeristé Libre de Bruxelles, Brussels, Belgium.

Marthews, T. R., Dadson, S. J., Lehner, B., Abele, S., and Gedney, N. (2015). High-resolution global topographic index values for use in large-scale hydrological modelling. *Hydrology and Earth System Sciences*, 19(1):91–104.

Masson-Delmotte, V., Zhai, P., Pörtner, H. O., Roberts, D., Skea, J., Shukla, P. R., Pirani, A., Moufouma-Okia, W., Péan, C., Pidcock, R., Connors, S., Matthews, J. B. R., Chen, Y., Zhou, X., Gomis, M. I., Lonnoy, E., Maycock, T., Tignor, M., and Waterfield, T. (2018). IPCC 2018: Summary for policymakers. In *Global warming of 1.5°C. An IPCC Special Report on the impacts of global warming of 1.5°C above pre-industrial levels and related global greenhouse gas emission pathways, in the context of strengthening the global response to the threat of climate change, sustainable development, and efforts to eradicate poverty*. World Meterological Organization.

Matross, D. M., Andrews, A., Pathmathevan, M., Gerbig, C., Lin, J. C., Wofsy, S. C., Daube, B. C., Gottlieb, E. W., Chow, V. Y., Lee, J. T., Zhao, C., Bakwin, P. S., William Munger, J., and Hollinger, D. Y. (2006). Estimating regional carbon exchange in New England and Quebec by combining atmospheric, ground-based and satellite data. *Tellus B: Chemical and Physical Meteorology*, 58(5):344–358.

McGuire, A. D., Christensen, T. R., Hayes, D., Heroult, A., Euskirchen, E., Kimball, J. S., Koven, C., Lafleur, P., Miller, P. A., Oechel, W., Peylin, P., Williams, M., and Yi, Y. (2012). An assessment of the carbon balance of Arctic tundra: comparisons among observations, process models, and atmospheric inversions. *Biogeosciences*, 9(8):3185–3204.

Meesters, A. G. C. A., Tolk, L. F., Peters, W., Hutjes, R. W. A., Vellinga, O. S., Elbers, J. A., Vermeulen, A. T., van der Laan, S., Neubert, R. E. M., Meijer, H. A. J., and Dolman, A. J. (2012). Inverse carbon dioxide flux estimates for the Netherlands. *Journal of Geophysical Research: Atmospheres*, 117(D20).

Metropolis, N., Rosenbluth, A. W., Rosenbluth, M. N., Teller, A. H., and Teller, E. (1953). Equation of State Calculations by Fast Computing Machines. *The Journal of Chemical Physics*, 21(6):1087–1092.

Michalak, A. M. (2004). A geostatistical approach to surface flux estimation of atmospheric trace gases. *Journal of Geophysical Research*, 109(D14).

Miller, J. B., Lehman, S. J., Montzka, S. A., Sweeney, C., Miller, B. R., Karion, A., Wolak, C., Dlugokencky, E. J., Southon, J., Turnbull, J. C., and Tans, P. P. (2012). Linking emissions of fossil fuel CO_2 and other anthropogenic trace gases using atmospheric $^{14}CO_2$. *Journal of Geophysical Research: Atmospheres*, 117(D8).

Miller, S. M., Michalak, A. M., and Levi, P. J. (2014). Atmospheric inverse modeling with known physical bounds: an example from trace gas emissions. *Geoscientific Model Development*, 7(1):303–315.

Nassar, R., Jones, D. B. A., Kulawik, S. S., Worden, J. R., Bowman, K. W., Andres, R. J., Suntharalingam, P., Chen, J. M., Brenninkmeijer, C. a. M., Schuck, T. J., Conway, T. J., and Worthy, D. E. (2011). Inverse modeling of CO_2 sources and sinks using satellite observations of CO_2 from TES and surface flask measurements. *Atmospheric Chemistry and Physics*, 11(12):6029–6047.

Oda, T. and Maksyutov, S. (2011). A very high-resolution (1 km×1 km) global fossil fuel CO_2 emission inventory derived using a point source database and satellite observations of nighttime lights. *Atmospheric Chemistry and Physics*, 11(2):543–556.

Palmer, P. I., O'Doherty, S., Allen, G., Bower, K., Bösch, H., Chipperfield, M. P., Connors, S., Dhomse, S., Feng, L., Finch, D. P., Gallagher, M. W., Gloor, E., Gonzi, S., Harris, N. R. P., Helfter, C., Humpage, N., Kerridge, B., Knappett, D., Jones, R. L., Le Breton, M., Lunt, M. F., Manning, A. J., Matthiesen, S., Muller, J. B. A., Mullinger, N., Nemiitz, E., O'Shea, S., Parker, R. J., Percival, C. J., Pitt, J., Riddick, S. N., Rigby, M., Sembhi, H., Siddans, R., Skelton, R. L., Smith, P., Sonderfeld, H., Stanley, K., Stavert, A. R., Wenger, A., White, E., Wilson, C., and Young, D. (2018). A measurement-based verification framework for UK greenhouse gas emissions: an overview of the Greenhouse gAs Uk and Global Emissions (GAUGE) project. *Atmospheric Chemistry and Physics Discussions*, pages 1–52.

Peters, W., Krol, M. C., van der Werf, G. R., Houweling, S., Jones, C. D., Hughes, J., Schaefer, K., Masarie, K. A., Jacobson, A. R., Miller, J. B., Cho, C. H., Ramonet, M., Schmidt, M., Ciattaglia, L., Apadula, F., Heltai, D., Meinhardt, F., Di Sarra, A. G., Piacentino, S., Sferlazzo, D., Aalto, T., Hatakka, J., Ström, J., Haszpra, L., Meijer, H. A. J., Van Der Laan, S., Neubert, R. E. M., Jordan, A., Rodó, X., Morguí, J.-A., Vermeulen, A. T., Popa, E., Rozanski, K., Zimnoch, M., Manning, A. C., Leuenberger, M., Uglietti, C., Dolman, A. J., Ciais, P., Heimann, M., and Tans, P. P. (2010). Seven years of recent European net terrestrial carbon dioxide exchange constrained by atmospheric observations. *Global Change Biology*, 16(4):1317–1337.

Peters, W., Miller, J. B., Whitaker, J., Denning, A. S., Hirsch, A., Krol, M. C., Zupanski, D., Bruhwiler, L., and Tans, P. P. (2005). An ensemble data assimilation system to estimate CO_2 surface fluxes from atmospheric trace gas observations. *Journal of Geophysical Research: Atmospheres*, 110(D24).

Petit, J. R., Jouzel, J., Raynaud, D., Barkov, N. I., Barnola, J.-M., Basile, I., Bender, M., Chappellaz, J., Davis, M., Delaygue, G., Delmotte, M., Kotlyakov, V. M., Legrand, M., Lipenkov, V. Y., Lorius, C., PÉpin, L., Ritz, C., Saltzman, E., and Stievenard, M. (1999). Climate and atmospheric history of the past 420,000 years from the Vostok ice core, Antarctica. *Nature*, 399(6735):429–436.

Peylin, P., Bacour, C., MacBean, N., Leonard, S., Rayner, P., Kuppel, S., Koffi, E., Kane, A., Maignan, F., Chevallier, F., Ciais, P., and Prunet, P. (2016). A new stepwise carbon cycle data assimilation system using multiple data streams to constrain the simulated land surface carbon cycle. *Geoscientific Model Development*, 9(9):3321–3346.

Peylin, P., Houweling, S., Krol, M. C., Karstens, U., Rödenbeck, C., Geels, C., Vermeulen, A., Badawy, B., Aulagnier, C., Pregger, T., Delage, F., Pieterse, G., Ciais, P., and Heimann, M. (2011). Importance of fossil fuel emission uncertainties over Europe for CO_2 modeling: model intercomparison. *Atmospheric Chemistry and Physics*, 11(13):6607–6622.

Peylin, P., Law, R. M., Gurney, K. R., Chevallier, F., Jacobson, A. R., Maki, T., Niwa, Y., Patra, P. K., Peters, W., Rayner, P. J., Rödenbeck, C., van der Laan-Luijkx, I. T., and Zhang, X. (2013). Global atmospheric carbon budget: results from an ensemble of atmospheric CO_2 inversions. *Biogeosciences*, 10(10):6699–6720.

Pickers, P. (2016). *New applications of continuous atmospheric O_2 measurements: meridional transects across the Atlantic Ocean, and improved quantification of fossil fuel-derived CO_2*. PhD thesis, University of East Anglia.

Potter, C. S. (1999). Terrestrial biomass and the effects of deforestation on the global carbon cycle: Results from a model of primary production using satellite observations. *BioScience*, 49(10):769–778.

Reuter, M., Buchwitz, M., Hilker, M., Heymann, J., Bovensmann, H., Burrows, J. P., Houweling, S., Liu, Y. Y., Nassar, R., Chevallier, F., Ciais, P., Marshall, J., and Reichstein, M. (2016). How Much CO_2 Is Taken Up by the European Terrestrial Biosphere? *Bulletin of the American Meteorological Society*, 98(4):665–671.

Reuter, M., Buchwitz, M., Hilker, M., Heymann, J., Schneising, O., Pillai, D., Bovensmann, H., Burrows, J. P., Bösch, H., Parker, R., Butz, A., Hasekamp, O., O'Dell, C. W., Yoshida, Y., Gerbig, C., Nehrkorn, T., Deutscher, N. M., Warneke, T., Notholt, J., Hase, F., Kivi, R., Sussmann, R., Machida, T., Matsueda, H., and Sawa, Y. (2014). Satellite-inferred European carbon sink larger than expected. *Atmospheric Chemistry and Physics*, 14(24):13739–13753.

Rienecker, M. M., Suarez, M. J., Gelaro, R., Todling, R., Bacmeister, J., Liu, E., Bosilovich, M. G., Schubert, S. D., Takacs, L., Kim, G.-K., Bloom, S., Chen, J., Collins, D., Conaty, A., da Silva, A., Gu, W., Joiner, J., Koster, R. D., Lucchesi, R., Molod, A., Owens, T., Pawson, S., Pegion, P., Redder, C. R., Reichle, R., Robertson, F. R., Ruddick, A. G., Sienkiewicz, M., and Woollen, J. (2011). MERRA: NASA's Modern-Era Retrospective Analysis for Research and Applications. *Journal of Climate*, 24(14):3624–3648.

Rigby, M., Manning, A. J., and Prinn, R. G. (2011). Inversion of long-lived trace gas emissions using combined Eulerian and Lagrangian chemical transport models. *Atmospheric Chemistry and Physics*, 11(18):9887–9898.

Rivier, L., Peylin, P., Ciais, P., Gloor, M., Rödenbeck, C., Geels, C., Karstens, U., Bousquet, P., Brandt, J., and Heimann, M. (2010). European CO_2 fluxes from atmospheric inversions using regional and global transport models. *Climatic Change*, 103(1-2):93–115.

Rockström, J., Gaffney, O., Rogelj, J., Meinshausen, M., Nakicenovic, N., and Schellnhuber, H. J. (2017). A roadmap for rapid decarbonization. *Science*, 355(6331):1269–1271.

Rodenbeck, C., Gerbig, C., Trusilova, K., and Heimann, M. (2009). A two-step scheme for high-resolution regional atmospheric trace gas inversions based on independent models. *Atmos. Chem. Phys.*, page 12.

Rödenbeck, C., Houweling, S., Gloor, M., and Heimann, M. (2003). Time-dependent atmospheric CO_2 inversions based on interannually varying tracer transport. *Tellus B*, 55(2):488–497.

Say, D., Manning, A. J., O'Doherty, S., Rigby, M., Young, D., and Grant, A. (2016). Re-Evaluation of the UK's HFC-134a Emissions Inventory Based on Atmospheric Observations. *Environmental Science & Technology*, 50(20):11129–11136.

Schellekens, J., Dutra, E., Martínez-de la Torre, A., Balsamo, G., van Dijk, A., Sperna Weiland, F., Minvielle, M., Calvet, J.-C., Decharme, B., Eisner, S., Fink, G., Flörke, M., Peßenteiner, S., van Beek, R., Polcher, J., Beck, H., Orth, R., Calton, B., Burke, S., Dorigo, W., and Weedon, G. P. (2017). A global water resources ensemble of hydrological models: the eartH2observe Tier-1 dataset. *Earth System Science Data*, 9(2):389–413.

Schimel, D., Stephens, B. B., and Fisher, J. B. (2015). Effect of increasing CO_2 on the terrestrial carbon cycle. *Proceedings of the National Academy of Sciences*, 112(2):436–441.

Schuh, A. E., Denning, A. S., Corbin, K. D., Baker, I. T., Uliasz, M., Parazoo, N., Andrews, A. E., and Worthy, D. E. J. (2010). A regional high-resolution carbon flux inversion of North America for 2004. *Biogeosciences*, 7(5):1625–1644.

Schuh, A. E., Denning, A. S., Uliasz, M., and Corbin, K. D. (2009). Seeing the forest through the trees: Recovering large-scale carbon flux biases in the midst of small-scale variability. *Journal of Geophysical Research*, 114(G3).

Schulze, E. D., Luyssaert, S., Ciais, P., Freibauer, A., Janssens, I. A., Soussana, J. F., Smith, P., Grace, J., Levin, I., Thiruchittampalam, B., Heimann, M., Dolman, A. J., Valentini, R., Bousquet, P., Peylin, P., Peters, W., Rödenbeck, C., Etiope, G., Vuichard, N., Wattenbach, M., Nabuurs, G. J., Poussi, Z., Nieschulze, J., Gash, J. H., and Team, t. C. (2009). Importance of methane and nitrous oxide for Europe's terrestrial greenhouse-gas balance. *Nature Geoscience*, 2(12):842–850.

Sitch, S., Huntingford, C., Gedney, N., Levy, P. E., Lomas, M., Piao, S. L., Betts, R., Ciais, P., Cox, P., Friedlingstein, P., Jones, C. D., Prentice, I. C., and Woodward, F. I. (2008). Evaluation of the terrestrial carbon cycle, future plant geography and climate-carbon cycle feedbacks using five Dynamic Global Vegetation Models (DGVMs). *Global Change Biology*, 14(9):2015–2039.

Smallman, T. L., Exbrayat, J.-F., Mencuccini, M., Bloom, A. A., and Williams, M. (2017). Assimilation of repeated woody biomass observations constrains decadal ecosystem carbon cycle uncertainty in aggrading forests. *Journal of Geophysical Research: Biogeosciences*, 122(3):528–545.

Smallman, T. L., Williams, M., and Moncrieff, J. B. (2014). Can seasonal and interannual variation in landscape CO_2 fluxes be detected by atmospheric observations of CO_2 concentrations made at a tall tower? *Biogeosciences*, 11(3):735–747.

Stanley, K. M., Grant, A., O'Doherty, S., Young, D., Manning, A. J., Stavert, A. R., Spain, T. G., Salameh, P. K., Harth, C. M., Simmonds, P. G., Sturges, W. T., Oram, D. E., and Derwent, R. G. (2018). Greenhouse gas measurements from a UK network of tall towers: technical description and first results. *Atmospheric Measurement Techniques*, 11(3):1437–1458.

Stavert, A. R., O'Doherty, S., Stanley, K., Young, D., Manning, A. J., Lunt, M. F., Rennick, C., and Arnold, T. (2018). UK greenhouse gas measurements at two new tall towers for aiding emissions verification. *Atmospheric Measurement Techniques Discussions*, pages 1–55.

Steinbach, J., Gerbig, C., Rödenbeck, C., Karstens, U., Minejima, C., and Mukai, H. (2011). The CO_2 release and Oxygen uptake from Fossil Fuel Emission Estimate (COFFEE) dataset: effects from varying oxidative ratios. *Atmospheric Chemistry and Physics*, 11(14):6855–6870.

Steinkamp, K., Mikaloff Fletcher, S. E., Brailsford, G., Smale, D., Moore, S., Keller, E. D., Baisden, W. T., Mukai, H., and Stephens, B. B. (2017). Atmospheric CO_2 observations and models suggest strong carbon uptake by forests in New Zealand. *Atmospheric Chemistry and Physics*, 17(1):47–76.

Stuiver, M. and Quay, P. D. (1981). Atmospheric ^{14}C changes resulting from fossil fuel CO_2 release and cosmic ray flux variability. *Earth and Planetary Science Letters*, 53(3):349–362.

Suntharalingam, P., Kettle, A. J., Montzka, S. M., and Jacob, D. J. (2008). Global 3-D model analysis of the seasonal cycle of atmospheric carbonyl sulfide: Implications for terrestrial vegetation uptake. *Geophysical Research Letters*, 35(19).

Taguchi, S., Law, R. M., Rödenbeck, C., Patra, P. K., Maksyutov, S., Zahorowski, W., Sartorius, H., and Levin, I. (2011). TransCom continuous experiment: comparison of ^{222}Rn transport at hourly time scales at three stations in Germany. *Atmospheric Chemistry and Physics*, 11(19):10071–10084.

Takahashi, T., Sutherland, S. C., Wanninkhof, R., Sweeney, C., Feely, R. A., Chipman, D. W., Hales, B., Friederich, G., Chavez, F., Sabine, C., Watson, A., Bakker, D. C., Schuster, U., Metzl, N., Yoshikawa-Inoue, H., Ishii, M., Midorikawa, T., Nojiri, Y., Körtzinger, A., Steinhoff, T., Hoppema, M., Olafsson, J., Arnarson, T. S., Tilbrook, B., Johannessen, T., Olsen, A., Bellerby, R., Wong, C., Delille, B., Bates, N., and de Baar, H. J. (2009). Climatological mean and decadal change in surface ocean pCO_2, and net sea–air CO_2 flux over the global oceans. *Deep Sea Research Part II: Topical Studies in Oceanography*, 56(8-10):554–577.

Tans, P. P., Conway, T. J., and Nakazawa, T. (1989). Latitudinal distribution of the sources and sinks of atmospheric carbon dioxide derived from surface observations and an atmospheric transport model. *Journal of Geophysical Research: Atmospheres*, 94(D4):5151–5172.

Tarantola, A. (2005). *Inverse Problem Theory and Methods for Model Parameter Estimation*. Other Titles in Applied Mathematics. Society for Industrial and Applied Mathematics.

The UK government (2008). Climate Change Act 2008. Technical report, The Stationary Office Limited, London, UK.

Thompson, R. L. and Stohl, A. (2014). FLEXINVERT: an atmospheric Bayesian inversion framework for determining surface fluxes of trace species using an optimized grid. *Geoscientific Model Development*, 7(5):2223–2242.

Thoning, K. W., Tans, P. P., and Komhyr, W. D. (1989). Atmospheric carbon dioxide at Mauna Loa Observatory: 2. Analysis of the NOAA GMCC data, 1974–1985. *Journal of Geophysical Research: Atmospheres*, 94(D6):8549–8565.

Thurner, M., Beer, C., Santoro, M., Carvalhais, N., Wutzler, T., Schepaschenko, D., Shvidenko, A., Kompter, E., Ahrens, B., Levick, S. R., and Schmullius, C. (2014). Carbon stock and density of northern boreal and temperate forests: Carbon stock and density of boreal and temperate forests. *Global Ecology and Biogeography*, 23(3):297–310.

Todd-Brown, K. E. O., Randerson, J. T., Post, W. M., Hoffman, F. M., Tarnocai, C., Schuur, E. A. G., and Allison, S. D. (2013). Causes of variation in soil carbon simulations from CMIP5 Earth system models and comparison with observations. *Biogeosciences*, 10(3):1717–1736.

Tolk, L. F., Dolman, A. J., Meesters, A. G. C. A., and Peters, W. (2011). A comparison of different inverse carbon flux estimation approaches for application on a regional domain. *Atmospheric Chemistry and Physics*, 11(20):10349–10365.

Turnbull, J. C., Karion, A., Fischer, M. L., Faloona, I., Guilderson, T., Lehman, S. J., Miller, B. R., Miller, J. B., Montzka, S., Sherwood, T., Saripalli, S., Sweeney, C., and Tans, P. P. (2011a). Assessment of fossil fuel carbon dioxide and other anthropogenic trace gas emissions from airborne measurements over Sacramento, California in spring 2009. *Atmospheric Chemistry and Physics*, 11(2):705–721.

Turnbull, J. C., Tans, P. P., Lehman, S. J., Baker, D., Conway, T. J., Chung, Y. S., Gregg, J., Miller, J. B., Southon, J. R., and Zhou, L.-X. (2011b). Atmospheric observations of carbon monoxide and fossil fuel CO_2 emissions from East Asia. *Journal of Geophysical Research: Atmospheres*, 116(D24).

UNECE/EMEP (2001). *EMEP/CORINAIR Emission Inventory Guidebook - 3rd edition 2001*. European Environment Agency.

Vardag, S. N., Hammer, S., O'Doherty, S., Spain, T. G., Wastine, B., Jordan, A., and Levin, I. (2014). Comparisons of continuous atmospheric CH_4, CO_2 and N_2O measurements - results from a travelling instrument campaign at Mace Head. *Atmospheric Chemistry and Physics*, 14(16):8403–8418.

Wang, Y., Deutscher, N. M., Palm, M., Warneke, T., Notholt, J., Baker, I., Berry, J., Suntharalingam, P., Jones, N., Mahieu, E., Lejeune, B., Hannigan, J., Conway, S., Mendonca, J., Strong, K., Campbell, J. E., Wolf, A., and Kremser, S. (2016). Towards understanding the variability in biospheric CO_2 fluxes: using FTIR spectrometry and a chemical transport model to investigate the sources and sinks of carbonyl sulfide and its link to CO_2. *Atmospheric Chemistry and Physics*, 16(4):2123–2138.

Weedon, G. P., Balsamo, G., Bellouin, N., Gomes, S., Best, M. J., and Viterbo, P. (2014). The WFDEI meteorological forcing data set: WATCH Forcing Data methodology applied to ERA-Interim reanalysis data. *Water Resources Research*, 50(9):7505–7514.

White, E. D., Rigby, M., Lunt, M. F., Smallman, T. L., Comyn-Platt, E., Manning, A. J., Ganesan, A. L., O'Doherty, S., Stavert, A. R., Stanley, K., Williams, M., Levy, P., Ramonet, M., Forster, G. L., Manning, A. C., and Palmer, P. I. (2019). Quantifying the UK's carbon dioxide flux: an atmospheric inverse modelling approach using a regional measurement network. *Atmospheric Chemistry and Physics*, 19(7):4345–4365.

Williams, M., Rastetter, E. B., Fernandes, D. N., Goulden, M. L., Shaver, G. R., and Johnson, L. C. (1997). Predicting Gross Primary Productivity in Terrestrial Ecosystems. *Ecological Applications*, 7(3):882–894.

Xueref-Remy, I., Dieudonné, E., Vuillemin, C., Lopez, M., Lac, C., Schmidt, M., Delmotte, M., Chevallier, F., Ravetta, F., Perrussel, O., Ciais, P., Bréon, F.-M., Broquet, G., Ramonet, M., Spain, T. G., and Ampe, C. (2018). Diurnal, synoptic and seasonal variability of atmospheric CO_2 in the Paris megacity area. *Atmospheric Chemistry and Physics*, 18(5):3335–3362.

Zeebe, R. E., Ridgwell, A., and Zachos, J. C. (2016). Anthropogenic carbon release rate unprecedented during the past 66 million years. *Nature Geoscience*, 9(4):325–329.

Zupanski, D., Denning, A. S., Uliasz, M., Zupanski, M., Schuh, A. E., Rayner, P. J., Peters, W., and Corbin, K. D. (2007). Carbon flux bias estimation employing Maximum Likelihood Ensemble Filter (MLEF). *Journal of Geophysical Research*, 112(D17).